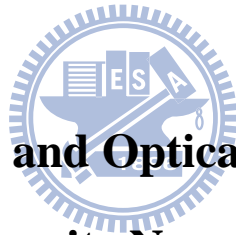# 國立交通大學

材料科學與工程學系

博 士 論 文

黃銅礦奈米晶體的合成與光學特性研究

Study on Synthesis and Optical Characteristics of Chalcopyrite Nanocrystals

研 究 生：郭冠廷

指導教授：陳三元 博士

中 華 民 國 九 十 八 年 八 月

黃銅礦奈米晶體的合成與光學特性研究

Study on Synthesis and Characteristics of

Chalcopyrite Nanocrystals

研 究 生：郭冠廷　　　　　　Student：Kuan-Ting Kuo

指導教授：陳三元博士　　　　Advisor : Dr. San-Yuan Chen

國 立 交 通 大 學

材 料 科 學 與 工 程 學 系

博 士 論 文

A Thesis

Submitted to Department of Materials Science and Engineering

College of Engineering

National Chiao Tung University

in partial Fulfillment of the Requirements

for the Degree of Doctor in

Materials Science and Engineering

August 2009

Hsinchu, Taiwan, Republic of China

中 華 民 國 九 十 八 年 八 月

黃銅礦奈米晶體的合成與光學特性研究

研究生:郭冠廷 　　　　　　　　　指導教授:陳三元

國立交通大學材料科學與工程學系

中文摘要

銅銦二硫半導體近來被認為是最佳的太陽能材料,因為其具有適合的能帶寬(1.5 eV) 和高吸收係數,與理想的太陽能光譜幾乎完全匹配,若作為太陽能電池的吸收層可將入射光子完全吸收。過去十年,銅銦二硫薄膜被廣泛研究,其太陽能最佳轉換效率達到 12.7%。此外,銅銦二硫奈米晶體仍被認為具有相當大的潛力可提高太陽能轉換效率,這是因為奈米晶體產生的量子侷限效應具有多重激子(multiple excitons)與內部能帶(intra band-gap)的優點。因此本論文將探討銅銦琉與類銅銦二硫奈米晶體的合成,結構鑑定與在太陽能電池元件的相關應用。

本論文首先利用膠體方法合成銅銦琉的奈米晶體與不同厚度包覆的核-殼結構的銅銦二硫-硫化鋅奈米晶體,並以 X 光繞射儀(XRD)、穿透式電子顯微鏡(TEM)、X 光光電子能譜儀（XPS）、動態雷射散射分析儀(DLS)鑑定合成奈米晶體的結構與粒徑大小。本論文合成的均勻銅銦二硫奈米晶體的粒子半徑為 2.4 奈米,核-殼結構耐米晶體粒子半徑大小則為 4.6 奈米。由於量子侷限效應,所得銅銦二硫奈米晶體的放射光波長在 450 奈米,明顯高於塊材的銅銦二硫半導體能帶。硫化鋅表面改質消除了銅銦二硫奈米晶體表面的缺陷,因此可明顯提高其發光強度。

合成銅銦二硫奈米晶體後,我們將三種不同比例的鋅導入銅銦二硫奈米晶體中,分別為n=1,n=2和n=3(n=Cu/Zn)。並將這些奈米晶體嫁接到5μm長的氧化鋅奈米線上,探討其太陽能轉換效率。合成後的鋅參雜銅銦二硫奈米晶體的吸收波長分別為530(n=1),570(n=2)和650(n=3)奈米。當n=2的時候,可得到最佳的轉換效率,其值為0.28%,短路電流(Jsc)為1.71mA/cm^2,開路電壓(Voc)為0.34V,

而填充係數(FF)則為0.48。此類型量子點太陽能電池的限制來自於激子快速的再結合與電解液，當沉積硫化鋅保護層於鋅參雜銅銦二硫奈米晶體表面後，主要太陽能電池參數都獲得提升($Jsc = 3.21$ ma/cm^2, $Voc = 0.45$ V, $FF = 0.49$)，因此得到轉換效率為0.71%。

本論文提出的第二個方法是在高頻磁場(High frequency magnetic field)下合成高品質的鋅參雜的銅銦二硫奈米晶體，所有實驗過程在正常大氣環境與室溫下即可進行。磁性的參雜提供了主體(host)在外加磁場下產生超順磁性加熱，使得晶體以高於傳統高溫爐加熱速度的2-3個級數快速成長。隨磁場時間的作用，鋅參雜的銅銦二硫奈米晶體形貌隨之變化，從球體，錐體，立方體，最後形成長方體。

本論文最後將磁場下合成的，含有不同形狀銅銦二硫奈米晶體的膠體溶液製成”奈米墨水”並應用於太陽能電池元件中，將其塗佈成銅銦二硫薄膜吸收層，最佳轉換效率為1.01%，吸收層膜厚為1.012μm(長方體樣品)。吸收層膜厚提高到2.132μm後效率可達到1.44%。

Study on Synthesis and Optical Characteristics of Chalcopyrite Nanocrystals

Student : Kuan-Ting Kuo   **Advisor : San-Yuan Chen**

**Department of Materials Science and Engineering National
Chiao Tung University**

Abstract

Copper indium disulfide ($CuInS_2$) semiconductor has been considered as the best materials for solar-cells because it has a superior band-gap of 1.5 eV and high absorption coefficient, which matches almost ideally to the solar spectrum and assures a complete absorption of the incident photon flux in an absorber layer. In the past decade, $CuInS_2$ film has been widely studied and the best conversion efficiency for solar cells is about 12.7 %. On the other hand, $CuInS_2$ nanocrystals still have great potential to promote power conversion efficiency due to quantum confinement effect, such as multiple excitons and intra band-gap. Therefore, in this thesis, the synthesis, characterization and application of $CuInS_2$ and derivative nanocrystals, will be systematically studied.

The bare $CuInS_2$ with different shell thickness, $CuInS_2$@ZnS core-shell nanocrystals, are first produced via a colloidal method and characterized by X-ray diffraction (XRD), transmission electron microscopy (TEM), X-ray photoelectron spectroscopy (XPS), and dynamic light scattering (DLS). The obtained nanocrystals are quasimonodisperse with an average particle size of 2.4 (bare) and 4.6 (core-shell) nm, respectively. The emission peak of obtained $CuInS_2$ is around 450 nm, which is higher than bulk $CuInS_2$ due to the size-dependent quantum confinement effect. ZnS modification eliminates defects on the surface of $CuInS_2$ and significantly enhances photoluminescence consequently.

After the $CuInS_2$ nanocrystals were developed, the Zn was introduced into

CuInS$_2$ nanocrystals with three different Cu/Zn ratios (n value) which were and then deposited onto 5 μm long ZnO nanowire substrate as a quantum dot (QD)-based solar cell. The absorbance peak of obtained Zn doped CuInS$_2$ nanocrystals shift from 530, 570, to 650 nm correspond to n = 1, 2, and 3, respectively. The best conversion efficiency of bare Zn doped CuInS$_2$ is 0.28 % for n =2 sample, short-circuit current density (*Jsc*) is 1.71 mA/cm^2, open-circuit voltage (*Voc*) is 0.34 V, and fill factor (*FF*) is 0.48. It was fond that the restriction of such quantum dot-based solar cells could be due to the fast recombination time and corrosion from electrolyte. But, after depositing ZnS layer on the surface of Zn-CuInS$_2$ nanocrystals, an optimal efficiency at 0.71 % could be obtained, resulting from the promotion of all solar cell parameters. (*Jsc* = 3.21 ma/cm^2, *Voc* = 0.45 V, FF = 0.49)

The second novel method we present is using magnetic Zn doping to synthesize high quality CuInS$_2$ nanocrystals under high frequency magnetic field at ambient conditions. The magnetic doping gives superparamagnetic heating of the resulting nanocrystals via magnetic induction, causing an accelerating growth rate of the doped CuInS$_2$ under ambient conditions of 2-3 orders of magnitude faster than conventional autoclave synthesis. Shape evolution of the Zn doped CuInS$_2$ nanocrystals from initially spherical, to pyramidal, cubic, and finally to a bar geometry, were detected as a function of time of exposure to magnetic induction.

Finally, these colloidal solvent with different shape nanocrystals were further used as "nanoink" to fabricate a simple thin film solar device, the best efficiency of these crystals we obtained is 1.01 % with a 1.012 um thick absorber layer (bar geometry). The efficiency can be promoted to 1.44 % after thickening absorber to 2.132 um.

Keywords: chalcopyrite, CuInS$_2$, nanocrystal, solar cell, core-shell, high frequency magnetic field.

Ackonwledgements

My greatest debt is to my advisor, Prof. Dr. San-Yuan Chen, who provided me the opportunity to study in his group. Under his discipline, I have been enabled to develop my potential and finish this thesis. Much training he gave me to research independently and think deeply have stimulated my indomitable attitude, and enabled me to accumulate more experiences in my independent work.

I am deeply grateful to Dr. Dean-Mo Liu, whose detailed supervision and continuous supports laid a smooth foundation for my studies. From the experimental work, discussions, to the corrections of this dissertation, especially in editing of the English, he has given essential constructive and indispensable input to this dissertation. His intrinsic carefulness and patience led all my papers and this dissertation to much less errors and more readable.

During my first 4 years, I am particularly thankful for the financial support from Chunghwa Picture Tubes (CPT) Inc and Dr. Bing-Ming Cheng who serves at the National Synchrotron Radiation Research Center (NSRRC). Without their support, I might not able to continue my Ph D study.

I am especially indebted to my colleague in this lab, who contributed directly and indirectly to this accomplishment.

Last, I appriciate my family for their understanding and unconditional support, and thank my friends in "39 group" for their accompanying and listening in my difficult time. Finally, special thanks to my girl friend, Wei-Chen, who gave me the most patient and loving supports, as well as encouragement during the course of this work.

Kuan-Ting Kuo, September 2009

Hsinchu, Taiwan

Contents

Figure captions

Table captions

Chapter 1

Introduction

During the past decade, the energy resource concerns have become more and more imperative, great efforts have been focused on the development of renewable energy resources, **[1-2]** among which photovoltaic solar power holds the great potential and brilliant advantages such as unpollutedness, safety and inexhaustibleness. The development of photovoltaic community is well aware of the cost benefits which associated with the continued increase in solar cell efficiency. Over the past decade much of the cell efficiency improvements have resulted from the move towards multi-junction devices. However, as researchers continue to push the envelope, they are looking towards new approaches, such as the use of nanotechnology, in improving device efficiencies.

Semiconductor nanocrystals, and luminescent nanocrystals have attracted considerable interest during the past decade because of their numerous applications in photoelectronic devices and biotechnology. **[3-6]** Recently developed quantum dot-based solar cells are of special interest due to quantum size effects such as slower cooling rate of excitons and multiple exciton generation. **[7-11]** As a result of quantum confinement, the theoretical energy conversion efficiency of quantum dot-based solar cells is predicted to be 66%. **[9]** This concept has been demonstrated on TiO_2 electrodes by depositing CdS **[12-13]** and CdSe. **[14-16]** Recently, it has been reported on using ZnO nanowires following a QD deposition. **[17]**

In comparison to the current workhorse of semiconductor nanocrystal emitters, those made from CdSe, $CuInS_2$ (CIS) nanocrystal emitters are more acceptable for real-world applications because, in contrast to the CdSe-based ones, CIS does not contain any Class A element (Cd, Pb, and Hg) or Class B element (Se and As). CIS is one of the most important I-III-VI_2 semiconductor materials for use in photovoltaic

1

solar cells and it has many notable advantages such as an appropriate band gap, a high absorption coefficient, and good thermal, environmental, and electrical stability. [18-20]

Recently, ZnO nanowires have been employed in dye-sensitized [21] and hybrid solar cells (PVs) [22] to substitute for TiO_2 films and particles. The nanowires can help improve electron transport by avoiding the particle-to-particle hopping that occurs in the TiO_2 network. Furthermore, nanowires provide direct conduction pathways for the electrons from the point of injection to the collection electrode. To develop this new generation of devices, single-crystalline and nearly monodisperse semiconductor nanocrystals with tunable sizes are critical. Conversely, there has been barely any investigation into using CIS nanocrystals for such a new generation of devices, presumably due to the poor quality of CIS nanocrystals.

The synthesis and characterization of semiconductor nanocrystals have attracted much attention due to their potential applications in the fields of magnetics, optics, electronics, and catalysis. [23-25] These nanocrystals have controllable sizes in the nanometer range and exhibit remarkable physical properties that can be finely tuned by adjusting the crystal composition, size, and shape. [26-27] It has been demonstrated that there exist strong correlations between the shape of a nanostructure and its corresponding performance in chemistry and materials science. [28-29] CIS nanocrystals have been synthesized by a number of research groups in the recent past, but the chemistry continues to be refined to obtain nanocrystals with improved size control. Part of the challenge facing these efforts has been the need for better synthetic methods for nanocrystals of the desired CIS compound, which will be thoroughly investigated as illustrated in the thesis.

Chapter 2 starts with a introduction of development of solar cell, followed by a brief introduction of known physical properties such as electrical, electronical, optical

properties of CIS material. Then reports about variety of synthesis of CIS nanocrystals come after introduction.

In **Chapter 3,** the experiment steps and characterization techniques employed in this work were outlined, that is, X-ray diffraction (XRD), transmission electron microscope (TEM), X-ray photoelectron spectroscopy (XPS), ultraviolet-visible (Uv-vis), photoluminescence emission (PL), and scanning electron microscopy (SEM) for surface, structure and morphology characterization, and optical transmission and *I-V* curve measurement for efficiency, respectively.

In **Chapter 4**, we synthesized high-quality CIS@ZnS (core-shell) nanocrystals via a colloidal solvent process and characterized for their optical properties by UV-vis, room temperature solution PL spectroscopy. All of the as-synthesized nanocrystals can be well dispersed in toluene or hexane to form stable and clear colloidal solutions, which shows strong visible emission (blue for CIS@ZnS core/shell nanocrystals, see section 4.3) under UV excitation. The growth of a ZnS shell on CIS nanocrystals, that is, the formation of CIS@ZnS core/shell NCs, resulted in an impact enhancement in the PL intensity compared to that of bare CIS nanocrystals due to the eliminated surface defects and the reduced lattice mismatch between the core and shell materials. A dramatic increase of the PL intensity can be obtained from the ZnS-capped CIS with respect to that of the bare CIS nanocrystals.

To further apply CIS nanocrystals to dye-sensitized solar cell, we developed a novel quantum-dot-based solar cell assembly consisting of core-shell Zn-doped CuInS$_2$@ZnS (Zn-CIS@ZnS) quantum dots associated with short ZnO (5 μm in length) nanowires, as shown in **Chapter 5**. In section 5.2, the photo-conversion efficiency of the Zn-CIS-based solar cells without the presence of the ZnS shell can be readily tuned by controlling the Zn/Cu ratio. Furthermore, the efficiency was significantly improved upon the deposition of a thin ZnS shell on these Zn-CIS QDs,

where a significant enhancement in short-circuit current density was observed because the ZnS coating is able to effectively eliminate the excited electrons recombination and enhance the charge transfer efficiency from Zn-CIS QDs to ZnO nanowires. The power-conversion efficiency is promoted more than 2~3 times as that without ZnS coating.

In *Chapter 6*, we report a novel and facile method to synthesize phase pure, chemically homogeneous, and highly crystalline $CuInS_2$, an important element for optoelectronics, optics, and solar energy applications. This ternary semiconductor compound is grown by magnetic Zn doping under high-frequency magnetic induction at ambient conditions. Nanostructural development of the nanocrystals was well characterized and a mechanism of crystal growth was proposed.

Fabrication of simple device based on colloidal nanocrystals synthesized in *Chapter 6* will be discussed in *Chapter 7*. Efficiencies of different shapes CIS nanocrystals will be measured, followed by a comparison. Finally, conclusion and future researches will be summarized in *Chapter 8*.

Chapter 2

Literature Review and Theory

2.1 Development of Solar Cell

The modern era of photovoltaic device technology reached its Golden Jubilee year in 2003. **[30]** Since the discovery of a p–n junction Si photovoltaic (PV) device **[31]** reported in 1954, the science and technology of PV devices (solar cells) and systems have undergone revolutionary developments. Today, the best single crystal Si solar cells have reached an efficiency of 24.7%, compared with the theoretical maximum value of 30%. However, its growth is limited largely by the ultimate cost of the PV power. Despite tremendous progress in all aspects of production of Si-based solar cells and the rapid decrease of production cost **[32]** from $4.2/Wp in 1992 to $1.7/Wp in 2002, large-scale household applications are not commercially viable as yet.

Based on the material sorts, variety of solar cell can be classified into three generations: (1) The first generation: single crystal Si and poly-crystal Si-based solar cells, (2) Second generation (thin film solar cell): III-V, II-VI and I-III-V group solar cells, and (3) Third generation: nanotechnology such as dye-sensitized solar cells and quantum dots-based solar cells. A brief introduction would be present below.

Crystalline silicon was first used to produce solar cells, and still dominates the PV market today. First generation is manufactured by silicon materials, the operation principle is shown as Figure 2.1, once sun light illuminate on the chip combined with two type semiconductors (p-n junction), electrons migrated to n-type semiconductor (holes migrated to p-type semiconductor) and consequently induced electricity. First generation cells consist of large-area, high quality and single junction devices. First Generation technologies involve high energy and labor inputs which prevent any significant progress in reducing production costs. Single junction

silicon devices are approaching the theoretical limiting efficiency of 31% **[33]** and achieve cost parity with fossil fuel energy generation after a payback period of 5–7 years.
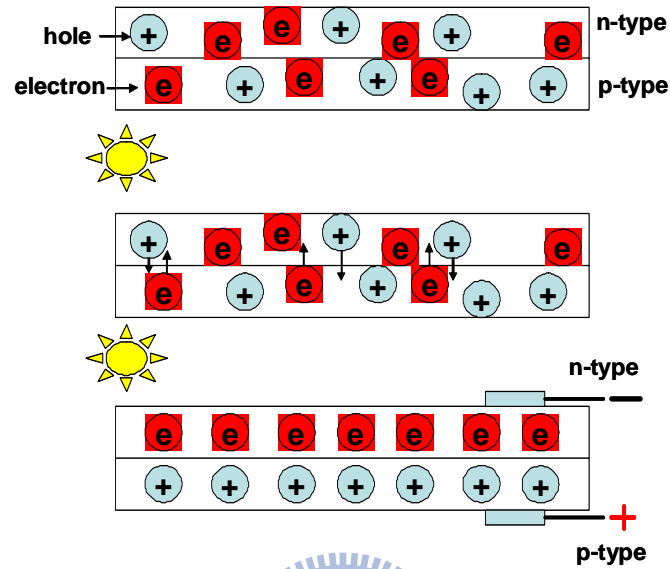
Figure 2.1 Mechanism of first generation solar cell.

Second generation materials have been developed to address energy requirements and production costs of solar cells. The most successful second generation materials have been cadmium telluride (CdTe), copper indium gallium selenide (CIGS), amorphous silicon and micromorphous silicon. These materials are applied in a thin film to a supporting substrate such as glass or ceramics, reducing material mass and therefore costs. The thickness range of such a layer is wide and varies from a few nanometers to tens of micrometers. These technologies do hold promise of higher conversion efficiencies, particularly CIGS-CIS and CdTe offers significantly cheaper production costs. Typical CIGS materials are $CuInSe_2$, $CuInS_2$, $CuInGaSe_2$ and their alloys with bandgaps ranging from 1.05 to 1.7 eV, which is favorable for absorbing the solar radiation. The high absorption coefficient of these materials of almost 10^5 cm^{-1} assures a complete absorption of the incident photon flux in an absorber layer as thin as a few microns. Polycrystalline chalcopyrite-based thin

film solar cells have recently reached conversion efficiencies as high as 18.8%, **[34]** which is the highest value so far achieved for any polycrystalline thin film solar cell. This record device consists basically of a coevaporation-deposited *p*-type Cu(InGa)Se$_2$ absorber layer, an *n*-type thin CdS buffer, and an *n*-type ZnO window layer, as shown in Figure 2.2.

Transparent from contact	ZnO:Al (0.3~0.4 um)
	ZnO(~0.1 um)
	CdS (~0.05um)
	CIGS (1.5~2.5 um)
	Mo(0.3~0.4 um)
Glass substrate	
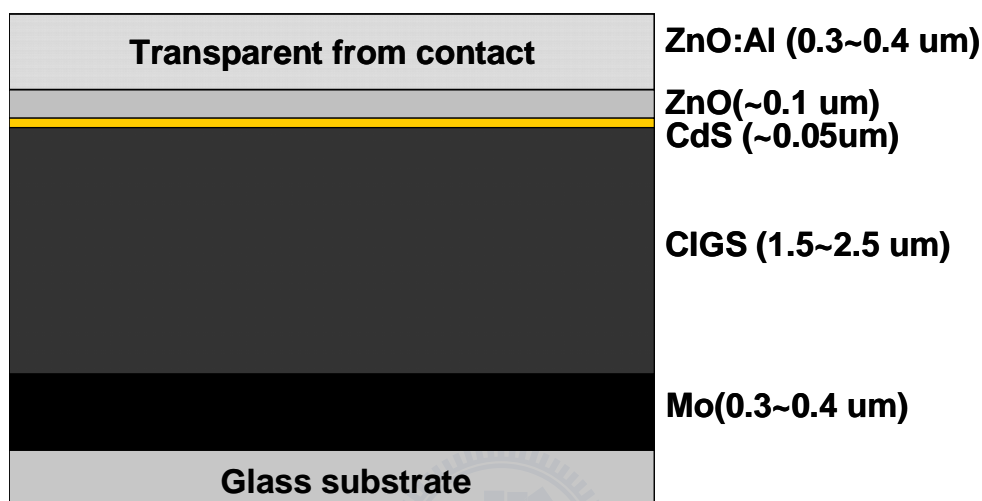
Figure 2.2 Schematic cross section of a typical CuInGaSe$_2$ solar cell.

The dominance of the photovoltaic field by inorganic solid-state junction devices is now being challenged by the emergence of a third generation of cells, based, for example, on nanocrystalline and conducting polymers films. These offer the prospective of very low cost fabrication and present attractive features that facilitate market entry. It is now possible to depart completely from the classical solid-state junction device, by replacing the contacting phase to the semiconductor by an electrolyte, liquid, gel or solid, thereby forming a photo-electrochemical cell. The prototype of these devices is the dye-sensitized solar cell, which realizes the optical absorption and the charge separation processes by the association of a sensitizer as light-absorbing material with a wide band gap semiconductor of nanocrystalline morphology.

Third generation photovoltaic cell, also called advanced thin-film photovoltaic cell, is a range of novel alternatives to "first generation" (silicon p-n junction or wafer solar cells) and "second generation" (low-cost, but low-efficiency thin-film) cells. It is an even more advanced version of the thin-film cell. The dye-sensitized solar cell (DSSC) provides a technically and economically credible alternative concept to present day p–n junction photovoltaic devices [35]. In contrast to the conventional systems where the semiconductor assume both the task of light absorption and charge carrier transport the two functions are separated here. Light is absorbed by a sensitizer, which is anchored to the surface of a wide band semiconductor. Charge separation takes place at the interface via photo-induced electron injection from the dye into the conduction band of the solid. Carriers are transported in the conduction band of the semiconductor to the charge collector. A schematic presentation of the operating principles of the DSSC is given in Figure 2.3. At the heart of the system is a mesoporous oxide layer composed of nanometer-sized particles which have been sintered together to allow for electronic conduction to take place. The material of choice has been TiO_2 (anatase) although alternative wide band gap oxides such as ZnO [36] has also been investigated. Attached to the surface of the nanocrystalline film is a monolayer of the charge transfer dye. Photo-excitation of the sensitizer (S) is followed by electron injection into the conduction band of the mesoporous oxide semiconductor. The dye molecule is regenerated by the redox system, which itself is regenerated at the counter electrode by electrons passed through the load. Potentials are referred to the normal hydrogen electrode (NHE). The open-circuit voltage of the solar cell corresponds to the difference between the redox potential of the mediator and the Fermi level of the nanocrystallline film indicated with a dashed line.

The other important new concept of third generation solar cell is quantum dots-based solar cell (Figure 2.4). Quantum dot (QD) solar cells have the potential
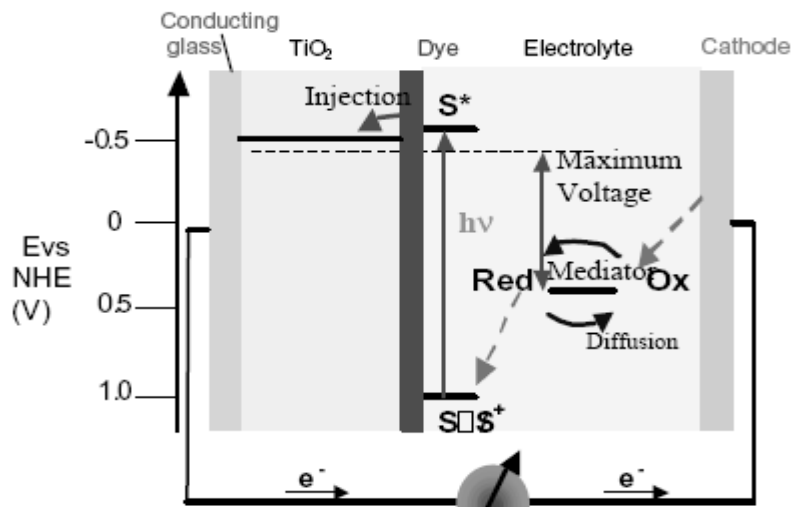
Figure 2.3 Principle of operation and energy level scheme of the dye-sensitized nanocrystalline solar cell. **[35]**

to increase the maximum attainable thermodynamic conversion efficiency of solar photon conversion up to about 66% by utilizing hot photogenerated carriers to produce higher photovoltages or higher photocurrents. The former effect is based on miniband transport and collection of hot carriers in QD array photoelectrodes before they relax to the band edges through phonon emission (Figure 2.5). The latter effect is based on utilizing hot carriers in QD solar cells to generate and collect additional electron–hole pairs through enhanced impact ionization processes (Figure 2.6).
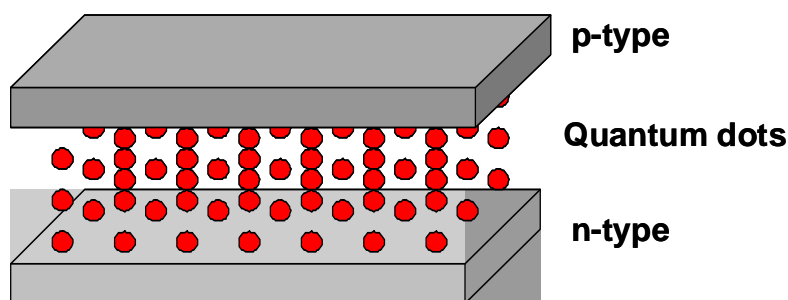
Figure 2.4 Structure of basic quantum dot solar cell.

Current researches have introduced QDs into DSSC system to substitute for dye as the light absorber. **[37, 38]** They used ZnO nanowires and TiO$_2$ nanotubes as the electrodes, combined with CdSe QDs as light absorber (see Figure 2.7 and 2.8). However, both the efficiency was less then 1 %, much lower than predicted value.
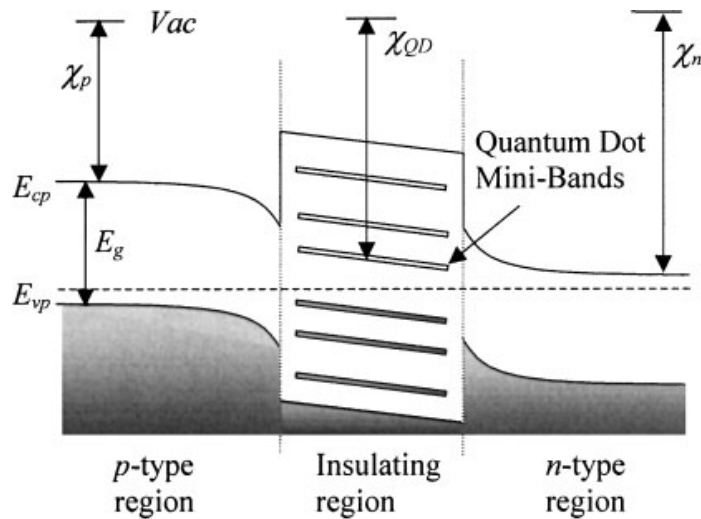
Figure 2.5 Idealized energy band diagram of a quantum dot solar cell. **[8]**
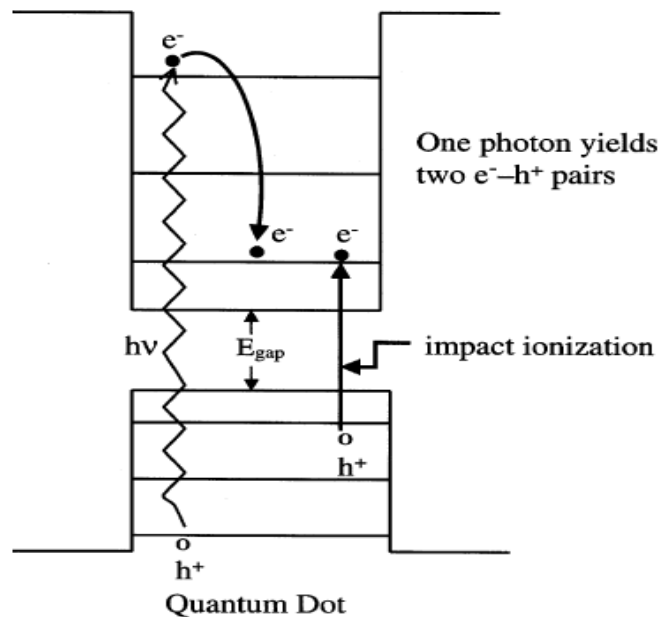
Figure 2.6 Enhance photovoltaic efficiency in quantum dot solar cell by impact ionization. **[9]**

In spite of such low efficiency, QD-based solar cell is still worth to be developed. To overcome the bottleneck for higher efficiency, new QDs are necessary to be found and studied for their potential. CuInS$_2$ is the most important candidate for this purpose.

In the next section, basic properties and synthesis methods of CuInS$_2$ will be introduced.
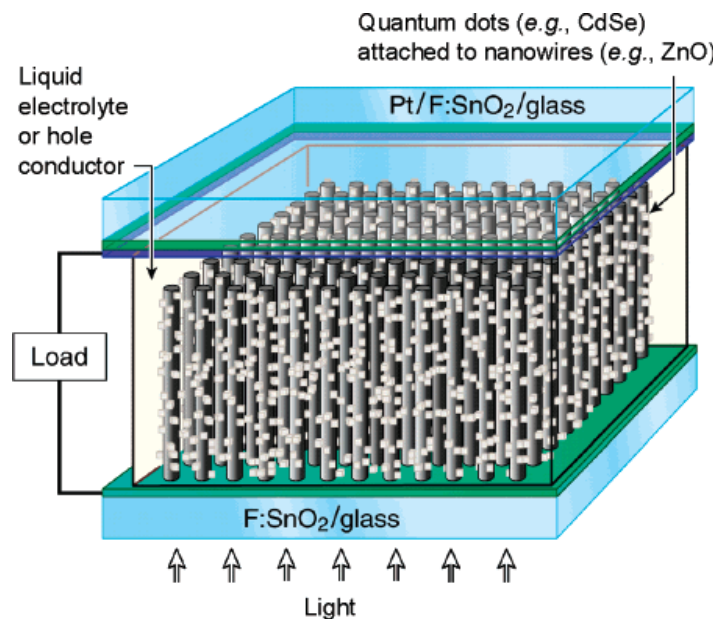
Figure 2.7 Schematic device of CdSe QD/ZnO-based DSSC. **[37]**
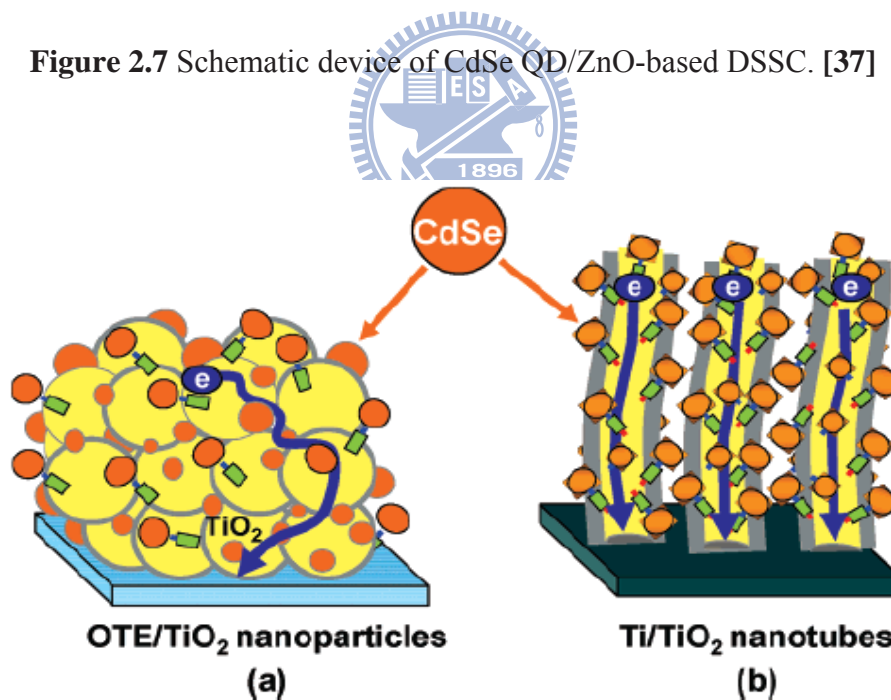
Figure 2.8 Illustration of CdSe QDs/TiO$_2$-based DSSC. **[38]**

2.2 Brief Review of CuInS$_2$

CuInS$_2$ (CIS) is one of the ternary chalcopyrite compound family. A comprehensive review of chalcopyrite compounds was first reported by Shay and Wernick. [39] Recent experimental studies have been worked on thin film due to their great potential for large area PV modules. The structure and physical properties of CIS are further reported as follows.

2.2.1 Crystal Structure of CuInS$_2$

CIS has the chalcopyrite lattice structure. This is a diamond-like structure similar to the sphalerite (zincblende) structure but with an ordered substitution of the group I (Cu) and group III (In) elements on the group II (Zn) sites of sphalerite. This gives a tetragonal unit cell depicted in Figure 2.9 with a ratio of the tetragonal lattice parameters c/a close to 2 (see Table 2.1). The deviation from $c/a = 2$ is called the tetragonal distortion and stems from different strengths of the Cu–S and the In–S bonds. Structural and optical properties of chalcopyrite materials are compared in table 2.1. The reduced symmetry, due to two kinds of cations, leads to a primitive cell of eight atoms in the chalcopyrite structure compared to a primitive cell of two atoms in the sphalerite structure. The Bravais lattice of the chalcopyrite is body centered tetragonal, belonging to space group $I42d$. [40] Compared to the face centered cubic Bravais cell of the sphalerite the unit cell is doubled along the crystal c axis. At room temperature, the ternary compounds stabilize in chalcopyrite structure, however, they may crystallize in sphalerite structure at high temperature (975-1047°C) where the different cations are distributed randomly. [41]
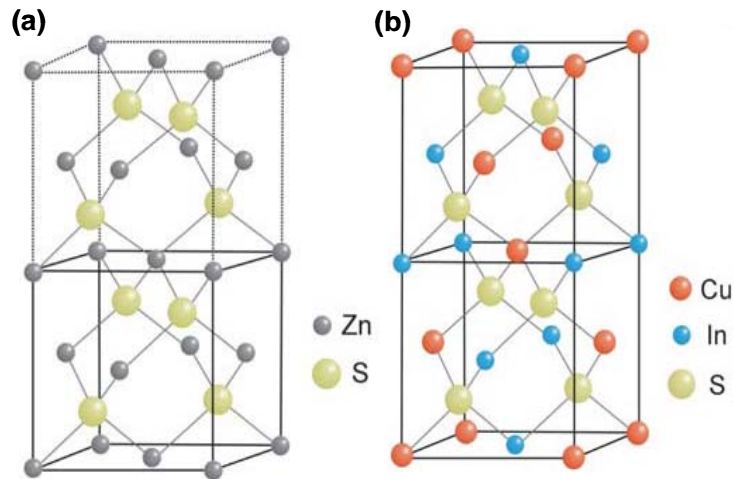
Figure 2.9 Structures of (a) zincblende ZnS and (b) chalcopyrite $CuInS_2$.

Table 2.1 Summary of crystal structure, space group, Bravais lattice, and lattice constants of $CuInS_2$ in the zincblende, chalcopyrite.

material	Crystal structure	Bravais Lattice	Space group	Lattice constants
$CuInS_2$	zincblende	fcc	*F43m (216)*	$a=b=c=0.551$[42]
	chalcopyrite	bc-tetragonal	*I42d (122)*	$a=b=0.5523$[43] $c=1.1133$ $c/a=2.0158$

2.2.2 Physical Properties

Figure 2.10 presents a schematic band structure of CIS, with notation of the contributions of the atomic orbitals. The valence band is separated into two parts, with the upper part reaching 5 eV and the lower one located around 7 eV. The Cu $3d$ and S $3p$ orbitals from the Cu-S bond contribute to the upper valence band whereas the S $3p$ and In $4p$ from the In-S bond form the lower valence band. At around 12 eV a band is built from S $3s$ states and a narrow band is set up near 17 eV by In $4d$ orbitals. The conduction band is formed by S $3p$ and In $5s$ orbitals. [44] This theoretical calculation of the band structure of CIS is in good agreement with the experimental results of X-ray photoemission spectroscopy in respect of the valence band structure. [45, 46] However, it underestimates the optical band gap relative to the experiment.
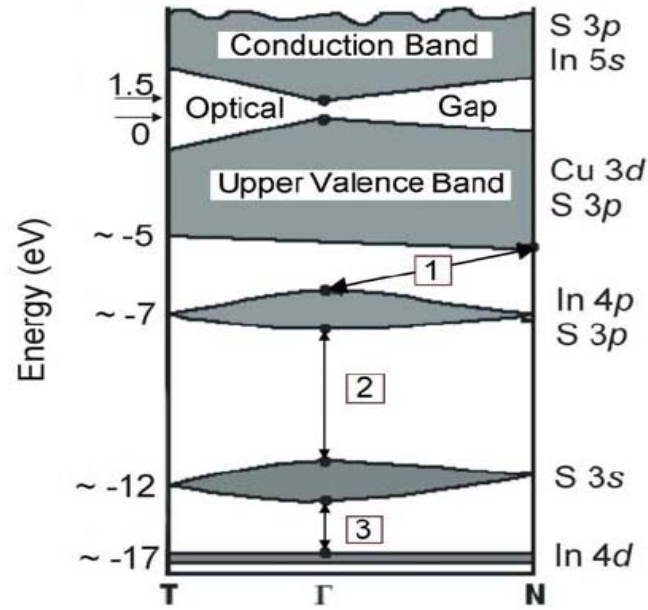
Figure 2.10 Schematic band structure of $CuInS_2$, with indication of contributions of the atomic orbitals and the corresponding energy levels. Shade areas denote the major subbands, and the boxed numbers mark the three internal gaps. **[44]**

CIS is a direct semiconductor. Whereas bandgaps of 1.55 and 1.53 eV were found for bulk single crystals at low (2 K) and room temperature, respectively, band gaps varying between 1.38 and 1.55 eV were reported for CIS thin films at RT depending on different deposition techniques used. **[39, 47-52]** As is normally expected for semiconductors, the bandgap of CIS films decreases with increasing temperature and can be characterized over the temperature range 300-77 K according to the relation

$$E_g = E_{g0} - \beta T^2/(T + \alpha) \qquad (2.1)$$

with the initial bandgap E_{g0}=1.62 eV, two constants α =231.54 K and β = 4.3$\times$ 10^{-4} eV/K, respectively. **[52]** Around the fundamental absorption edge, CIS has an absorption coefficient between 10^4 to 10^5 cm^{-1}, it can thus absorb the incident light with photon energies higher than the bandgap within a few microns.

A number of studies on the electrical properties of CIS bulk single crystals and

thin films have been reported. **[53-58]** Unlike its binary II-VI analogues that are normally n-type, CIS can be made both n- and p-type, depending upon its composition, i.e., deviation from molecularity and stoichiometry, defined as [Cu]/[In]-1 and $2[S]/([Cu]/3[In])-1$, respectively. **[59]** It was generally observed that for $CuInS_2$ single crystals good p-type behavior (ρ ~1-5 Ω cm, μ ~ 15-20 cm^2/Vs) could be obtained by annealing in a sulfur overpressure, and good n-type characteristics (ρ ~1 Ω cm, μ ~ 100- 200 cm^2/Vs), by annealing in indium or Cu + In with a minimum S pressure. **[53, 54]** Similar behavior was observed for CIS films. Excess-sulfur films were generally p-type while sulfur-deficient and indium-rich films were n-type. **[58]** The observed behavior of the conducting type of CIS can be understood based on the predicted defect energies and on the ternary Cu-In-S phase diagram. In table 2.2, the defect levels of donors and acceptors reported for $CuInS_2$ are summarized.

Table 2.2 Summary of the defect levels of donors and acceptors reported for $CuInS_2$.

Defect nature	Defect assignment	Ionization energy (eV)	Refs
Acceptor	V_{Cu}	0.10	**[60-63]**
Acceptor	V_{In}	0.15	**[64-66]**
Donor	V_S(or In_{Cu})	0.035	**[61, 64-67]**
Donor	In_i (or In_{Cu})	0.072	**[64, 65]**
Donor	In_{Cu}	0.145	**[59, 61]**

2.3 Synthesis Methods of Nanocrystal CuInS$_2$

2.3.1 Solvothermal

In recent years, multinary chalcopyrite compounds have attracted much attention due to their interesting physical properties. It is well known that the device properties of CIS-based solar cells are badly affected by their stoichiometric composition, defects, and structure, which are strongly related to the preparation conditions. Some studies have been interested in the use of solvothermal routes, which are carried out at low temperatures and do not require organometallic or toxic precursors, to prepare various kinds of nanocrystalline materials with a wide range of optical and electronic properties accessible in nanoscale.

Jiang *et al.* [68] synthesized CIS nanorod at 280°C through elemental solvothermal reaction. Starting materials were analytical grade Cu, In, and S powders. Ethylenediamine was used as solvent. The XRD pattern of this retragonal phase yielded cell constants a = 5.5086 A, c = 11.0264 A, close to the reported data (JCPDS card, no.38-777). The TEM image (Figure 2.11) indicated that CIS is a nanorod with size of 20 nm x 800 nm.
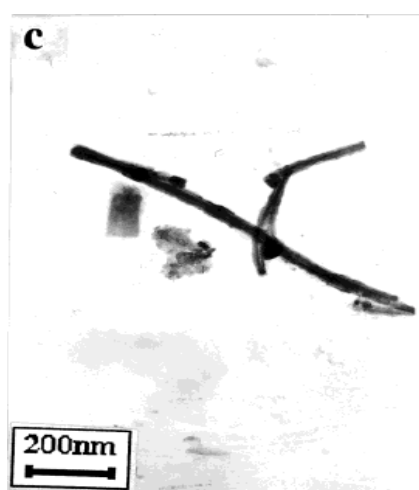
Figure 2.11 TEM image of CIS nanorod. **[39]**

Xiao *et al.* **[69]** extended the solvothermal pathway to chalcopyrite quaternary

semiconductor $CuIn(Se_xS_{1-x})_2$ nanocrystallities with composition x ranging from 0 to 1 using $CuCl_2 \cdot 2H_2O$, $InCl_3 \cdot 4H_2O$, Se and S as reactants. In their system, ethylenediamine was selected as the solvent due to its strong basic capacity, strong chelation, and its ability to act as an absorber of the excess heat produced in the reaction. UV-Vis absorption spectra indicate that the absorption energy varies linearly with the Se/S ratio (as shown in Figure 2.12).
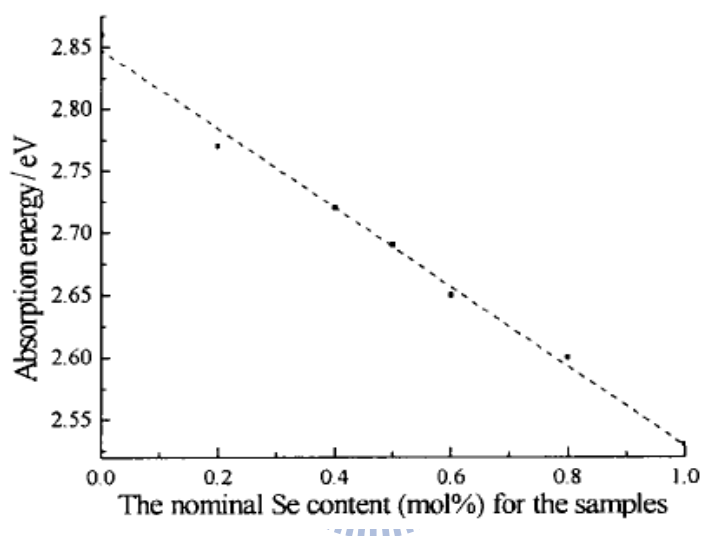
Figure 2.12 The dependence of absorption energy on the norminal Se content (mol %) for the samples. **[69]**

2.3.2 Single-source precursor

Colloidal synthesis of nanoparticles provides better control over morphology and size than other methods, particularly for very small particles. Single-source precursors are attracted great intention due to controllable and specific properties. Single-source precursors are discrete molecules that include all the elements required in the final materials these precursors can be designed with many properties in mind, including stoichiometry, solubility, and volatility.

Castro *et al.* synthesized CIS and CISe nanocrystals through single-source precursors in 2003, **[70]** using $(PPh_3)_2CuIn(SEt)_4$ and $(PPh_3)_2CuIn(SePh)_4$ (scheme

and molecular structure are shown in scheme 2.1 and Figure 2.13). Although the particle size of CIS they synthesized is not small enough (larger than 8.1 nm) to exhibit size quantization effects, these precursors provide a route to colloidal chalcopyrite QDs.
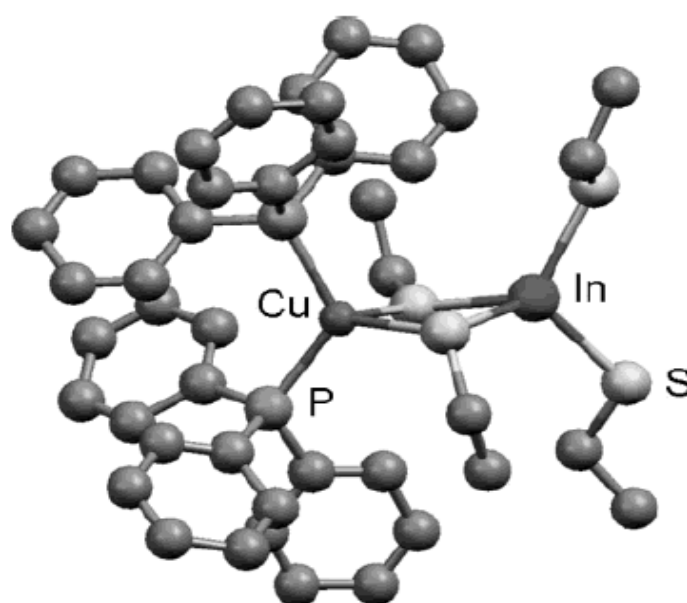
Figure 2.13 Molecular structure of $(PPh_3)_2CuIn(SEt)_4$. **[70]**
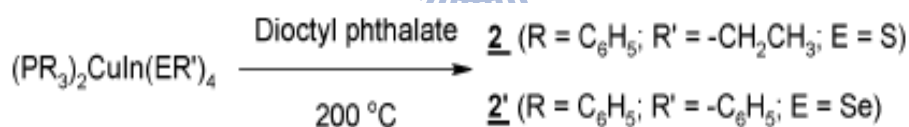
Scheme 2.1 Reaction scheme for the conversion of the single-source precursors to CuInS$_2$ and CuInSe$_2$

It is well-established that quantum confinement in semiconductors (i.e. increasing bandgap energy with decreasing semiconductor dimension) takes place at particle dimensions smaller than the Wannier-Mott (WM) exciton of the corresponding macroscopic bulk phase. **[71]** by knowledge of the high frequency dielectric constant, ε_∞, and the reduced effective exciton mass, $\mu = 1/(\mu_e^{-1} + \mu_h^{-1})$, one can calculate the WM-exciton Bohr radius according to $R_B = (\varepsilon_\infty/\mu) a_B$, with a_B being the Bohr radius of the hydrogen atom (0.53 A). Taking the CIS bulk values **[72]** of $\varepsilon_\infty = 11$, $\mu_e = 0.16$ and $\mu_h = 1.3$, the WM-exciton size of CIS was calculated to

be 8.1 nm.

In 2004, they successfully synthesized CIS nanocrystals smaller than 8.1 nm by modifying experiment condition. [73] The average size of these CIS nanocrystals varied from 2 nm, 2.68, and 3.35 nm with increasing temperature $200^{o}C$, $225^{o}C$, and $250^{o}C$ (Figure 2.14). The absorption of these nanocrystal solutions show a broad shoulder with a long tail to lower energies, both significantly shifted from the bulk band-gap absorption of CIS (1.5 eV), resulting from quantum confinement. Shown in Figure 2.15(a) are typical absorption, emission, and photoluminescent excitation spectra for solutions of CIS colloidal nanocrystals.
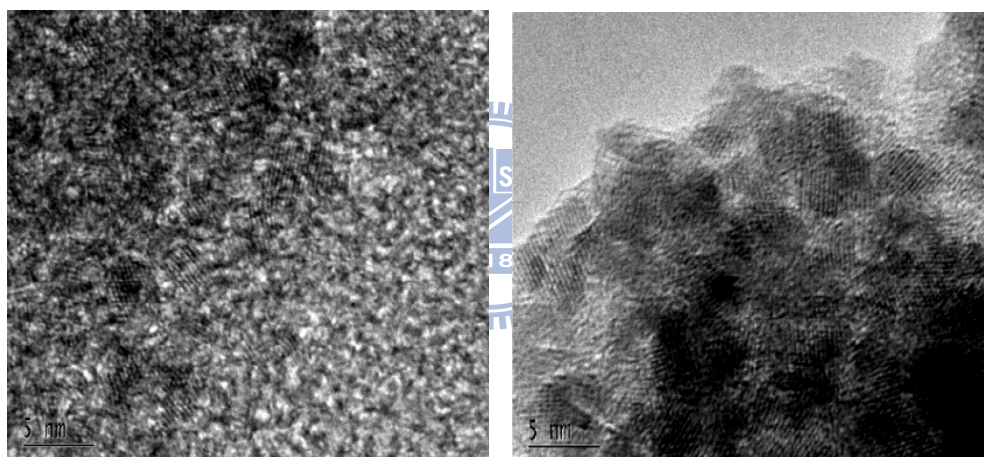
Figure 2.14 TEM images of CuInS$_2$ nanocrystals grown at 225 and $250^{o}C$. Scale bars in the images are both 5 nm. [73]

Based on their study, the nature of the surface ligands plays an important role in the PL efficiency of CIS nanocrystals. As has been observed for CdSe nanocrystals, surface defects provide sites for charge trapping, leading to nonradiative recombination of the electron and hole and quenching of the fluorescence emission. Passivation of these sites with a strong ligand leads to increased quantum yield, while a weak ligand further increases the quenching effect. As can be seen in Figure 2.15(b),

the PL efficiency is strongly affected by the nature of the surface ligands, which implies that the surface ligands of the nanocrystals provides a significant source of defects or unpassivated sites where nonradiative recombination can take place.
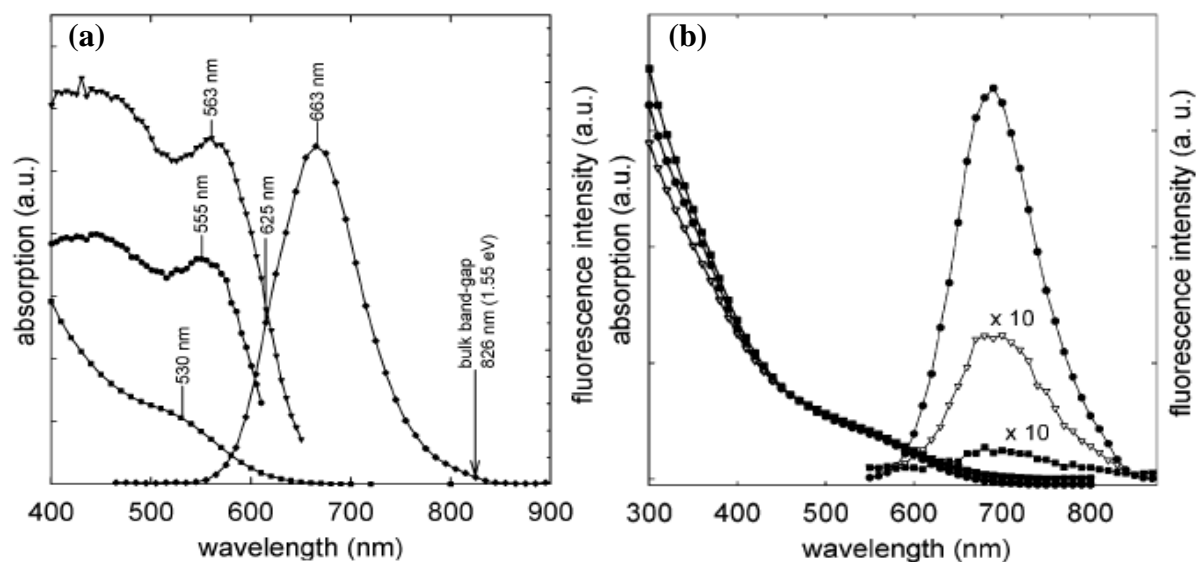
Figure 2.15 (a) Absorption, fluorescence emission, and photoluminescent excitation spectra of a typical colloidal solution of CIS nanocrystals. **(b)** Absorption and fluorescence emission spectra of CIS with hexanethiol, TOPO, and pyridine organic capping ligands (from top to bottom). **[73]**

Nairn *et al.* have also found the similar effect (Figure 2.16) in 2006, **[74]** which synthesized CIS nanocrystals through single-source precursor photolysis. They prepared the molecular precursors $[(TOP)_2CuIn(SR)_4]$ (TOP = $(octyl)_3P$; R = *n*-Pr, *t*-Bu) in organic solvent such as DOP, and then irradiated the precursors with a medium pressure Hg arc lamp (200 W/in.). The gradual color transition of the solution changed from colorless to yellow to orange and ultimately orange-red, as shown in Figure 2.17. The PL properties of CIS nanocrystal are complex due to its complicated defect chemistry from variation in molecularity ([Cu]/In) and stoichiometry ([S]/[Cu]). Examples of defects are copper and indium vacancies and interstitials, and excess or deficient sulfur occupancy. CIS can be prepared as either n- or p-type conductivity by varying the atomic ratios. High-quality crystalline material
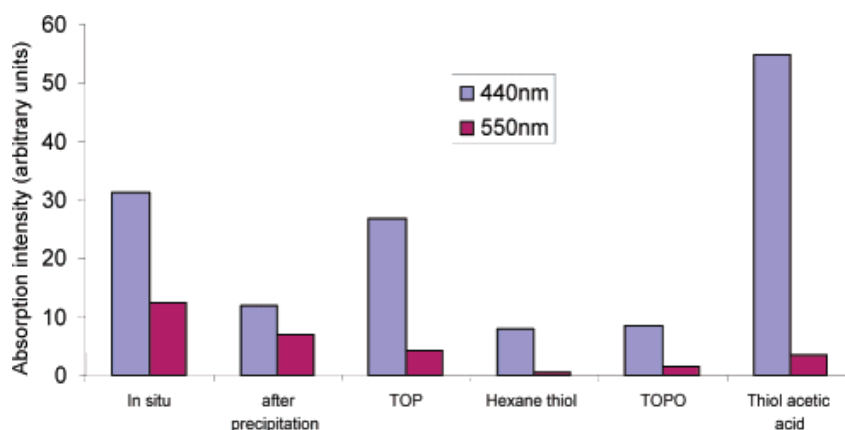
Figure 2.16 Effect of different capping agents on the emission intensities of CIS nanocrystals generated from the photolysis. **[74]**

of both conductivity types displays narrow band-edge emission between 1.5 and 1.55 eV, consisting of up to 10 narrow lines. These transitions arrive from recombination of free excitons, excitons bound to neutral or ionized donors and acceptors, and donor-valence band pairs; Figure 2.18 shows these energy levels and transitions. Based on the large difference between the absorption and the emission peaks and the observation of the PL at room temperature, it is concluded that PL of these CIS nanocrystals is broad-band, or donor-acceptor defect based, in nature. It is not surprising that CIS synthesized at a very low temperature would have many defects. It is difficult to grow CIS that exhibits near-edge PL, and that materials is synthesized at 700-900°C
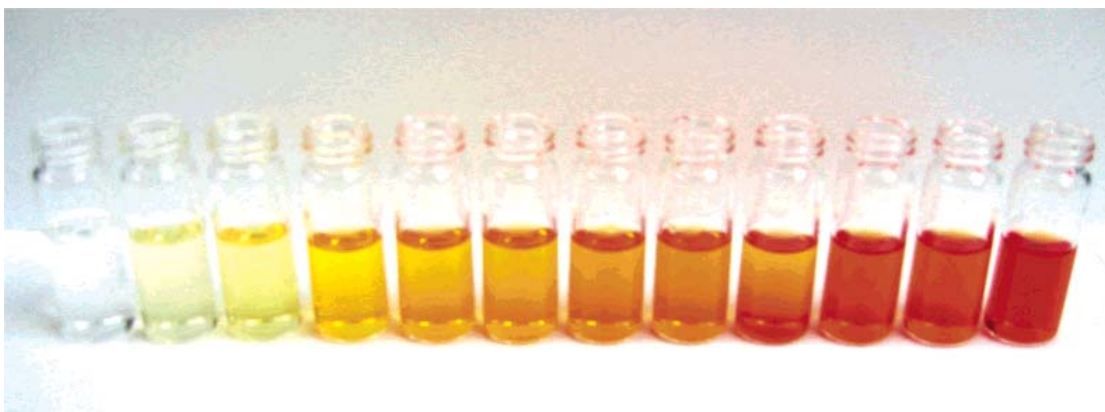
Figure 2.17 Vials of samples from the irradiation of solution of precursor [(TOP)$_2$CuIn(SR)$_4$] in DOP for (from left to right) 0, 2, 4, 6, 8, 11, 21, 30, 50, 74, 214, and 218 h. **[74]**
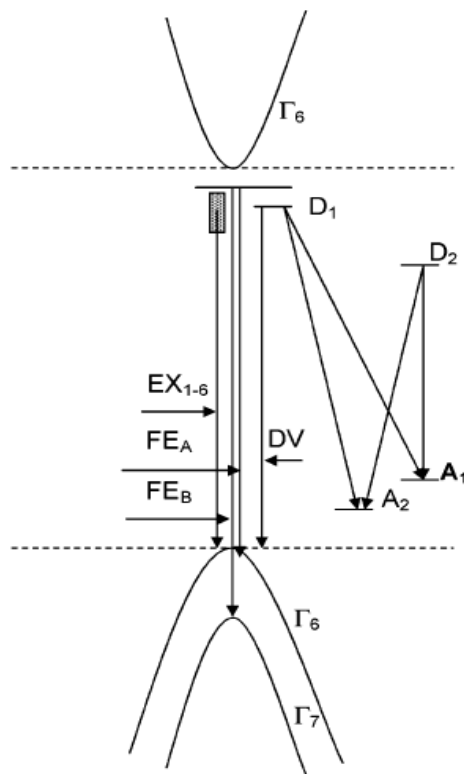
Figure 2.18 Schematic diagram of the energy levels and transitions that have been observed in single-crystal CIS. **[73]**

2.3.3 Hot-Injection

Development of colloidal routes enable low-cost fabrication of inorganic solar cells through a wet-chemistry process of semiconductor nanocrystal colloidal solution has attracted a great deal of attention. It has been known that crystal structure, composition, and size of the nanocrystals may significantly affect their optoelectronic property and device performance. Although the structure of nanocrystals can be generally controlled by the capping ligands used, the reported Cu-In-S nanocrystals are still limited to the chalcopyrite structure. Nevertheless, composition of current Cu-In-S nanocrystals is mainly controlled by using a single ternary precursor. In spite of the use of a single-source precursor is convenient, this method is limited by the precursor availability and their tedious procedure.

In 2006, Nakumura *et al.* introduced Zn into CIS system with a kind of hot-injection method and enhanced their PL intensity. **[75]** The particle size varied from 2.6 to 4 nm with increasing Cu/Zn ratio, both the absorption and emission peaks also show red-shifted with increasing Cu/Zn ratio (Figure 2.19).
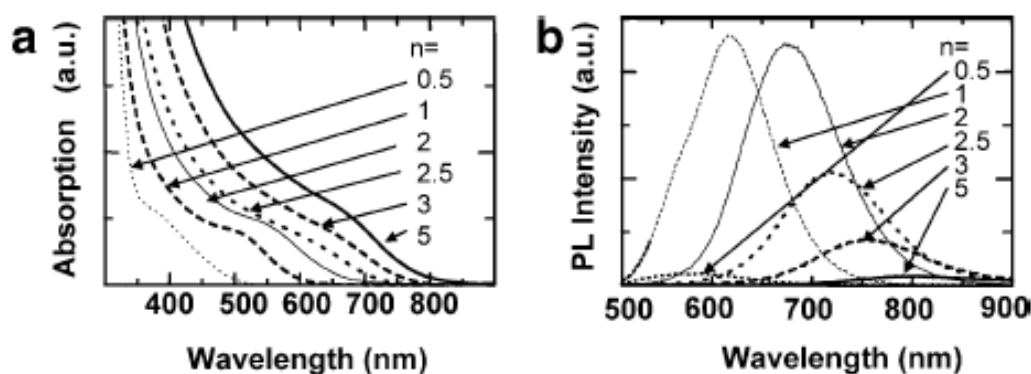
Figure 2.19 Raw material composition effects on optical properties: (a) UV-vis absorption and (b) PL emission spectra (excitation 500 nm). (Raw material composition Zn:Cu;In:S = 1:n:n:4 (n = 0.5-5).) **[75]**

In a chalcopyrite CIS, the Cu-S bond is weaker than that of In-S and the Cu vacancy is preferably generated. In addition, the Cu vancancies induced anti-site defect generation **[76]** and the ionic diameters of Cu and Zn are similar. On the basis of reasons above, Zn preferentially substituted to Cu and prevented anti-site defects. Therefore, introduction of Zn ion into CIS nanocrystals was predicted to improve the PL intensity. Furthermore, the band-gap was controlled by this Zn content. The wide selectivity in components and composition by this method suggest a new series of chalcopyrite-type semiconductor nanocrystals with various properties.

Different crystal structures were obtained through a hot-injection method on Cu(dedc)$_2$ and In(dedc)$_3$ precursors (dedc is diethyldithiocarbamate.), with tunable [Cu]/[In] composition. **[77]** Zincblende CIS nanocrystals can be obtained by the co-decomposition of Cu(dedc)$_2$ and In(dedc)$_3$ in the presence of oleic acid. Similarly, wurtzite CIS nanocrystals can be prepared by the co-decomposition of Cu(dedc)$_2$ and In(dedc)$_3$ in the presence of dodecanethiol. The formation of CIS nanoparticles may

involve possible reaction routes illustrated in Scheme 2.2: the reaction of CuS or Cu_2S from the decomposition of the $Cu(dedc)_2$ in the presence of oleic acid or dodecanethiol with In_2S_3 from $In(dedc)_3$, respectively, results in the formation of zincblende and wurtzite CIS nanocrystals.

$$In(dedc)_3$$
$$Cu(dedc)_2 \xrightarrow{\text{Oleylamine}} 2CuS + In_2S_3 \xrightarrow[\text{Oleylamine}]{\text{Zincblende}} 2CuInS_2 + S$$
$$\Downarrow \text{Dodecanethiol}$$
$$Cu(dedc) \xrightarrow{\text{Oleylamine}} Cu_2S + In_2S_3 \xrightarrow{\text{Wurtzite}} 2CuInS_2$$
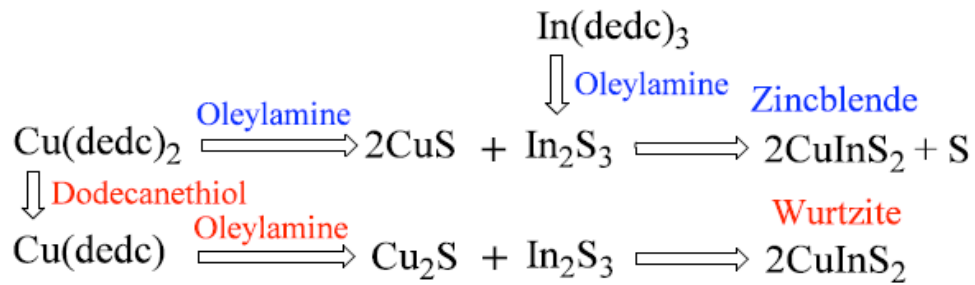
Scheme 2.2 Schematic formation mechanism of CIS from $Cu(dedc)_2$ and $In(dedc)_3$ precursors. **[77]**

This study correlates the crystalline structure of the binary ZnS nanocrystals with those of ternary Cu-In-S nanocrystals, demonstrating the feasibility fabrication their alloyed or core/shell structures.

Chapter 3

Experiment

3.1 Chemicals

Copper(I) chloride (CuCl, 95%, analytical reagent), indium(III) chloride (InCl$_3$, 98%, AR), sulfur powder (99.5%, chemically pure), Zinc stearate (10~12% as Zn, technical) and trioctylphosphine (TOP, 90%, technical grade) were purchased from Sigma-Aldrich Corp.; octadecene (ODE, 90%, technical grade) and oleylamine (70%, technical grade) were purchased from Tokyo chemical industry Co., Ltd. Diethyldithiocarbamic acid zinc salt ([(C$_2$H$_5$)$_2$NCSS]$_2$Zn, technical grade), zinc nitrate hexahydrate (Zn(NO$_3$)$_2$ · 6H$_2$O), methenamine (C$_6$H$_{12}$N$_4$), mercaptopropionic acid (MPA) were purchased from Sigma-Aldrich Corp.

3.2 Characterization

3.2.1 Structure and morphology

X-ray diffraction (XRD)

The resulting powder collected from the solutions was examined using X-ray powder diffraction (XRD, M18XHF, Mac Science, Japan) to identify the crystallographic phase of nanocrystals, with Cu Kα radiation (λ=0.15405 nm) (40kV, 200 mA), 2θ ranging from 10° to 70° at a scanning rate of 10°/min.

Transmission electron microscope (TEM)

TEM images were obtained using a JEOL 2010 transmission electron microscope operating at 200 kV. Samples for the TEM were prepared by depositing a drop of the samples dispersed in toluene onto a carbon grid. The excess liquid was wicked away with filter paper, and the grid was dried in air.

X-ray photoelectron spectroscopy (XPS)

XPS measurements were carried out using a Field Emission – Auger Electron Microprobe (Thermo VG Microlab 350) x-ray photoelectron spectrometer using an Mg Kα x-ray as the excitation source.

3.2.2 Optical measurement

Then UV‑vis, PL emission, and excitation (PLE) spectroscopy was applied using a UV‑vis spectrophotometer (UV-1600; Agelent 8453) and a spectrofluorometer (FP-6600; Jasco, Inc., Japan). For these observations, the products were precipitated with alcohol. They were further isolated by centrifugation to remove excess surfactants. The centrifuged particles were redispersed into an organic solvent such as toluene to yield a clear and colloidally stable suspension. The amounts of Zn-CIS absorbed on the ZnO films were measured with an UV-visible-NIR spectrophotometer (JASCO V-570) equipped with an integrating sphere (JASCO ISN-470).

3.3.3 Solar parameter measurement

Measurements of *IV* curves were made with a digital source meter (Keithley 2400, computer-controlled) with the device under one-solar AM 1.5 irradiation of a solar simulator (Newport-Oriel 91160) calibrated with a Si-based reference cell (Hamamatsu S1133) and a IR-cut filter (KG5) to correct the spectral mismatch of the lamp. The Zn-CIS/ZnO devices were operated in a back-side illumination fashion with the transparent counter electrode masked by a black plastic tape of the same size with a round hole to allow the actively illuminated area of 0.28 cm^2 for all measurements. Time-resolved measurements were performed with a tunable nanosecond optical-parametric-oscillator/Q-switch-pumped neodymium doped

yttrium aluminum garnet laser system NT341/1/UV, Ekspla. Emission transients were collected with a monochromator SpectraPro-300i, ARC, detected with a photomultiplier tube R928HA, Hamamatsu connected to a digital oscilloscope LT372, LeCroy, and transferred to a computer for kinetic analysis.

3.2.4 High frequency magnetic field set up

A high frequency (50-100 kHz) magnetic field (HFMF) was applied to the precursors to provide kinetic energy for Zn-CIS nanocrystal synthesis. The HFMF was created by a power supply, function generator, amplifier, and cooling water. Similar equipment was also reported in PNAS, vol. 103, 3540–3545 (2006). The strength of the magnetic field depended on the coils. In this study, the coil was 8 loops, the frequency was 50 kHz and the strength of magnetic field (H) was 2.5 kA/m. The temperature of HFMF generator was controlled by cycling cooling water at 25 ^{o}C.

Hysteresis loop analysis

Measurements of magnetization (M) versus applied field H and temperature T were carried out using a commercial SQUID (superconducting quantum interference device) magnetometer (MPMX-XL7).

3.3 Material fabrication

3.3.1 Synthesis of CuInS$_2$ nanocrystals

The CIS nanocrystals were prepared using a high-temperature organic solvent process. First, sulfur was dissolved in TOP. The solution was diluted with ODE to form a clear solution (solution 1). Then, CuCl and InCl$_3$ were dissolved in oleylamine at 50°C to form another solution (solution 2). These two material solutions were mixed to produce a raw material solution. A small aliquot of raw material solution was put into

a test tube and soaked directly in an oil bath that had been preheated to 240°C and aged for 300s. The prepared solutions were limpid, reflecting their high colloidal stability.

3.3.2 Synthesis of CuInS$_2$@ZnS core/shell nanocrystals

Preparation of the CIS@ZnS core/shell nanocrystals was achieved by modifying the above reaction system and surface coating of ZnS. Zinc stearate (ZnSt) and sulfur were each dissolved in TOP (solutions 3 and 4). After the colloidal solution of CIS nanocrystals was preheated to 240°C, solutions 3 and 4 were injected into the solution for 300s. Subsequently, the mixture was cooled to 90°C to form the ZnS shell on the surface of CIS nanocrystals. Repeating the injection step were also used to grow the multiple ZnS layers on the CIS nanocrystals. The product was diluted with toluene and PL spectra were measured.
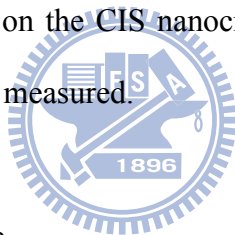
3.3.3 Systhesis of ZnO nanowire

The ZnO thin films were deposited on F-doped SnO$_2$ (FTO, 30 Ω/sq, Sinonar, Taiwan) substrates by RF magnetron sputtering as followed from our previous report.[126] The seeded substrates were then suspended horizontally in a reagent solution containing 0.016 M zinc nitrate and 0.025 M methenamine and heated to 95°C to initiate nanowire growth.

3.3.4 Synthesis of Zn-CIS quantum dots

The Zn-CIS QDs were prepared using a high-temperature organic solvent process. 0.5 mmol diethyldithiocarbamic acid zinc salt was dissolved in 6 ml TOP. The solution was diluted with 24 ml ODE to form a clear solution (solution 1). Then, 0.2 mmol CuCl and InCl$_3$ were dissolved in 6 ml oleylamine at 50°C to form another solution

(solution 2). Here, amine coordinates the Cu and In ions to produce amine complexes. These two material solutions were mixed to produce a raw material solution with a ratio Zn:Cu:In:S = 1:n:n:4 (n=1 in this composition), the composition ratios of Cu and In were varied from 1 to 3. Those of Zn and S precursors were fixed in concentration, indicated as Zn:Cu:In:S = 1:n:n:4 (n=1-3). A small aliquot of raw material solution was put into a test tube and soaked directly in an oil bath that had been preheated to 240°C and aged for 300s. The prepared solutions were limpid, reflecting their high colloidal stability.

3.3.5 ZnS coating of Zn-CIS quantum dots

A colloidal solution of ca. 20 mg of Zn-CIS nanocrystals with an average diameter of 3.6 nm in 4 mL of toluene was placed in a three-neck flask under purified argon flow. After addition of 2.5 mL of TOPO, the mixture was heated to 190 °C and then kept at this temperature till a complete heptane evaporation. Zinc stearate (316 mg) was dissolved in 2.5 mL of toluene upon gentle heating (ca. 60 °C). After cooling to room temperature, the resulting 0.2 M solution was mixed with 2.5 mL of a 0.2 M solution of Se in TOP. By means of a syringe pump this mixture was injected within 1 h into the reaction flask containing the core nanocrystals at 190-200 °C. Periodically small aliquots were removed in order to monitor the shell growth. After the addition was completed the crystals are annealed at 190 °C for an additional 1-1.5 h.

3.3.6 Synthesis of hydrophilic quantum dots by ligand exchange

Purified QDs were dissolved in a minimum amount of chloroform and excess mercaptopropionic acid (MPA) was added until the solution became cloudy, and stirred at 55°C for one night in argon atmosphere. After that, 1mL of tetrahydrofuran (THF) was added to stop the surface exchange reaction. After cooling to room

temperature, a suspension of potassium t-butoxide in THF was added to neutralize the carboxyl acid function, and then centrifuged to remove the by-products with THF. The THF washing process was repeated for 2-3 times, and finally distilled water was added to disperse hydrohilized Zn-CIS NCs into water.

3.3.7 Assembling Zn-CIS quantum dots on ZnO Nanowires

Fire ZnO plate at $450^{\circ}C$ for 30 minutes and then after cooling in air for 5 minutes, transferred ZnO plate to ZCIS solution and left for 3 days to ensure saturated adsorption of Zn-CIS QD onto the ZnO nanowires.

3.3.8 Fabrication of solar cells

For characterization of the photovoltaic performance of our devices, the Zn-CIS/ZnO films were served as working electrode (anode); a fluorine doped tin oxide glass (typical size 1.0×2.0 cm^2) coated with platinum (Pt) particles by sputtering was used as a counter electrode (cathode). The two electrodes were assembled into a cell of sandwich type and sealed with a hot-melt film (SX1170, Solaronix, thickness 25 μm); a thin layer of electrolyte was introduced into the space between the two electrodes and the device was fabricated accordingly. A typical redox electrolyte contained 0.1 M lithium iodide (LiI), 0.01 M iodine (I$_2$), 0.5 M 4-*tert*-butylpyridine (TBP), 0.6 M butyl methyl imidazolium iodide (BMII), and 0.1 M guanidinium thiocynate (GuNCS) in a mixture of acetonitrile (CH$_3$CN, 99.9%) and valeronitrile (n-C$_4$H$_9$CN, 99.9%) (v/v = 15/1)

3.3.9 Synthesis of Zn-CIS nanocrystals in the presence of high frequency magnetic field

0.5 mmol diethyldithiocarbamic acid zinc salt was dissolved in 6 ml TOP. The

solution was diluted with 24 ml ODE to form a clear solution (solution 1). Then, 0.2 mmol CuCl and $InCl_3$ were dissolved in 6 ml oleylamine at 50^oC to form another solution (solution 2). Here, amine coordinates the Cu and In ions to produce amine complexes. These two solutions were mixed to produce the raw material solution. A small aliquot of raw material solution was put into a test tube and exposed to HFMF with an input power of 90 W (**Figure 6.1**). The color of the mixture solution was changed with different durations of HFMF exposure from yellow (30 sec), red (45 sec) to black (120 sec). The resulting precipitated powders were collected via centrifugation at 6000 rpm, removed from the solution, and repeated three times to remove excess surfactants which were precipitated using methanol.

3.3.10 Fabrication of Zn-CIS thin film solar cells

The Mo coated soda lime glass substrates used here was fabricated by dc magnetron sputtering at Ar pressures 1.5 mTorr resulting in a 200 nm layer. Deposition of the CIS absorber layer on top of the Mo substrates is used drop casting by the nanoink solution and subsequent thermal treatments to remove the organics and sinter the films under Ar and Se atmospheres at 500 ^oC respectively. A ~ 50 nm CdS layer is then deposited by a chemical bath deposition (CBD) technique. The CBD bath contains 183 ml of deionized H_2O, 25 ml of 0.015 M $CdSO_4$ solution, 12.5 of 1.5 M thiourea solution, and 31.25 ml of stock NH_4OH (Aldrich). Next, A ~50 nm high resistivity i-ZnO film capped with a ~300 nm high conductivity ITO layer are deposited by RF magnetron sputtering. The ZnO film is sputtered in a mixture of 10% O_2 in Ar at sputtering pressure of 10 mTorr with no intentional heating. The ITO layer is sputtered with neither O_2 nor intentional heating at sputtering pressure of 1 mTorr. After sputtering of the oxide layers, the final device is baked in air at 200 ^oC over night.

Chapter 4

Synthesis and Characterization of Highly Luminescent CuInS$_2$ and CuInS$_2$/ZnS (Core/Shell) Nanocrystals

4.1 Introduction

CuInS$_2$ is one of the most important I-III-VI$_2$ semiconductor materials for use in photovoltaic solar cells and it has many notable advantages such as an appropriate band gap, a high absorption coefficient, and good thermal, environmental, and electrical stability. [78-80] Also, some research aims to apply chalcopyrite materials in "spintronics" as tailorable ferromagnetic materials. [81-84] However, chalcopyrite NCs have not been systematically investigated and relatively few studies [70, 73, 75, 85-86] have achieved particle sizes small enough to exhibit quantum confinement (the Wannier-Mott bulk exciton of the CuInS$_2$ is 8.1 nm [86]). Although Nairn et al. combined single source precursors and photolysis methods to obtain CuInS$_2$ NCs ~2 nm in diameter, the photoluminescence (PL) in these chalcopyrite NCs were not so strong as the well-developed II-VI group semiconductor NCs (CdSe, CdS et al.). [85] Nakamura and coworkers modified the high-temperature organic solvent method and successfully introduced Zn into the CuInS$_2$ NCs to achieve tunable band-gap energies (Eg) and PL. Compared to the pure CIS NCs prepared by a similar method, it was found that the quantum yield for the Zn-CIS alloy (~5%) was still much less than that of CdSe. [76]

Expansion of typical II-VI group semiconductor NCs such as CdSe and PbS are necessary because of the "Restriction of the Use of Certain Hazardous Substance (RoHS)" in Europe. Based on considerations of environmental and human toxicity, biological studies confine these NCs to specific fields. Luminescent CIS NCs are sought as new candidates for building blocks of nanomaterials and biological tabs

though quantum efficiency and photostability has been improved. Up to now, wide-band gap materials such as CdS, ZnS, and ZnSe have been widely used as shells to enhance the photoluminescence quantum yield by passivating surface nonradiative recombination sites. **[87-89]** However, no systematic studies have been reported on surface coatings on I-III-VI$_2$ type chalcopyrite semiconductors and core-shell structures although Nakamura and co-workers mentioned that ZnS deposition on the surface of Zn-CIS alloy NCs could improve the PL intensity. **[75]**

In the CIS/ZnS NCs system, ZnS was chosen to coat the CIS to form CIS/ ZnS core shell NCs, the facile synthesis and luminescent properties of monodisperse CIS, and CIS/ZnS (core-shell) NCs were investigated. In addition, x-ray diffraction, x-ray photoelectron spectroscopy, dynamic light scattering, and transmission electron microscopy were used to analyze the composite NCs and determine their chemical composition, average size, size distribution, shape, and internal structure.

4.2 Formation and microstructure of CuInS$_2$

Figure 4.1 shows the XRD patterns of the as-prepared CIS and CIS/ZnS core/shell NCs. The powder patterns for ZnS and CuInS$_2$ are also shown for comparison in the bottom and top inset. In Figure 4.1(a), there is an intense peak at $2\theta=27.8^o$, oriented along the (112) direction and other prominent peaks observed at 46.5^o (204) and 54.8^o ((312)/(116)), which are signatures of the chalcopyrite structure of CIS. The location of the pattern is in good agreement with the JCPDS reference diagrams in the bottom inset (JCPDS No. 32-0339). Similar features are observed for CIS/ZnS core–shell NCs but the latter exhibit an enhanced intensity in XRD peaks, which could result from the contribution of both ZnS and CIS. In the range between 15° and 25°, a broad halo appears, probably due to an amorphous contribution. This may indicate that the organic ligand TOP is still present, and may

not have been removed completely in processing.
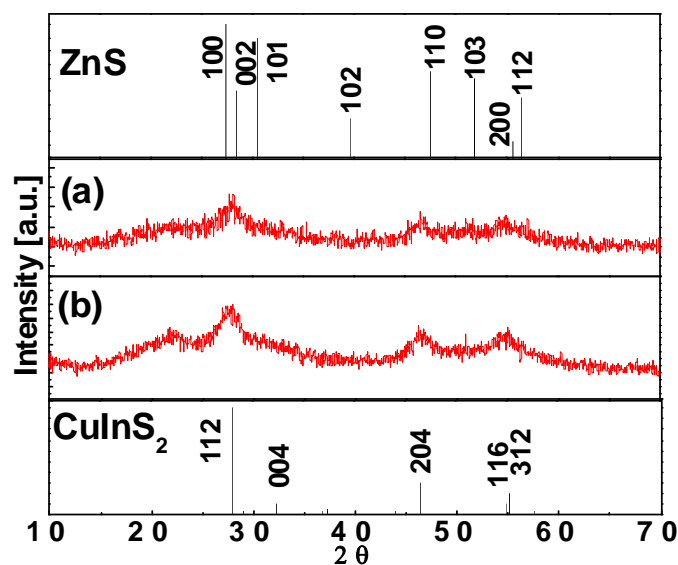
Figure 4.1 (a)XRD patterns of pure CIS and (b) CIS/ZnS (coe/shell) NCs as well as the standard data for ZnS (vertical bars, JCPDS card No. 10-0434) and CIS. (vertical bars, JCPDS card No. 32-0339).

Figure 4.2 shows the TEM images of the as-prepared CIS NCs and particle size distribution. In Figure 4.2(a), it can be seen that the resultant CIS NCs are uniform spherical-shaped particles with a very narrow size distribution (Fig 4.2(d) and 4.2(e) show the result of DLS analysis). Figure 4.2b shows a high-resolution TEM (HRTEM) image of the CIS NCs. It demonstrates the high crystallinity of the CIS NCs. The distances (0.31 nm) between the adjacent lattice fringes are the interplanar distances of CIS (112) plane, agreeing well with the (112) *d* spacing of the literature value of 0.319 nm (JCPDS NO.32-0339). Furthermore, after the growth of the ZnS shell, the image in Figure 4.2(c) shows slight differences in contrast between the core and the outer part, whereas it is hard to identify the structural differences between the core and the shells by comparing the contrast in the TEM image. However, the shell thickness can be roughly determined by the size difference between the average size of CIS/ZnS core/shell NCs (4.6±0.5nm), which is larger than that of the core CIS NCs

(2.4±0.5nm). The difference in particle size indicates that the shell thickness is around 1.1 nm.
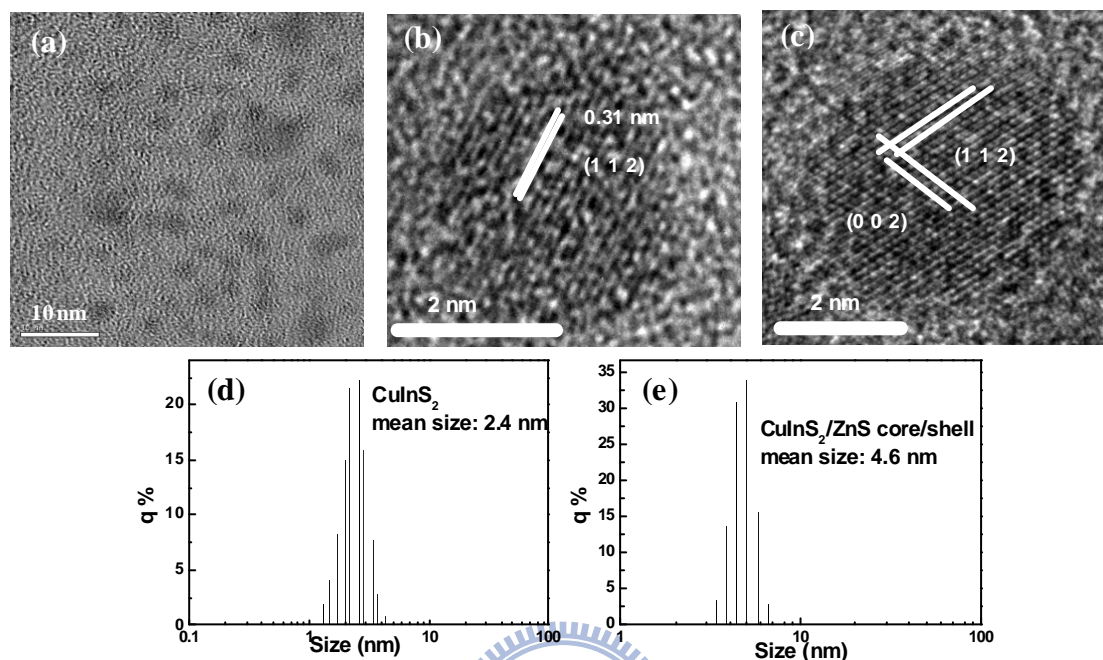
Figure 4.2 (a)TEM image, and (b) HRTEM image of CIS, as well as (c) HRTEM image of CIS/ZnS NCs. Particle size distribution histograms of (d) CIS, and (e) CIS/ZnS NCs.

The X-ray photoelectron spectra (XPS) were employed to investigate the surface compositions and chemical state of CIS and CIS/ZnS core/shell NCs. The results are shown in Figure 4.3(a) and 4.3(b), respectively, indicating the presence of Cu, In, Zn, and S, as well C from reference and O impurity. The spectra could be considered to be primarily contributed from the shell material, since XPS is a surface-sensitive technique. The peak of the Zn 2p3/2 in 3b is larger than that of the CIS/ZnS NCs, which can explain the formation of the ZnS shell to some extent.
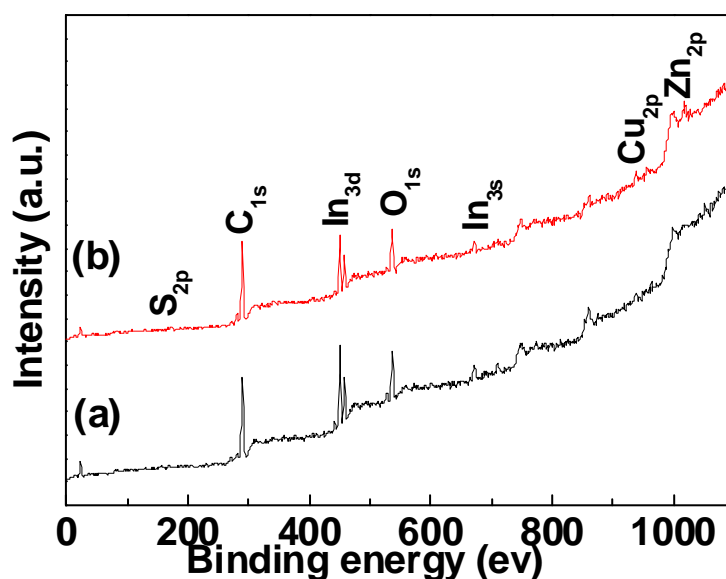
Figure 4.3 XPS of CIS (a) and CIS/ZnS (b) core/shell NCs.

4.3 Photoluminescence (PL) of the CuInS$_2$ Nanocrystals.

Figure 4.4 displays the photoluminescence behavior of as-prepared CIS NCs dispersed in a toluene solution. It was observed that the emission spectrum under excitation wavelength 366 nm is a slightly broad band centered around 450 nm. It has been previously reported that addition of TOP enhances the 450 nm emission band and quenches the 550 nm band. **[74]** The peak intensity of this emission band is significantly higher than that of bulk CuInS$_2$ (>810 nm) due to the size-dependent quantum confinement effects. However, the weak intensity of PL is due to the surface defects in these nanoparticles, which is in agreement with the report of Castro et al. who attributed this emission band to broad-band, defect-related transitions. **[73]** In addition, the PL intensity of the CIS NCs can be considerably improved by surface passivation with an inorganic or organic (amine) shell. ZnS is the shell material of choice as it provides good confinement of both electrons and holes in the core. Figure 4.5 demonstrates the photoluminescence emission spectra of CIS and CIS/ZnS

core/shell NCs. To identify if the enhancement of PL is contributed from pure ZnS or the ZnS shell on the CIS NCs, PL properties of a pure ZnS sample was also measured for comparison with CIS and CIS/ZnS core/shell NCs. It can be seen that the PL emission intensity was much enhanced with a ZnS coating and a small shift in the PL spectra to the red (lower energies) was observed after surface coating due to partial leakage of the exciton into the ZnS matrix. This red shift is more pronounced in smaller dots where the leakage of the exciton into the ZnS shell has a more dramatic effect on the confinement energy of the charge carriers. In addition, it was evidenced from UV-vis absorption measurement and found that with increasing ZnS coverage, the absorption in the ultraviolet was shifted as a result of direct absorption into the higher band gap ZnS shell (inset in Fig. 4.4).
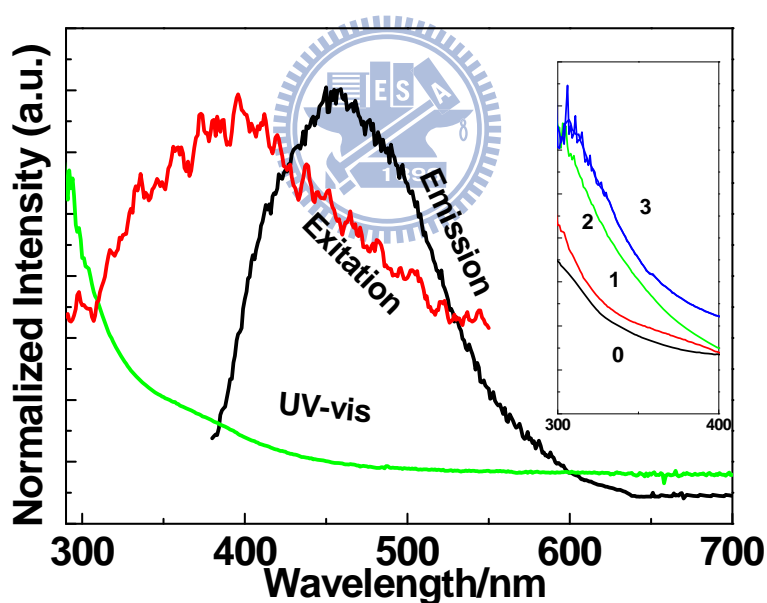
Figure 4.4 Uv-vis absorption, excitation and PL emission spectras of CIS NCs. The inset highlights the ultraviolet region spectra showing an increased absorption at higher energies with increasing coverage due to direct absorption into the ZnS shell.

The PL intensity reaches its maximum value at approximately ~2 monolayers of coverage, indicating that most of the surface vacancies and nonradiative recombination sites are passivated. However, it was found that PL peak intensity was decreased with increasing ZnS coatings over 2 monolayers. The generated defects in

the ZnS shell may be the source of new nonradiative recombination sites, which causes the decline of PL quality with thicker ZnS shell growth in this study. The most likely possibility is that the growth is initially coherent at low coverage, but as the thickness of the shell increases, the strain due to the lattice mismatch between CIS and ZnS could lead to the formation of dislocations and low-angle grain boundaries, relaxing the structure, and causing the growth to proceed incoherently. These defects could be the source of nonradiative recombination sites within the ZnS shell. Similar behavior was also reported for ultrathin CdSe/ZnSe quantum wells. **[89]**
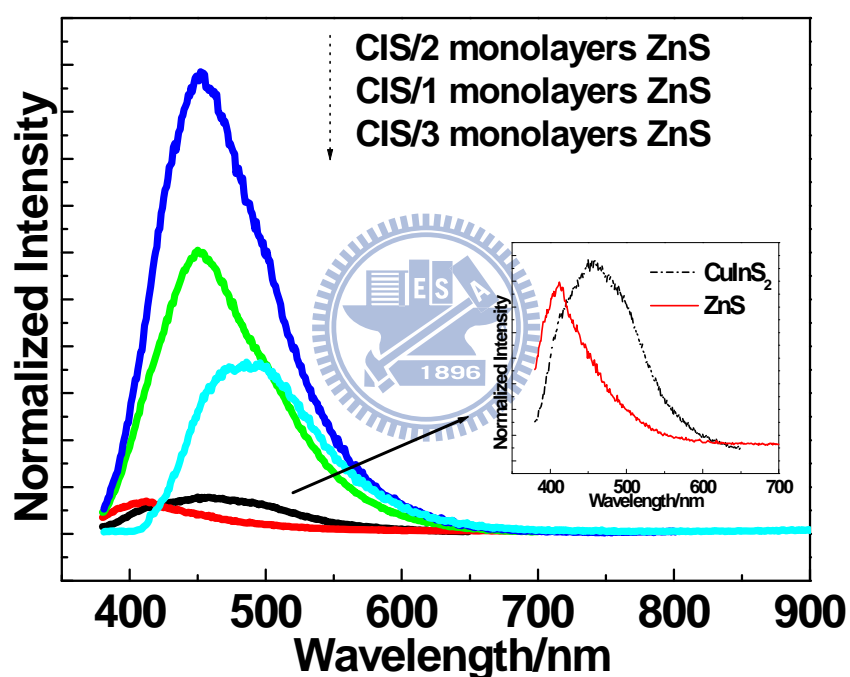
Figure 4.5 PL emission spectra of CIS and multi-layers ZnS coating on the surface of CIS NCs. PL emission spectra of pure ZnS and CIS NCs are shown in the inset of the emission spectra.

4.4 Summary

In summary, the ultrafine CIS and CIS/ZnS NC core/shells have been developed through a colloidal solvent process. The nanoparticles produced by this method are 2.4 ± 0.5 nm and 4.6 ± 0.5 nm in size. HRTEM, powder XRD, XPS and DLS measurements indicate that the NCs are uniform and crystalline. The PL intensity

could be much enhanced by the growth of a ZnS shell on CIS due to the elimination of the surface defects. These monodisperse and highly crystalline NCs can be potentially used as labels for biological molecules and as active components in optoelectronic devices.
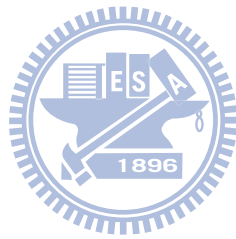
Chapter 5

Core-Shell CuInS$_2$/ZnS Quantum Dot Assembled on Short ZnO Nanowire with Enhanced Photo-Conversion Efficiency

5.1 Introduction

Recently, zinc oxide nanowires have attracted a considerable amount of research interest as potential candidates for optoelectronics applications such as nanoscale lasers, light-emitting diodes, and UV photodetectors. **[90-95]** Moreover, ZnO nanowires also have been substituted for TiO$_2$ nanoparticles as the n-type photoelectrodes in photovaltic device. **[96-97]** Wide band gap ZnO nanowires can provide direct conduction pathways for electrons to transport to the collection electrode. They also help improve electron transport by avoiding the particle-to-particle hopping that occurs in the TiO$_2$ network. Thus, ZnO nanowire can efficiently enhance the charge transport ability and efficiency, which is controversially the crux for the nanocomposite photovoltaic solar cells (PVs). Recently, a dye-sensitized solar cell (DSSC) made from solution-based ZnO nanowire has achieved a power conversion efficiency of 1.5%, **[98]** and a DSSC made from ZnO nanowire with a dendritic structure has achieved a power efficiency of 0.5%.**[99]** In both cases, the ZnO nanowires are tens of micrometer in length, which requires a longer-term growing process. While the ZnO nanowires with proper length prevent corrosion from electrolyte and efficient light-harvesting surface area, the over-length ZnO nanowires would prolong transfer pathway of electrons from light-sensitizer, resulting in increasing possibility of electron-trap by defects on ZnO surface and limiting power conversion efficiency.

The other critical challenge in nanocomposite PV applications is efficient utilization of solar energy, where about 60% of them have wavelengths longer than

700 nm. One plausible strategy is the use of semiconductor nanocrystals, known as narrow band gap quantum dots (QDs), instead of photosensitized dyes. In addition, it has been shown recently that QDs can generate multiple electron-hole pairs per photon, which could improve the efficiency of the device. **[100-103]** This concept has been demonstrated on TiO_2 or ZnO electrodes by depositing CdS **[104-105]** and CdSe. **[106-109]** For such a dye-sensitized system, QDs are known to be neutralized or corroded by an electrolyte and, therefore, such QDs solar cell performance is limited. Therefore, considering this problem, there are two fundamental ways to optimize this kind of QD-based solar cells. One requires a transition away from a liquid electrolyte to a different hole transport medium. Some researches studied on the solid **[110-111]** or gel state electrolyte **[112-117]** to be substituted for liquid electrolyte. However, their efficiency and long-term stability can not be comparable with those of the liquid electrolyte. The other is to deposit a protecting layer on the surface of QDs. Wide-band gap materials such as CdS, ZnS, and ZnSe have been widely used as shell to enhance the photoluminescence quantum yield by passivating surface nonradiative recombination sites. **[85-86, 88, 118]** Base on this concept, wide band gap shell not only can improve optical properties of QDs, but also protect them from corrosion of liquid electrolyte.

It has demonstrated that $CuInS_2$ (CIS), whose band gap energy is 1.55 eV (bulk), is a promising photosensitizer for ZnO. The band gap of CIS QDs can be tunable by Zn dopant. **[75]** From the viewpoint of band-energy engineering, ZnS is an energetically suitable medium due to its proper band gap (2.67 eV) which is believed to be able to efficiently promote electron transition between CIS QDs and ZnO nanowires. (Figure 5.1) Therefore, the ZnS is chosen as dual-functioning candidate, acting as a photosensitizer and in the meantime, to protect the Zn-doped CIS from undesirable chemical degradation in this study. More than this chemical modification,

a modified quantum dot solar cell by assembling Zn-CIS nanoparticles on single crystal ZnO nanowires using a bifunctional surface modifier is also investigated. Upon constructing the solar cell device, we believe that increase of the QDs coverage on the ZnO nanowires will surely boost the efficiency of energy conversion and on this basis, a short nanowire, i.e., 5 micrometers in length, was employed in order to testify such a hypothesis. With recent advances in using protecting layer in solar cells for efficient transport of charge carriers, it should be possible to further improve the efficiency of quantum dot solar cell.
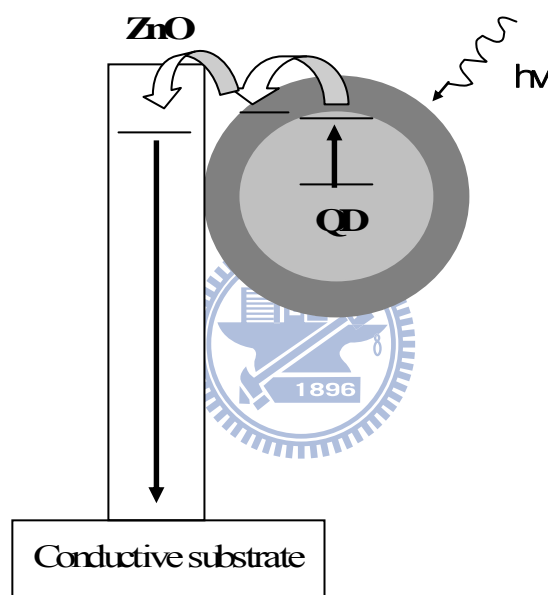
Figure 5.1 Schematic diagram of charge transfer from Zn-CIS quantum dot into ZnO nanowire.

5.2 Quantized Zn-CIS particles and their deposition on ZnO nanowires

The absorption spectra of the different-ratio Zn-CIS quantum dots employed in the present study are shown in Figure 5.2(a). These particles exhibit absorption in the visible with an onset corresponding to different Cu/Zn ratios. The shift of the onset absorption to lower wavelengths with decreasing n value represents the Zn doping effect in these particles. By comparing the excitonic transition (660, 570, 530 nm for *n*

= 3, 2, and 1, respectively.) with the absorption curve reported by Nakamura and co-workers, [75] the average particle diameter of these samples was identified as 4.4, 4.5, and 3.5 nm respectively. It is noticeable that the absorption and photoluminescence (not shown here) properties of Zn-CIS nanocrystal are not only dominated by its particle size but also the concentration of Zn doping. The Cu site in the lattice is preferentially substituted by Zn and the substitution is found to be more energetically favorable to prevent anti-site defects, which will affect the absorption spectrum. Therefore, by increasing the Cu/Zn ratio (or decreasing Zn concentration) in the reaction solution, the absorption edge shifted from ca. 400 to ca. 700 nm toward the longer wavelength. Figure 5.2(b) shows the similar absorption spectra of hydrophilic QDs after ligand exchange, which means that particle size and optical property of the QDs were not changed after surface modification compared to original QDs (in toluene). Exchange of TOP by thiols at the surface of Zn-CIS nanocrystals was accompanied by a slight blue shift of absorption spectrum. Similar phenomena were also reported for CdSe ad CdTe QDs. [5,119] The blue shift was due to a redistribution of electronic density and an increase in confinement energy induced by the stronger bond between the thiol and the Cu atoms at the Zn-CIS nanocrystal surface. These quantum dots were then deposited on ZnO nanowires for spectroscopic and photoelectrochemical investigation.

Figure 5.3(a) shows a cross-sectional scanning electron micrography of typical ZnO nanowires used as photoanodes. The nanowires are approximately 50-60 nm in diameter and ~5 μm length, indicating a relatively large surface area to accommodate high concentration of sensitizer molecules (and higher concentration of the QD deposition). All the samples used in this study displayed good stoichiometric composition and crystallinity according to the XRD and XPS analyses (not shown here).
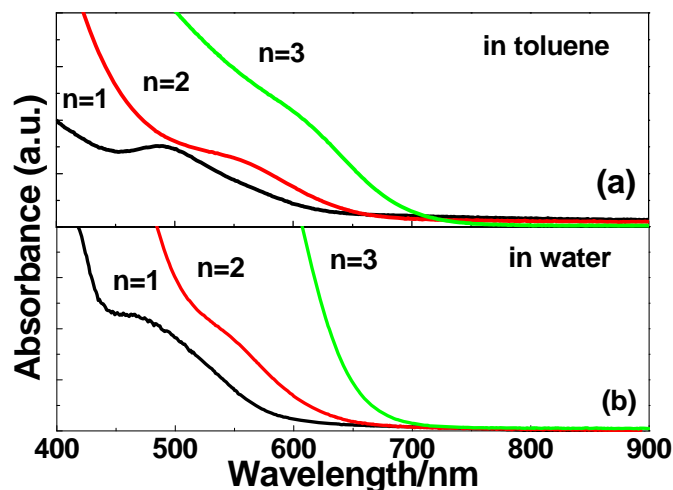
Figure 5.2 Absorption spectra of Zn-CIS quantum dots with various Cu/Zn ratios from n=1, n=2, and n=3 in (a) toluene and (b) water.

Figure 5.3(b) shows a high-resolution transmission electron micrograph (HRTEM) of a MPA-capped Zn-CIS QD isolated from a colloidal suspension. TEM images indicate that the QDs are single crystals with diameters ranging from 3 to 4 nm, i.e., 3.5 nm in average. Such MPA-capped Zn-CIS QDs could attach to the ZnO surfaces via carboxylate groups. A bright-field TEM image of a ZnO nanowire largely covered with an ensemble of Zn-CIS QDs was shown in Figure 5.3(c). The QDs are visible as the circular dark spots on the surface of the nanowire and EDX confirms the Zn-CIS composition. However, for a sample deposited with high concentration QDs, there will be a certain degree of aggregation during the QD deposition. In this condition, a size larger than 3.5 nm is possibly observed in Figure 5.3(c). The HRTEM image of the nanowire edge (Figure 5.3(d)) provides more compelling evidence that QDs are attached to the nanowire surface. An abrupt transition is observed between the (1010) lattice planes of the ZnO nanowire and the (112) lattice planes of the Zn-CIS QD, indicating an intimate contact between the QD and the nanowire within an approximate distance of 0.29 nm, or one ZnO (1010) lattice spacing.
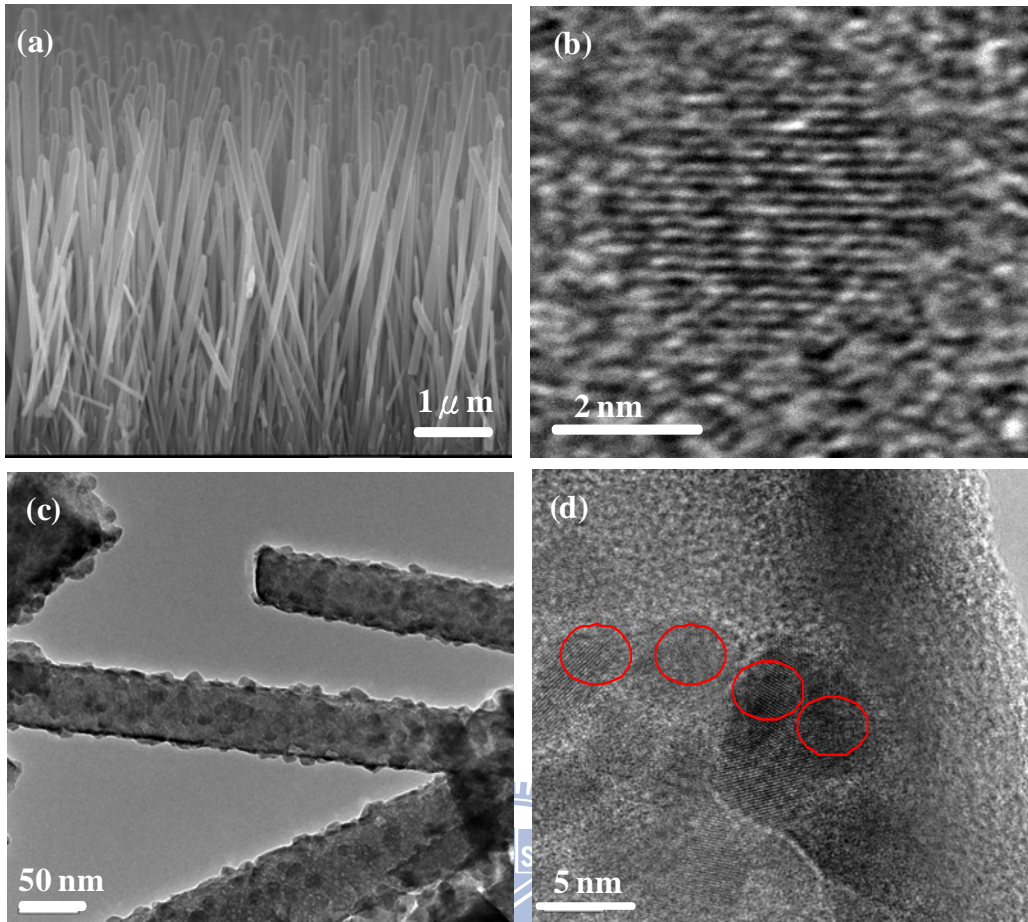
Figure 5.3 (a) Cross-sectional scanning electron micrograph of ZnO nanowires. (b) High-resolution transmission electron micrograph of a Zn-CIS quantum dot capped with MPA. (c) Bright-field transmission electron micrograph of a ZnO nanowire decorated with Zn-CIS quantum dots. (d) High-resolution transmission electron micrograph of Zn-CIS quantum dots attached to a ZnO nanowire. Some quantum dots have been outlined.

Figure 5.4(a) shows the appearance of three solutions with different ratios of Zn-CIS quantum dots dispersed in water, and then deposited to OTE/ZnO nanowires (Figure 5.4(b)), respectively. The photographs show the electrodes of different appearance of, yellow, red, and black, corresponding to the deposition of the Zn-CIS QDs of 3.5, 4.5, and 4.4 nm size, **[75]** respectively. However, since prolonged immersion in the Zn-CIS solution does not further enhance the absorption ability of the Zn-CIS, it was then assumed that the coverage of Zn-CIS nanoparticles on ZnO nanowire surface is spaciously saturated as a monolayer deposition. This can be

45

further verified by the fact that the QD surface was first organically modified by MPA, wherein the surface interaction between ZnO nanowire and Zn-CIS QD resulted from a chemical anchorage of the acidic group to ZnO nanowire and mercapto group to Zn-CIS QD. A multilayer deposition may be sterically inhibited as a result of repulsive interactions of MPA molecules between two approaching QD nanoparticles. The optical absorption properties of the Zn-CIS-coated ZnO nanowires are presented in Figure 5.4(c). It is evident that different-sized Zn-CIS particles exhibit excitonic transitions at 660, 570, and 530 nm. These excitonic peaks are similar to those observed for the QDs in the solution (Figure 5.2) and thus this confirms the binding of Zn-CIS QDs of varying sizes to the ZnO surface. Thus, the coloration of the ZnO nanowires offers an opportunity to selectively harvest the incident light. (The reflectance spectrum of an uncoated F-doped SnO_2 substrate was used as reference.)

5.3 Photovoltaic performance of the devices with various ratio of Zn dopant

Figure 5.5 shows the IV curves of the QD-DSSC devices integrated with those Zn-CIS-coated ZnO nanowires, which are assembled into a layer-type film. The relevant solar-cell parameters for the three samples are given in Table 5.1, which include the current density at short circuit (J_{SC} in mA cm^{-2}), the voltage at open circuit (V_{OC} in V), the fill factor (FF), and the efficiency of power conversion ($\eta = J_{SC} \cdot V_{OC} \cdot FF/P_{in}$ with $P_{in} = 100$ mW cm^{-2}).

A systematic trend with both V_{OC} decreasing upon increasing the n value (i.e., decreasing Zn doping) was disclosed. This result is similar to the work of Braunger et al, [120] who reported that the incorporation of small amounts of Zn led to an increased V_{OC}. However, the value of FF is lower than that received in TiO_2 DSSC solar cell (0.6-0.7), which is attributed to recombination between photoexcited carriers in the ZnO nanowires and tri-iodide ions in the electrolyte.
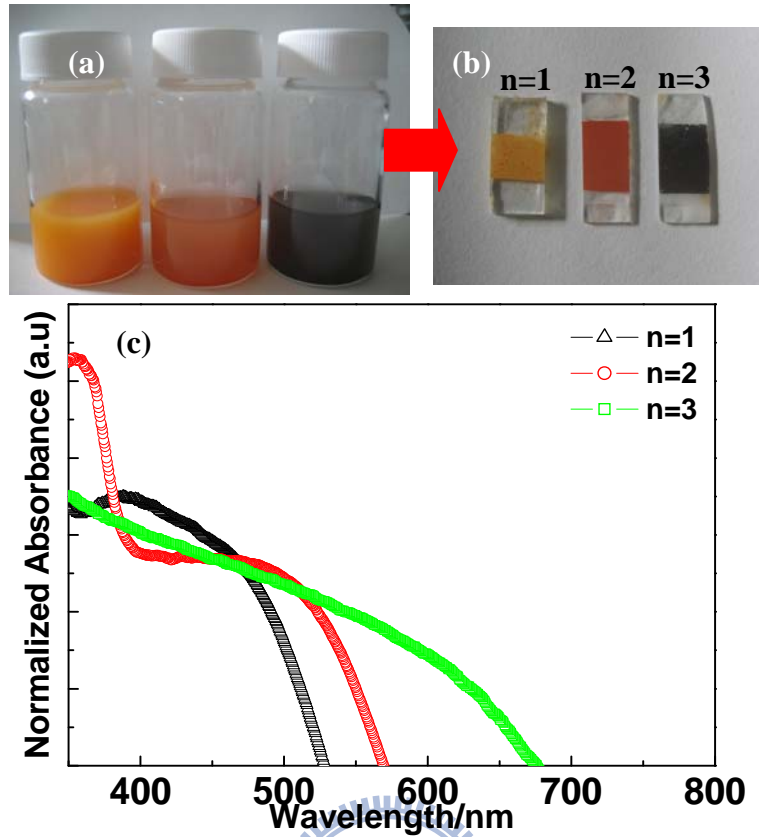
Figure 5.4 Photographs of different Cu/Zn ratio Zn-CIS quantum dots (a) in toluene, (b) anchored on ZnO NWs films. (c) Absorption spectra of different Cu/Zn ratios Zn-CIS quantum dots anchored on ZnO nanowires plate.

Because of the improvements in Jsc, and FF, the overall efficiency of conversion of photons to current exhibits a systematic increase from $\eta = 0.23$ % at $n = 1$ to $\eta = 0.28$ % at $n = 2$, but shows a decrease at $n = 3$ ($\eta = 0.24$ %). As can be seen, two important factors restrict the efficiency in the case of $n = 1$. The first limitation is the low FF, which indicates that electron transport in the ZnO nanowires has been obstructed. This obstruction can be attributed to two explanations: one is the presence of Zn^{2+}-ZCIS aggregates arisen from the unstable surface chemistry of ZnO nanowires electrode. During the assembly process, the acidic Zn-CIS QDs partially dissolve ZnO surface to form Zn^{2+}-ZCIS aggregates which deposited along the nano-pore walls in electrode and thus interfered the Zn-CIS QDs in generation of the photoelectrons. **[121]** The other one is the higher driving force for electron

injection. The conduction band edge of Zn-CIS with $n = 1$ is higher than others due to more amount of Zn doping. Therefore, a higher injection resistance exists at the ZnO/Zn-CIS interface and the photocurrent decreases more rapidly with the opposite potential applied, leading to a lower *FF*. Although the former situation exists in all three cases ($n = 1 \sim 3$), the later one is expected to dominate and explain the low *FF*. The second limitation to restrict the efficiency ($n = 1$) is the slightly lower *J*sc, which is attributed to insufficient photocurrent probably due to the lack of full spectrum of light absorption. However, it shows a slight reduction of the efficiency when $n = 3$, which is due to the decreasing Zn doping restricted open-circuit voltage and resulted in a low efficiency.
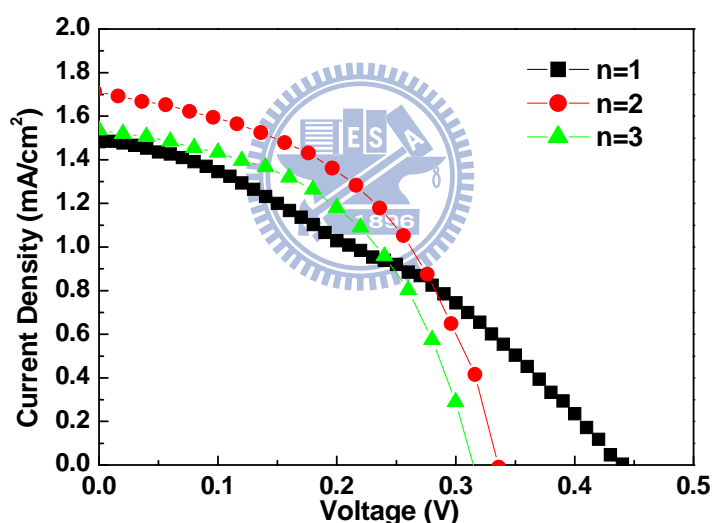
Figure 5.5 Current-voltage characteristics of Zn-CIS QDs-DSSC devices with different *n* value under stimulated AM 1.5 solar illumination (100 mW/cm^2) and active area 0.28 cm^2.

Comparing with the efficiency reported by Leschkies et al, **[109]** who obtained 0.4% power-conversion efficiency and short-circuit current 2.1 mA/cm^2 for a system of CdSe QDs with ZnO nanowires, the best power-conversion efficiency of current study has reached a lower value of 0.28%. However, while being normalized with those technical data in terms of the length of the ZnO nanowires, the average current

density is 0.342 mA/cm^2 per μm length, which is higher than that reported for the CdSe QDs with 12μm ZnO nanowires system having a value of 0.175 mA/cm^2 per μm length. Since it is reasonably to believe the population of the QD deposited on the nanowires will influence the resulting power-conversion efficiency, where the higher number of the QD on the nanowire surface, the higher the photocurrent can be produced while other variables are held constant, the average deposited number of the Zn-CIS QD on unit surface area of the ZnO nanowire is then estimated. In this case, the surface area of a 5 μm length single ZnO nanowire with 50 nm diameter is ca. 0.785 μm^2, which can accommodate about 45700 Zn-CIS quantum dots with 3.5 nm diameter for a hexagonal closed packing configuration, converting to the average adsorption number per μm^2 is about 58000. This is technically accessible since the microscopic observation readily showed a full coverage of the nanowire by the QDs. For the case of Reference 7d, the calculated surface area and average absorption number is 4.7 μm^2 and 68000 per μm^2 (12 μm length and 125 nm diameter of ZnO nanowire, 3 nm diameter of CdSe), respectively, which is higher by 10 times in surface area, but only larger by about 10% in QD population compared to the nanowires employed in current study. However, in practice, the population of QDs deposited on 12-μm ZnO nanowire is sparingly distributed, rather than closely packed, which probably explained the power-conversion efficiency for the latter system is not as high as expected but only slightly higher, by about 7.5%, than current experimental outcome. Such a comparison strongly indicates that the overall power conversion efficiency of the QD-DSSCs should be largely limited by (1) the surface area of the nanowires available for QD deposition and (2) the deposited population of the QD. The length and the size of the nanowire are unlikely to be major dominating factors for controlling the efficiency. This result proved our hypothesis regarding the average current density for the QDs-ZnO nanowires solar

cell system.

Table 5.1 Photovoltaic performance of the Zn-CIS/ZnO DSSCs under AM1.5 illumination (Power 100 mW/cm^2) and active area 0.28 cm^2.

	n=1	n=2	n=3
J_{SC} /mA cm^{-2}	1.48	1.71	1.54
V_{OC} /V	0.44	0.34	0.32
FF	0.36	0.48	0.50
η (%)	0.23	0.28	0.24

5.4 Design of the ZnS shell as a dual-function layer

Based on the results reported above, there are two major competing pathways that reduced the performance of the Zn-CIS-coated ZnO nanowire device when the electrons transfer toward the ZnO nanowire electrodes. First recombination dynamic is attributed to the complex reaction between excited electrons in Zn-CIS excited state and the I_3^- in electrolyte. Second recombination dynamic results from the capture of these excited electrons by Zn-CIS cations, resulting in the QD regeneration reaction and no longer competing efficiently with this reaction. These faster recombination dynamics, however, result in an enhanced dark current for these devices and consequently limit open-circuit voltage and fill factor of the device, as evidenced by the current/voltage data. As was known, partial QD corrosion from electrolyte and charge recombination between ZnO and Zn-CIS might be the major origin for the reduced efficiency. The source of charge recombination might have been due to the band discontinuity between ZnO and Zn-CIS. Given these considerations, a key strategy for optimization of the performance of Zn-CIS-based device is the minimization of interfacial charge recombination losses. To address this issue, a novel core-shell configuration with ZnS as a shell on the Zn-CIS QD (as core) was designed and the shell is acting as

both a protecting layer and a band-bridge layer.

Figure 5.6 shows *I-V* characteristics of two QD-DSSCs recorded during illumination with 100 mW/cm^2 simulated AM1.5 spectrum. One of these cells (hollow circle) was constructed using the core-shell QDs whilst the other without the ZnS shell (solid circle, sample with n=2) for comparison. The inset parameters are the *V*oc**, *J*sc, *FF*, and η of the ZnS-coated sample. It was found that both the power conversion efficiency (0.66%) and the short-circuit current (3.12 mA/cm^2) of the QD-DSSC modified by ZnS coating exhibited much higher values than those obtained without the coating. Noticeably, the efficiency was promoted more than 2 times after ZnS coating, which indicated that ZnS coating effectively enhanced the performance of the QD-based solar cell. The value of *Voc*, *Jsc* and *FF* were also increased after the ZnS coating, which suggests that the ZnS coating is able to effectively eliminate the excited electrons recombination. The influence of ZnS layer deposition for this QD-based solar will be elucidated in more detail in a later section.
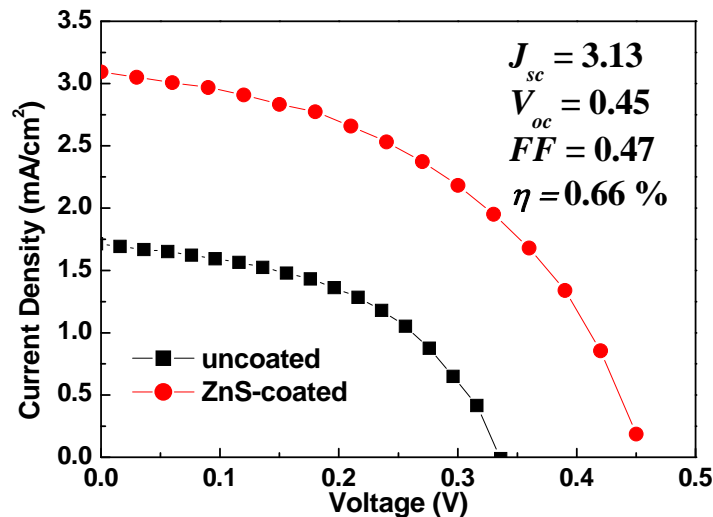
Figure 5.6 Current-voltage characteristics of Zn-CIS QDs-DSSC devices fabricated with (spot) ZnS coating and (square) without**.** Samples were measured under stimulated AM 1.5 solar illumination (100 mW/cm^2) and active area 0.28 cm^2.

Under open-circuit conditions, it is believed that electrons accumulate within the ZnS shell under visible irradiation, which shifts the apparent Fermi level to negative potentials. Once the illumination is removed, the accumulated electrons are slowly discharged because they are scavenged by the defects on the ZnO nanowire surface. On this basis, the electrons injected from the excited Zn-CIS should be survived in a longer time length and hence facilitate electron transport without undergoing any possible loss at grain boundaries.

To prove this assumption, we further employed picosecond emission decay measurement to analyze the excited electron lifetime, in order to gain better understanding on the recombination dynamics of excitons.

5.5 Mechanistic aspects of charge transfer into ZnO nanowires

On the basis of the principle of sensitizing large-band-gap semiconductors with short-band-gap semiconductors, efforts have been made to employ short-band-gap semiconductors as sensitizers to extend the photoresponse of ZnO into the visible region. The Zn-CIS particles exhibit a band-edge emission peak, which also shifts to the blue region with decreasing particle size. Figure 5.7(a) shows the emission spectra of $n2$ Zn-CIS QDs deposited on glass slide and ZnO NWs. These QDs exhibit characteristic emission peaks at 660 nm. When Zn-CIS was anchored onto a ZnO nanowire (Figure 5.7(b)), a significant quenching of the emission was seen, thus confirming the excited-state interaction between the two dissimilar semiconductor particles. This quenching behavior represents the deactivation of the excited Zn-CIS via electron transfer to ZnO nanowires. The processes that follow the band-gap excitation of Zn-CIS are presented in Equations (5.1)-(5.3):

$$Zn\text{-}CIS + h\nu \rightarrow Zn\text{-}CIS_{(e+h)} \rightarrow Zn\text{-}CIS + h\nu \qquad (5.1)$$

$$Zn\text{-}CIS_{(e)} + ZnO \rightarrow Zn\text{-}CIS + ZnO_{(e)} \qquad (5.2)$$

$$Zn\text{-}CIS_{(h)} + Redox \rightarrow Zn\text{-}CIS + O_x \qquad (5.3)$$
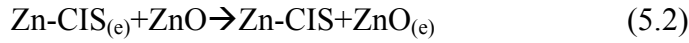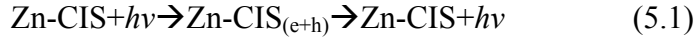
Whereas the electrons injected into ZnO are collected to generate photocurrent, it is necessary to employ a redox couple to scavenge the holes (Eq 5.3). Failure to scavenge holes could lead to surface oxidation, especially during extended period of irradiation. **[122-123]**
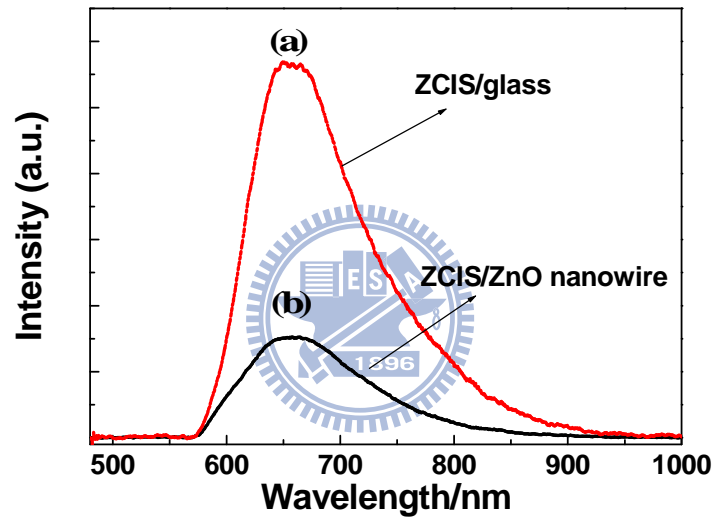
Figure 5.7 Emission spectra of 4.5 nm (*n* = 2) diameter Zn-CIS quantum dot film deposited on (a) glass and (b) ITO/ZnO NWs films. Excitation was at 410 nm. Spectra b carries a multiplication factor of 3. All of the spectra were recorded using front face geometry.

Time-dependent measurements of Zn-CIS on various plates were performed using time-correlated single-photon counting (TCSPC) with excitation at $\lambda_{ex} = 410$ nm. Typical results of a Zn-CIS/glass solution, a Zn-CIS/ZnO film, and a Zn-CIS@ZnS/ZnO film are shown in Figure 5.8. To investigate the effect of a rigid environment without interference from electron-transfer dynamics, deposition of Zn-CIS QDs on a glass plate was prepared. The phosphorescent decay of the

Zn-CIS/glass construct is describable with a multiexponential decay; three time coefficients obtained from regression analysis of the data fitting are listed in Table 5.2. When deposited on a glass slide, Zn-CIS particles exhibited emission decays with an average lifetime of 22.6 ns. We anchored Zn-CIS on ZnO films to test the effect of electron transfer through space from Zn-CIS to ZnO nanowires. The emission transient is quenched more rapidly than that of Zn-CIS/glass construct, Figure 5.8, having an average lifetime of 3.53 ns and some curve-fitted parameters are also given in Table 5.2. This result indicates that interfacial electron transfer through space quenches efficiently the phosphorescence in the nanosecond range. In the transient of a Zn-CIS/ZnO film, an additional 0.27 ns component appeared, and other nanosecond components were substantially quenched. If the shortening of the average lifetime is attributed to quenching by electron transfer from Zn-CIS QD to ZnO nanowire, the photocurrent density should be higher than the value above-mentioned. However, the efficiency is much lower than what is predicted, indicating electron transfer from Zn-CIS QD to ZnO nanowire is not the only relaxation path of exciton. According to the hypothesis, faster recombination from excitons trapped by redox or Zn-CIS cation caused an enhancement of dark current. After ZnS coating on the surface of Zn-CIS, the average lifetimes were lengthened from 3.53 to 7.7 ns due to the higher conduction band level of ZnS layer than that of Zn-CIS. The slower decay observed with ZnS coating provides as a strong indication that the electrons injected from excited Zn-CIS can survive longer and hence facilitate electron transport without undergoing possible losses at grain boundaries or trapped by redox species, rather than obstructed the electron transfer between Zn-CIS QD and ZnO nanowire. From Equation 5.4, the electron-transfer rate constants of Zn-CIS and Zn-CIS@ZnS core-shell QDs were evaluated, the results are listed in Table 5.2, indicating energy transfer of excited Zn-CIS QDs is multiple radiative exciton relaxation from the

54

energetically distributed surface-states ($k_{et} \leqq 10^9$ s^{-1} [124])

$$k_{et} = \frac{1}{\tau_{(ZCIS + ZnO)}} - \frac{1}{\tau_{(ZCIS)}}$$ (5.4)

This implies that the surface of the nanocrystals provides a significant source of defects or unpassivated sites where nonradiative recombination can take place. In contrast, ZnS coating appears to eliminate the competing recombination pathways and improves charge transfer efficiency from excited-state to ZnO nanowire.
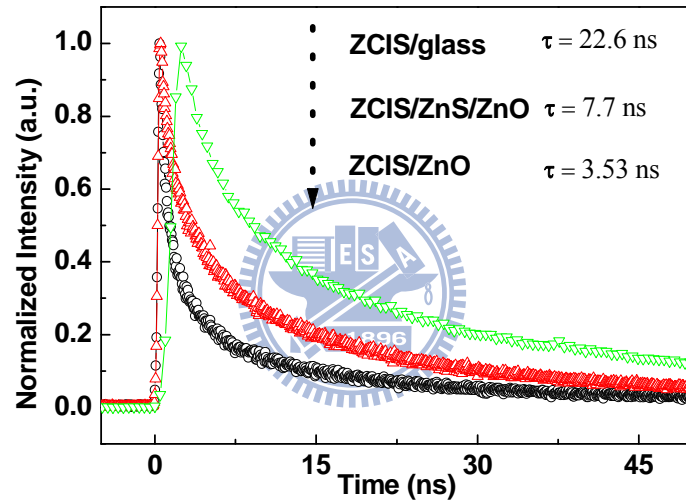
Figure 5.8 Fluorescent decay of 4.5 nm (n=2) diameter Zn-CIS quantum dots deposited on glass plate (top), ZnO nanowires flim (bottom). Middle is fluorescent decay of ZnS-coated Zn-CIS quantum dots deposited on ZnO nanowires film.

Table 5.2 Kinetic parameters of Zn-CIS emission decay analysis

	ZCIS/glass	ZCIS/ZnO	ZCIS/ZnS/ZnO
τ_1 (ns)	157 (5%)	46 (11%)	56.44 (6%)
τ_2 (ns)	5.5 (64%)	11.8 (4%)	14.62 (22%)
τ_3 (ns)	36.3 (31%)	2.25 (22%)	3.1 (39.4%)
τ_4 (ns)		0.274 (63%)	0.45 (32.6%)
$<\tau>$ (ns)	22.6	3.53	7.7
k_{et} 10^8 S^{-1}		2.39	0.86

5.6 Effect of ZnS shell thickness

To understand the effect of the layer thickness of ZnS shell on the resulting photo-conversion performance, Zn-CIS QDs with varying ZnS shell thickness were prepared and the corresponding power-conversion efficiency was examined. Figure 5.9 shows the efficiency of the core-shell (Zn-CIS)ZnS QDs-based devices with ZnS coverage of approximately 0, 0.6, 1.3, and 2.5 monolayers. The definition of a monolayer here is the shell of ZnS that measured 0.31 nm (the distance between consecutive planes along the [002] axis in bulk wurtzite ZnS) along the major axis of ZnS-coated QDs. As the coverage of ZnS on the Zn-CIS surface increases, a dramatic increase in efficiency was detected, followed by a steady decline at thickness above ~1.3 monolayers. Table 5.3 summarizes the relevant solar-cell parameters for these samples. It was found that the efficiency value increases from 0.28 to 0.71 with thickening of ZnS shell at 1.3 monolayers, which mainly resulted from an increasing Jsc (from 1.29 to 3.50 mA/cm^2). The enhancement of Jsc was attributed to the increased electrons (or excitons) transferred from Zn-CIS core to ZnO electrode through ZnS shell. Surface passivation by proper coverage of ZnS not only eliminated defects but also promoted the electrons transfer efficiently. However, once the coverage of ZnS is thicker than 1.3 monolayers, the Jsc value decreased considerably to 0.22 mA/cm^2 (reduced from 3.21 to 2.99 mA/cm^2) which resulted in a reduction of efficiency (0.085%). This phenomenon is due to the number of growing defects generated from the lattice mismatch between Zn-CIS and ZnS. These new defects could be the source of nonradiative recombination sites within the ZnS shell, which leads to the capture of electrons from Zn-CIS and decreases the Jsc dramatically.
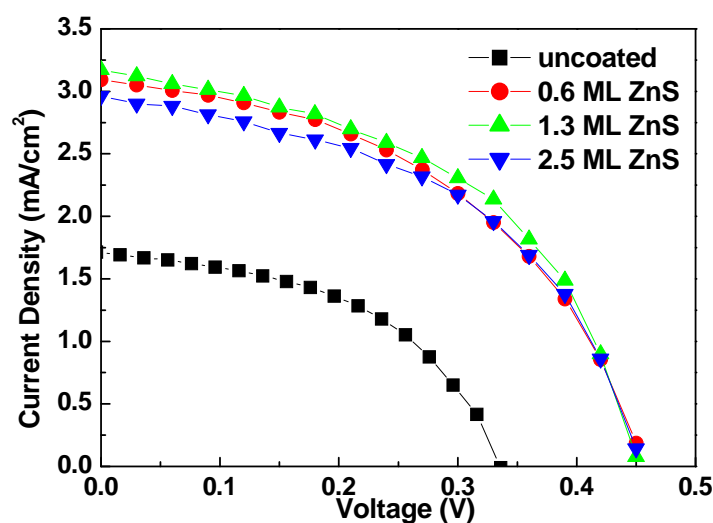
Figure 5.9 Current-voltage characteristics of Zn-CIS@ZnS-DSSC devices fabricated with different monolayer ZnS coating absorber under stimulated AM 1.5 solar illumination (100 mW/cm^2) and active area 0.28 cm^2.

Table 5.3 Photovoltaic performance of the Zn-CIS@ZnS/ZnODSSCs under AM1.5 illumination (Power 100 mW/cm^2) and active area 0.28 cm^2.

ZnS monolayer (ML)	ML=0	ML=0.6	ML=1.3	ML=2.5
J_{SC} /mA cm^{-2}	1.71	3.12	3.21	2.99
V_{OC} /V	0.34	0.45	0.45	0.45
FF	0.48	0.47	0.49	0.48
η (%)	0.28	0.66	0.71	0.65

To prove our hypothesis, HR-TEM was used to examine the internal structure of Zn-CIS@ZnS core-shell QDs. Figure 5.10 shows the HRTEM image of Zn-CIS quantum dots (a) without ZnS overcoating and (b) with 2.5 monolayers of ZnS overcoating. For the 2.5 monolayers sample, the outer lattice fringes are slightly askew compared with the inner part, which may be suggestive of strain-induced mismtach in the crystal. Figure 5.10(c) displays diffraction patterns of (a) bare Zn-CIS

nanoparticle and (b) that with <u>overcoating</u> 2.5 monolayers ZnS. A strong influence of the ZnS shell on the diffraction is revealed where the XRD pattern is dominated by the nanocrystals with the presence of 2.5 monolayers ZnS coverage compared with bare nanoparticle. The difference in the first broad diffraction peak between (a) and (b) spectra in Figure 5.10(c) suggests a possible change in orientation between the core and shell. Similar studies and analysis were reported for CdSe/ZnS core/shell structure. **[5, 85]** The increased Voc was due to a widened band-gap that was originated by the presence of the ZnS shell, which has been reported earlier using a PbS sensitized nanocrystalline. **[125]** Moreover, taking advantage of the energetic bands between the Zn-CIS core and ZnS shell, the higher conduction edge of ZnS than that of Zn-CIS QDs prevents the leakage of current from Zn-CIS to the electrolyte, causing more electrons to be injected into the ZnO nanowire and consequently increasing both Jsc and Voc.

The current solar cell device with 5 μm short ZnO nanowires has reached a power-conversion efficiency as high as 0.71 % through the use of a novel core-shell design. Upon normalizing those technical data in terms of the length of the ZnO nanowires, the average current density is 0.342 mA/cm^2 per μm length and increases to 0.642 mA/cm^2 per μm length after the coating, enhanced by as much as 1.88 times.. Furthermore, this finding strongly implies that an efficiency enhancement can be achievable if a maximal coverage and attachment of the Zn-CIS QDs on the ZnO nanowire can be achieved, and more than that, incorporation of the novel Zn-CIS@ZnS core-shell QDs further boosts the efficiency to a considerable extent which is highly expected for photovoltaic uses.

5.7 Concluding Remarks

The charge transfer from Zn-CIS or Zn-CIS/ZnS core/shell QDs into ZnO

nanowires by combining spectroscopic and photoelectrochemical techniques were investigated. The photoconversion efficiency of Zn-CIS QDs-based solar cells was readily tuned by controlling the Cu/Zn ratio. Increase in Zn doping increases the Voc of the Zn-CIS QD-anchored ZnO nanowires electrode device. Lower Cu/Zn ($n = 1$) ratio gives greater Voc and FF but insufficient absorption in the visible region. Higher Cu/Zn ratio ($n = 3$) showed better absorption in the visible region but caused sluggish electron injection into ZnO nanowires as effectively as that of lower-ratio Cu/Zn QDs. A maximum power-conversion efficiency (0.28%) with Cu/Zn ratio QDs of $n = 2$ was detected. However, a significantly improved power-conversion performance to as high as 0.71 % was attained while a thin ZnS shell of optimal thickness was deposited on these Zn-CIS QDs.
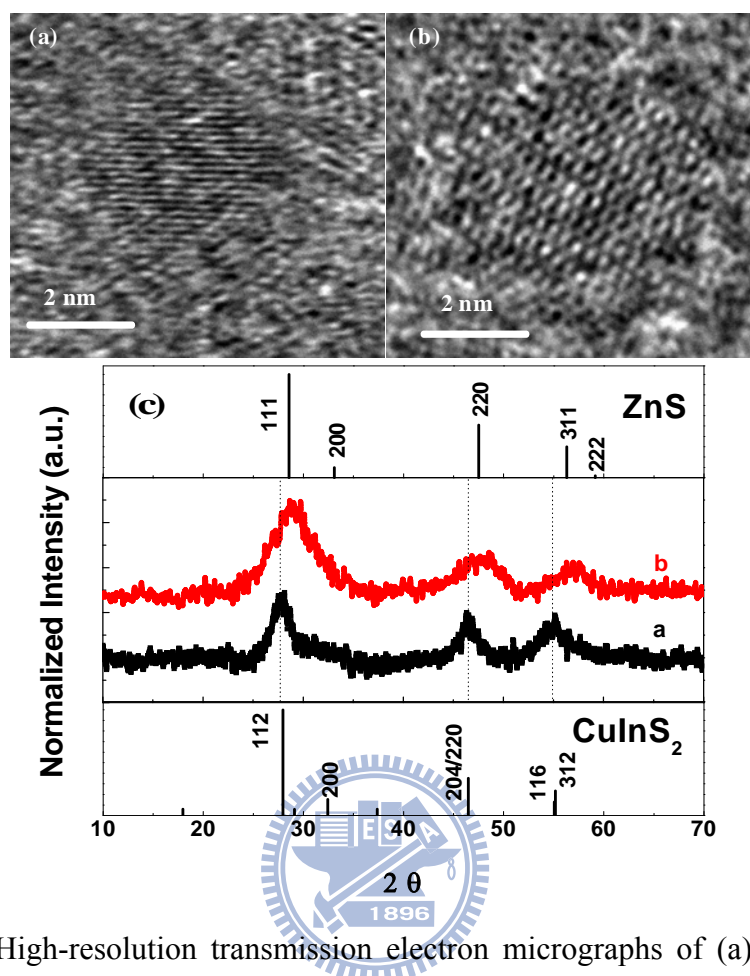
Figure 5.10 High-resolution transmission electron micrographs of (a) one "bare" Zn-CIS nanocrystallite and (b) one Zn-CIS nanocrystallite with a 2.5 monolayer ZnS shell. (c) Corresponding XRD patterns for (a) Zn-CIS nanocrystals and (b) ZnS-coated Zn-CIS. Two standard data for ZnS (top inset, vertical bars, JCPDS card No. 05-0566) and $CuInS_2$ (bottom inset, vertical bars, JCPDS card No. 75-0106) are shown for comparison.

Chapter 6

Magnetically-induced Synthesis of Highly-Crystalline Ternary Semiconductor Chalcopyrite Nanocrystals at Ambient Conditions

6.1 Introduction

In past decades, the synthesis of group II-VI semiconductors (i.e., binary semiconductor compounds) with various geometries has been successfully achieved for a number of different compositional combinations, from single phase elements to alloys and compound semiconductors. [127,128] In comparison, ternary alloys have been shown to offer more advantages over binary compounds, including continuously tunable band gaps and tailored physicochemical properties.

Colloidal semiconductors and metals have been synthesized using coordinating non-aqueous media by manipulating capping ligands, ligand-solvent pairs, reactant concentration, or synthesis temperature. [129-135] $CuInS_2$ (CIS), which is a ternary chalcopyrite compound, has demonstrated more optically and electronically tunable properties than the binary II-VI analogues with the cubic zinc blend structure. CIS has recently been considered to be a promising candidate for photovoltaic applications, owing to its relatively high absorption coefficient and excellent energy matching between its band gap (1.5 eV) and the solar spectrum. CIS nanocrystals have been synthesized by processes such as the elemental solvothermal technique, [68, 69, 136] thermolysis, [70,73] the hot injection technique, [137-138] and the single-source precursor route. [139-140] All of those techniques require high temperature and/or high pressure environments in order to bring the various kinds of species into the desirable crystal form. However, compared with the significant progress in monodisperse binary chalcopyrite colloids, investigation of ternary chalcopyrite colloids has been limited, owing to the lack of suitable synthesis methods. Therefore,

the challenge remains in the preparation of monodisperse ternary chalcopyrite colloids with manageable size and shape.

Making ternary chalcopyrite compounds with superparamagnetic behavior by magnetic doping has not yet been tried. It is generally understood that incorporation of magnetic elements might enable the host materials to exhibit magnetic behavior. [141-144] By limiting the size of the resulting doped compound to a few nanometers in scale, superparamagnetic character may be developed. Room-temperature ferromagnetism has been reported for non-magnetic metallic (Pd and Au) nanoparticles and carbon nanostructures (nanographites and polymerized fullerenes). [145-149] The ternary chalcopyrite semiconductors expressed as I–III–VI2, are considered to be a superstructure of the zinc-blende type. In particular, CuAB2 (A=Al, Ga, In; B=S, Se) has shown intrinsic p-type conductivity, which suggests that chalcopyrite compounds might be interesting host materials for magnetic doping. CIS nanocrystals have been found to exhibit magnetic properties in a limited number of reports. [150-151] Taking these findings into consideration, we hypothesized that a new synthesis technology could be advanced by magnetic doping, in which CIS nanocrystal nucleation and growth could be self-manipulated via magnetically induced heating of the developing CIS nanocrystals upon synthesis. This is in contrast to the currently existing time-consuming, cost-ineffective, and eco-unfriendly autoclaving synthesis.

Here, we report a novel methodology in the synthesis of CIS nanocrystals in coordinating solvents without sequential chalcogenide precursor injection, which is achieved by incorporation of magnetic Zn species, i.e., diethyldithiocarbamide zinc (DECZn), following a high frequency magnetic field induction (HFMF) (Figure 6.1) at ambient condition. The process for growing the resulting Zn-doped CIS nanocrystals with definite geometrical evolution can then be developed and

62

controlled.
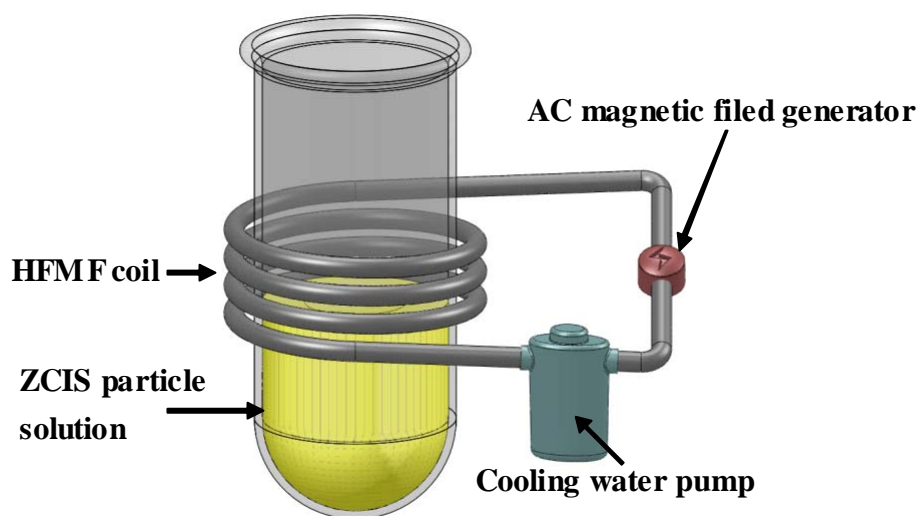
Figure 6.1 Apparatus setup for the magnetically-induced synthesis.

6.2 Optical behavior

A solution mixture of copper chloride (CuCl) and indium chloride (InCl₃) precursors was first prepared by dissolving in oleylamine and diluted with octadecene, followed by a trioctylphosphine (TOP) capping agent. Judicious choice of the precursor ratio results in nanocrystals with a tunable [Zn]/[Cu] composition. The mixed solution was subjected to HFMF for crystal growth. The size and shape of the resulting nanoparticles could be finely tuned by varying the exposure time and concentration of the capping agent during the synthesis. Under 90 W AC magnetic induction, the appearance of the solution underwent a sharp change in color from yellow to red, over a time period of 45 seconds, and then turned to black after two minutes of induction. However, without the addition of Zn precursor, the solution mixture showed no any change in appearance even for a long duration of magnetic induction. To investigate the effect of magnetic induction, aliquots of the Zn-doped solutions with different time durations from 30 to 360 seconds were taken and

examined by ultraviolet-visible spectroscopy, photoluminescence spectroscopy, and transmission electron microscopy. The fluorescent Zn doped $CuInS_2$ nanocrystals started to appear in the solution within the first 60 seconds and while under 365 nm UV light exposure, the solutions showed a yellow (30 sec) and red (45 sec) appearance (Figure 6.2). These two samples with emission peaks at 590 and 630 nm were similar to those reported by Nakamura et al, [75] who observed an improved PL intensity when Zn was incorporated into CIS nanocrystals, due to a reduction of anti-site defects. [76] The UV-vis spectra of these samples (30, 45, 120, 300, and 420 seconds, respectively) show the typical absorption curve of a semiconductor material (Figure. 6.3): a band-edge peak was visible at around 390 and 800 nm. The absorption energies for a 120 second exposure were significantly shifted to that of bulk $CuInS_2$ (ca. 810 nm), consistent with the expected effects of quantum confinement. More evidence for the size confinement effect was provided by PL spectroscopy (Figure 6.2). The PL spectrum of the Zn-CIS colloids showed a blue-shift compared to those in bulk CIS, which suggests further the size-dependent optical properties of the colloids. However, after long-term magnetic exposure, the absorption spectrum shifts to a longer wavelength, and a broad shoulder develops at 800 nm. The shift of the absorption spectrum to a longer wavelength with increasing photolysis time is consistent with band gap narrowing due to particle growth. The absorbance range broadens from 390 to 800 nm (corresponding to particle size from 3.5 to 75.4 nm), indicating the band-gap of the Zn-CIS nanocrystals underwent a red shift to match the bulk CIS (1.5 eV, 810 nm).
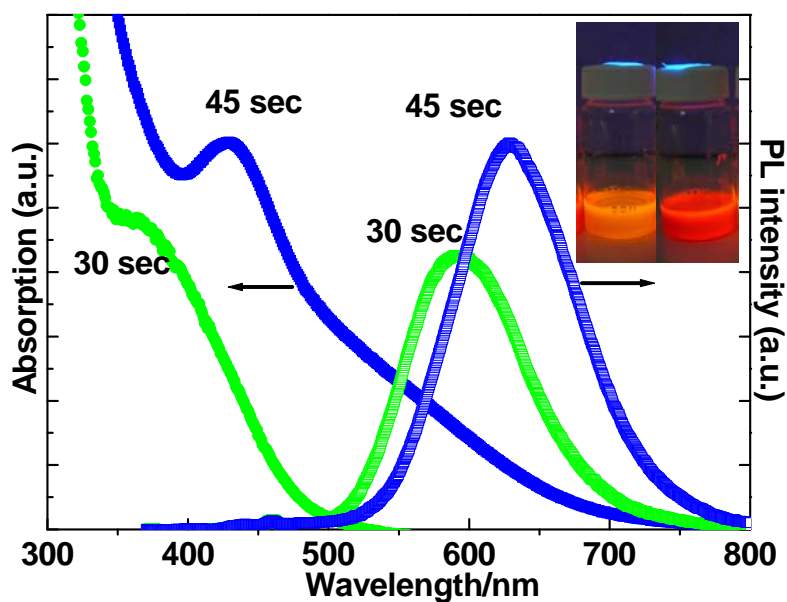
Figure 6.2 Absorption (left) and photoluminescence (right) spectra of ZCIS colloids obtained by HFMF in 30 and 45 seconds. Inset shows the visual image of these two ZCIS colloids under a 365 nm UV lamp irradiation.
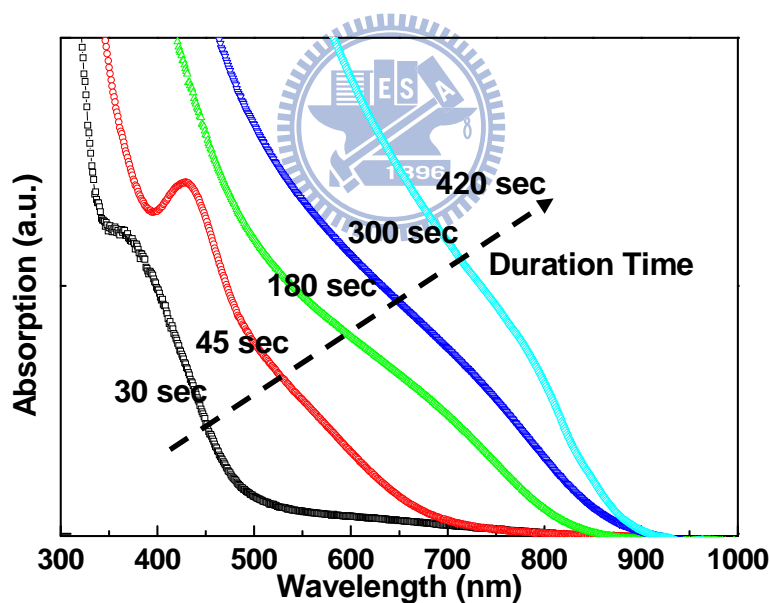
Figure 6.3 UV-vis absorption spectra of Zn-CIS nanocrystals under magnetic exposure (from left to right: 30, 45, 180, 300, and 420 sec.).

6.3 Growth of Zn-CIS nanocrystals

The TEM image of these Zn-doped nanocrystals showed narrowly size-distributed nanoparticles, with an average diameter of 3.5 nm (Figure 6.5(a)). The high-resolution TEM image (Figure 6.4(a)) further indicated that these nanoparticles

were single crystalline and spherical in shape. The size-specific quantum confinement of this size of the Zn-CIS nanocrystals gave a red-color solution. However, after only two minutes of magnetic field exposure, these nanocrystals grew to a size larger than the Wannier-Mott bulk exciton radius (i.e., 4.1 nm for CIS [84]). To identify the crystal growth of the Zn doped chalcopyrite semiconductor under magnetic exposure, solution samples were taken after magnetic induction for durations of 180, 300, and 420 seconds, where, a steady-state development of the resulting nanocrystals is assumed, albeit unintentionally selected. For the 180 second duration, the colloidal Zn-CIS nanocrystals displayed a rectangular geometry, with a size of 12-15 nm in length (Figure 6.4(b)). In the TEM images, lattice fringes corresponding to {0-11} and {220} CIS planes were predominantly visible. Based on these observations, the structure of the Zn-CIS nanocrystals after 180 seconds of magnetic induction was confirmed to be trigonal-pyramidal, rather than trigonal-plate, and has been formulated for $CuInSe_2$ [152] and CdS. [153] After 300 seconds of induction, a nanocubic geometry was obtained (from the same batch of solution), as shown in Figure 6.4(c). The lattice fringes are separated by a distance of 3.1 Å, which corresponds to the {112} planes of CIS. The surface tension values of the {100}, {010}, and {001} planes of nanocubes are very similar, resulting in a similar distance between these three crystallographic faces and the Wulff`s point. On this basis, a higher average growth rate along those crystallographic directions is expected, resulting in Zn-CIS nanocrystals evolved into rectangular or quasi-cubic geometry. Nevertheless, after 420 seconds of magnetic induction, the {112} plane of the nanocube showed the fastest growth rate to form a bar-like geometry with an average length of 75.4 nm and width of 18.3 nm (Figure 6.4(d)).
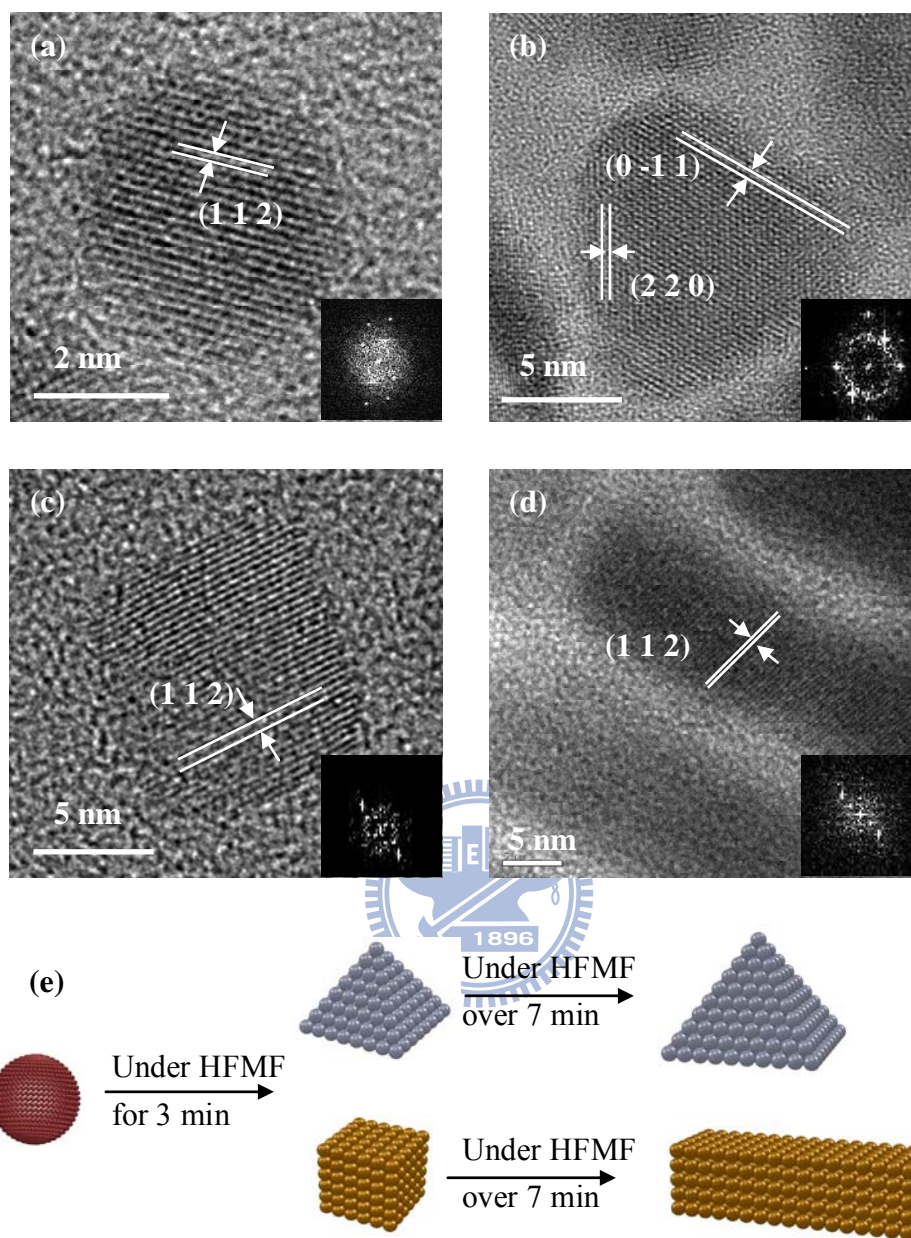
Figure 6.4 HRTEM images of the Zn-CIS nanocrystals with various geometries; (a) nanoparticle, (b) nanopyramid, (c) nanocube, (d) nanobar synthesized under magnetic exposure. (e) Schematic of the growth of nanoparticles into various geometries of different size, from nanopyramids, nanocubes, and nanobars under magnetic induction.

Lower-magnification TEM investigations were performed to monitor the formation of Zn-CIS nanocrystals. As shown in Figure 6.5(a), spherical particles dominantly appeared in the solution in the 60-second sample. After 180 sec, most of

the spherical structures were replaced by nanopyramids with diameters of 12-15 nm, as shown in Figure 6.5(b), indicating that the nanoparticles were transformed in the magnetic field. The nanocubes (Figure 6.5(c)) were formed after 300 sec and then eventually grew into nanobars after 420 sec, Fig. 6.5(d).
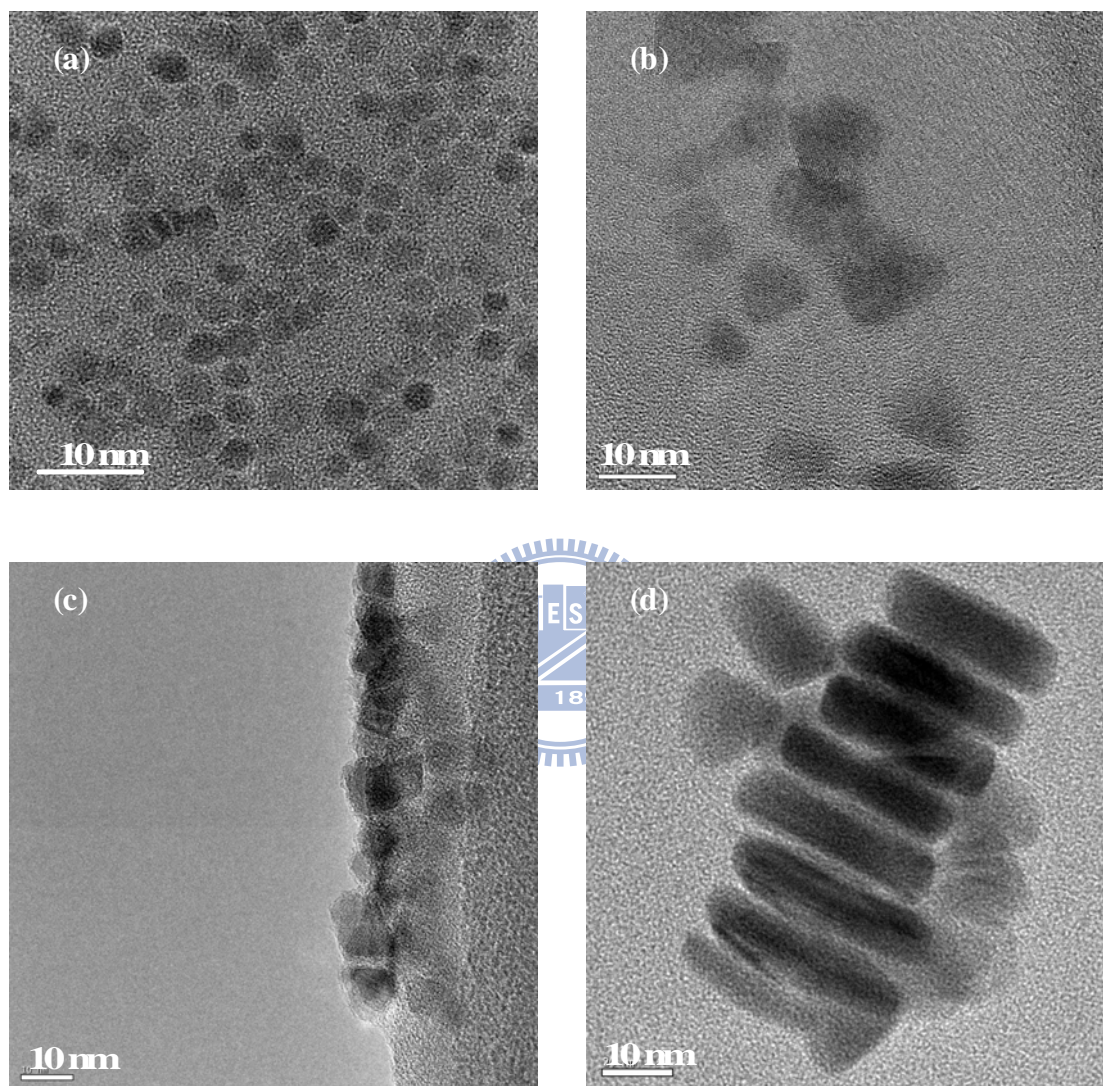
Figure 6.5 TEM images of samples (a) nanoparticles, (b) nanopyramids, (c) nanocubes, (d) nanobars. (All the images have the same scale bars (10 nm).)

It appears from experimental observations that both the pyramidal and cubic Zn-CIS nanoparticles co-existed in the time duration of 300-420 seconds (Figure 6.6). The nanocubes kept growing along the (112) plane and turned into a nanorod geometry; in the meantime, the small pyramidal nanoparticles kept growing equally

along the four faces and turned into large crystals of identical geometry (see Figure 6.4(e) for a better illustration). In other words, both the nanorod and nanopyramid Zn-CIS crystals of larger dimensions, after a longer magnetic exposure, were presented simultaneously in the final suspension. However, it is not fully understood whether there has any interactions evolved between the growth of both types of the nanocrystals.

In a chalcopyrite $CuInS_2$ crystal, the bonding energy between Cu and S atoms is weaker than that between In and S atoms, which means that the Cu vacancy is preferably generated. In addition, the Cu vacancies induce anti-site defect generation. [76] Furthermore, the ionic diameter of Cu (0.635 A) is similar to that of Zn (0.64 A). On this basis, the Cu site in the lattice is preferentially substituted by Zn where such a substitution is found to be more energetically favorable to prevent anti-site defects. [38] The molar ratio of Zn:Cu:In:S in the nanocrystals of varying stages of magnetic induction was determined by inductively couple plasma (ICP) spectroscopy and TEM-EDX analysis (Figure 6.6), both data showed consistent ratio with an average of 1.1:2.5:3.4:5.6, i.e., a Cu-rich phase, for various geometrical structures, as given in Table 6.1. These results indicated that a relatively uniform compositional evolution of these Zn-CIS nanocrystals can be achieved.

Table 6.1 Composition of the varied structure Zn-CIS nanocrystal

	Zn%	Cu%	In%	S%	Ratio
Nanoparticle	8.73	19.84	26.98	44.44	1.1:2.5:3.4:5.6
Pyramid	8.46	19.6	28.07	43.87	1.1:2.5:3.6:5.7
Cube	9.01	19.67	27.45	44.87	1.1:2.4:3.4:5.5
Bar	9.34	19.42	27.75	43.49	1.2:2.5:3.6:5.6
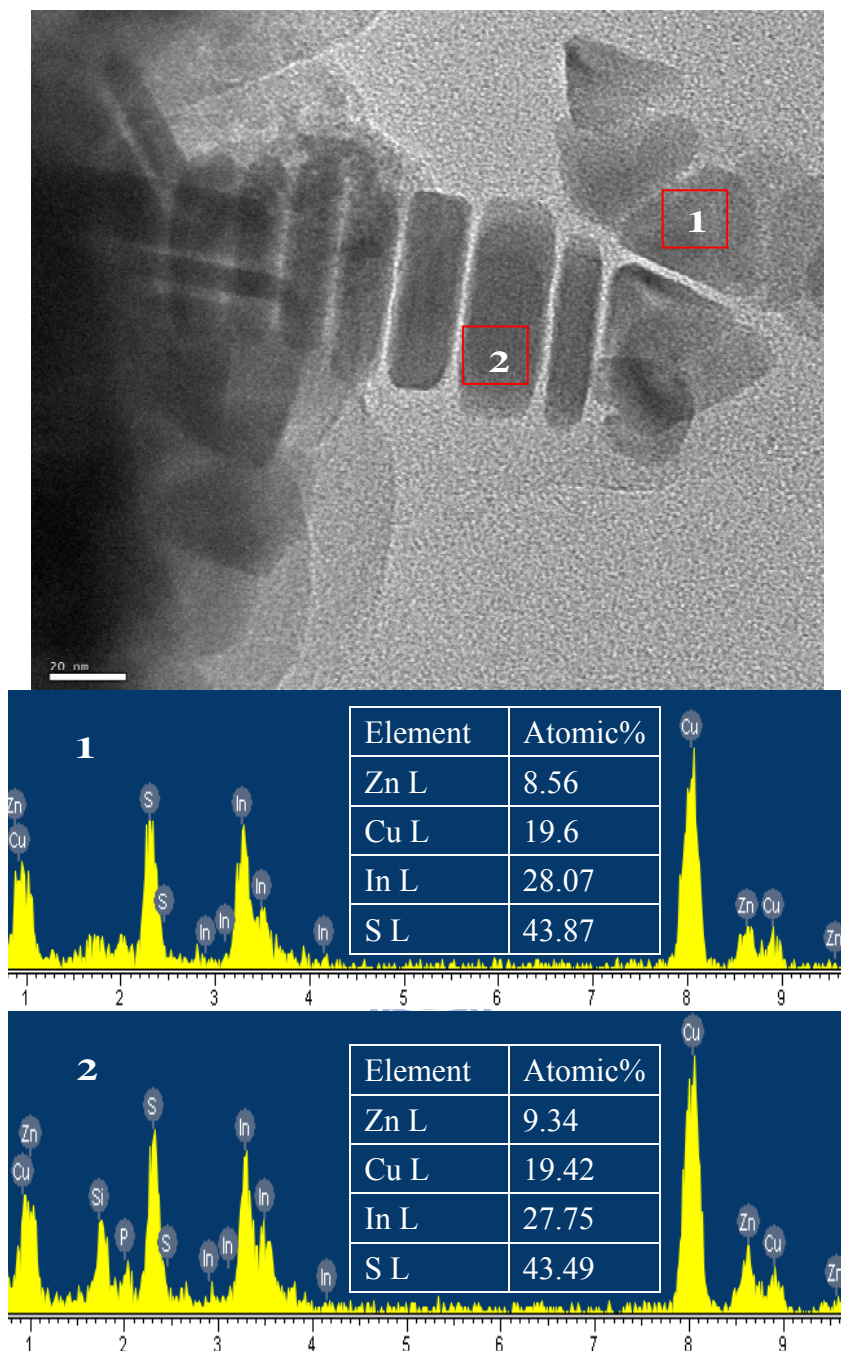
Figure 6.6 Energy dispersive X-ray spectra (EDX) and corresponding TEM images of nanobar shaped ZCIS nanocrystals. EDX analysis evidences components of ZCIS nanocrystals. Larger pyramidal shape of ZCIS crystals also found under long-term HFMF exposure, which indicated small pyramidal crystals kept growing along three directions and eventually coexisted with nanorod crystals.

6.4 Crystallographic analysis

The crystal phase of the as-synthesized compound was identified by powder

X-ray diffraction (XRD) (Figure 6.7, black lines on the *X*-axis, respectively, denote CuInZnS$_2$ diffraction patterns, JCPDS NO. 47-1731) and higher energy XRD (Figure 6.8), which clearly reveals that all the diffraction peaks perfectly match the crystallographic structure of chalcopyrite CuInZnS$_2$ (space group: *I42d* (No.122) and unit cell dimensions : *a* = *b* = 5.508 A, *c* = 11.09 A), with no other impure phases detected, indicating that a phase-pure Zn doped CIS can be efficiently obtained. Moreover, regardless of the particle size (ranging from 3.5 to 75.4 nm) of the synthesized Zn-CIS nanocrystals, they all gave an identical diffraction pattern. These results, together with the HR-TEM observations, further prove that all the Zn-CIS nanocrystals synthesized under magnetic induction possess single-crystal structure with a relatively high degree of uniformity. Although the variation of crystal shape has been addressed in a number of articles, the details of the mechanism have not yet been clarified. **[154-156]** It is generally believed that the shape evolution of the nanocrystals is dominated by the inherent crystal structure during the initial nucleation stage. The subsequent growth was then managed through the delicate control of external factors, such as surfactants, temperature, and time. **[157]**
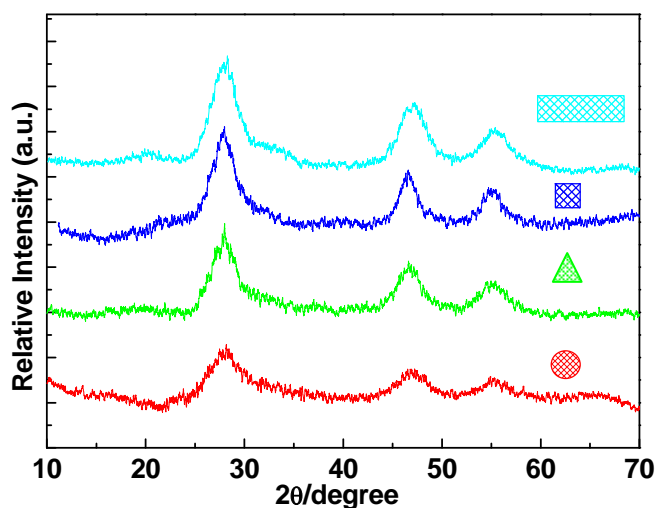
Figure 6.7 XRD patterns of the Zn-CIS nanocrystals of different shapes, with bottomlines on the x-axis, denoting standard CIS powder diffraction pattern.
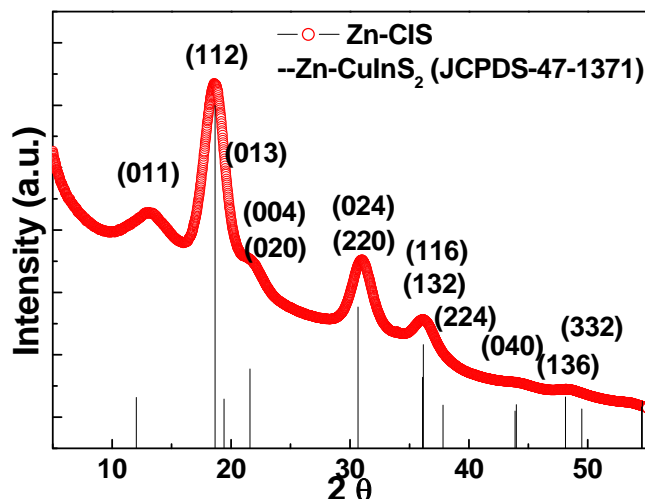
Figure 6.8 XRD spectrum of Zn-CIS nanobar by using higher-energy XRD, bottom inset is the chalcopyrite structure $CuInS_2$ for comparison.

6.5 Discussion

The discovery of magnetic-induced synthesis of a ternary semiconductor is far beyond what has been observed to date using traditional solution chemistry, such as the solvothermal method, where temperatures as high as 200-300° C over time periods of several to dozens of hours are frequently required. The magnetic-induced crystal growth of Zn-doped CIS in this investigation should cause a self-heating effect originating from the developing Zn-CIS compound, since the CIS nanocrystals showed a stronger paramagnetic behavior after doping with Zn, Figure 6.9. The hysteresis loop for the resulting Zn-CIS nanocrystals was corrected for the diamagnetic contribution (inset of Figure 6.9) and shows typical paramagnetic behavior, with the magnetization essentially saturated above 10 kOe. The hysteresis loop data for the Zn-CIS nanocrystals at 300k and 5k (Figure 6.10) also evidenced the superparamagnetism of such Zn doped CIS nanocrystals. In theory, magnetic colloids in a magnetic field experience an internal stress as a result of the non-uniform distortion arising from magnetic forces, generating heat. Under magnetic induction,

the temperature of the Zn-CIS colloidal solution gradually rose from the very beginning and reached a steady-state temperature of several tens of Celsius, at which point the heat generation from the magnetic Zn-CIS nanocrystals was equilibrated with the heat dissipated to the environment.
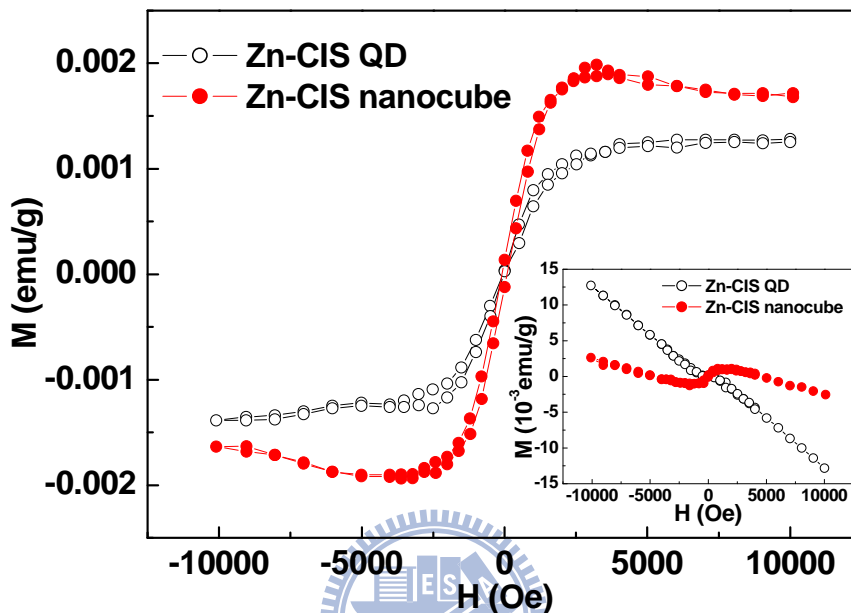
Figure 6.9 Magnetization curves measured at room temperature for Zn-CIS QDs (hollow) and Zn-CIS nanocubes (solid). The inset shows the raw data and the data after subtracting the high-field diamagnetic component.
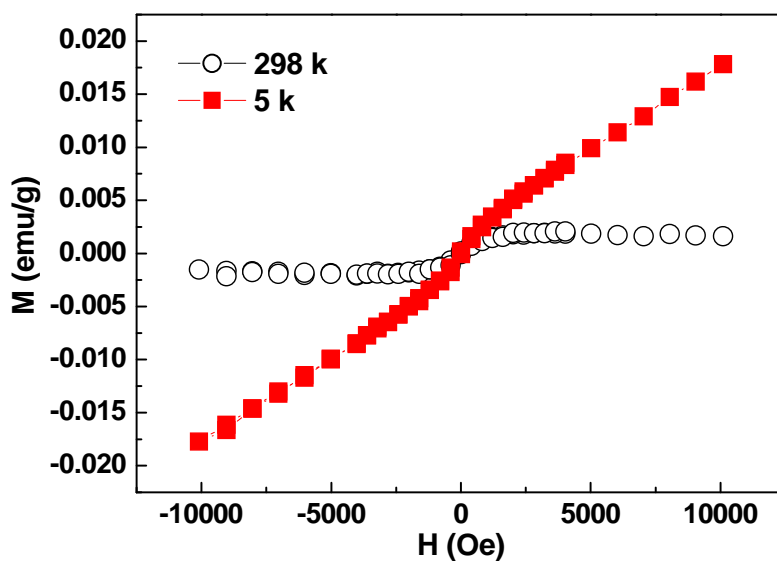
Figure 6.10 Magnetization curves measured at different temperature for Zn-CIS QDs.

Assuming magnetic heating involves only isolated, independent nanoparticles, RF field friction in and around a magnetic particle can be stemming from two sources: [158] first, the particle may tumble causing frictional heating at the particle-solvent interface. The relaxation time for this mode can be estimated as the time required for Brownian motion over a characteristic distance of the order of one particle diameter. Brownian relaxation may not be responsible for the frictional heating of the Zn-CIS, however, because the heat generated from this mechanism should be equally shared between the nanoparticle and solvent so it is unlikely for the Zn-CIS alone to reach a very high temperature. Friction may also arise from spin rotation without crystal lattice rotation within the crystal. The relaxation time for this mode (Neel relaxation) is the reciprocal of the spin flipping rate, too fast to contribute any significant friction in a RF field. As a first approximation, we can roughly approximate the heating rate R_{ZCIS} of the Zn-CIS (or ZCIS) nanoparticles in terms of R_S using $V_{ZCIS}R_{ZCIS}C_{ZCIS}=$ $(1-V_{ZCIS})R_S C_S$. Here V_{ZCIS} is the volume fraction of the Zn-CIS nanocrystals relative to the solution, and C_S and C_{ZCIS} are the volumetric specific heat of the solvent and ZCIS, respectively. Here we used V_{ZCIS}~0.01, meanwhile, referring to the specific heat of ZCIS and the solvent, we estimate C_S/C_{ZCIS} ~1. Therefore, the calculated R_{ZCIS} is from 10° C/s to 100° C/s, i.e., it takes a few to few tens of seconds for the temperature to rise to several hundred degrees of Celsius in the Zn-CIS nanocrystals before a steady state is reached. However, interfacial heat transfer at a nanometer scale surrounding the nanocrystals is not well determined.

Referring back to the forming of such Zn-CIS nanocrystals under magnetic field, how do these particles form in the first place? In the solution without adding Zn precursor (which is virtually a Zn-S-containing precursor), the other two precursors (i.e., Cu and In) are unable to react in the presence of magnetic field (we have also found no any reaction with Zn-S-containing precursor alone). However, after the

Zn-S-containing precursor was prepared separately, i.e., completely dissolved in a solvent, we found no any precipitate in the solution and believed it may form a Zn-S-containing compound. While the first aliquot amount of the compound was added to the mixture solution, energetically effective collisions (under heating and agitating) among those precursors should cause the incorporation of Cu ion with the compound (due to the similar ionic size between Cu and Zn ions), upon which a chemically equivalent mixture of the those molecular precursors may develop into the first nanocrystal or "first compound" in the presence of magnetic field, such as Cu-containing ZnS compound, which allows to induce heating under exposure of the field. Since the electron configuration of Cu^+ is d^{10}, ZnS doped with Cu^+ would be diamagnetic. If copper existed as Cu^0 or Cu^{2+} in the ZnS, the system would be strongly paramagnetic. [159] In our study, the Cu precursor is CuCl, which means Cu^+ could be pseudo-oxidized by the Zn-S-containing compound (i.e., S^- in the Zn precursor, Figure 6.11).
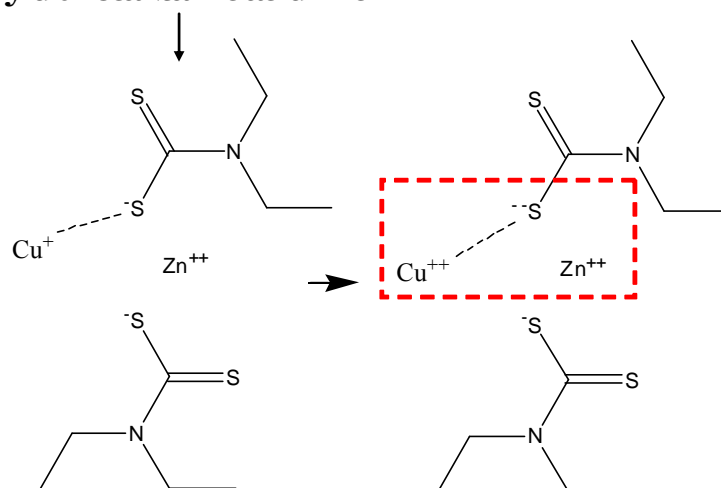
Figure 6.11 Mechanism of "first paramagnetic nanocrystal" formation.

While the Cu-containing ZnS compound exhibits paramagnetism, the magnetic

field can thus induce heat. To prove our hypothesis for the formation of a chemical compound, we mixed only Cu precursor into the solution of Zn-S-containing precursor, in the absence of In precursor. A secondary force may bring interaction between Cu and S ions, rather than forming any chemical bond, leading to a featureless of Cu-S bond using Raman spectroscopic analysis, in other words, there appears no chemical interaction between Cu and S in the mixture. In spite of such weak attraction, the reaction is somehow an ongoing procedure in the presence of magnetic field which was confirmed by a visual observation of the solution, turning from turbid appearance to transparent. This phenomenon indicated the precursors in the solution were actually affected by the magnetic field and consequently induced heating for further reaction. Although we have no direct evidence available for such an intermediate compound presently, the SQUID analysis of collected precipitation from the mixed Zn-S and Cu precursors demonstrated our hypothesis (see Figure 6.12). It is highly likely to believe that the "first" magnetic nanocrystal may preserve for a short period of time and form rapidly into a more stable nanocrystal with Zn-Cu-In-S near-stoichiometric chemistry under the presence of magnetic field due to the involvement of other ions, such as In. Once the first paramagnetic Zn-CIS nanocrystal was developed, a continuous growth was followed immediately and rapidly. Development of such a "first paramagnetic nanocrystal" in the solution should be time dependent, following a crystal growth kinetic, both scenarios result in a mixture of the nanocrystals of varying geometry and size over a certain time span of reaction, as evidenced in Figure 6.4, where the nanocrystals with different size and shape can be observed simultaneously.
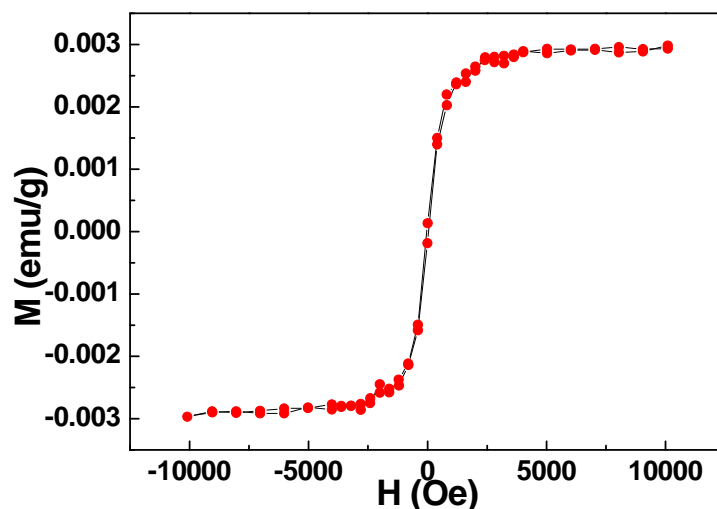
Figure 6.12 Magnetization curve of precipitation from Zn and Cu precursors.

Accordingly, the formation of Zn-CIS nanocrystals arising from magnetic induction is associated with fast nucleation and growth kinetics. In other words, once the nuclei begin evolving, a rapid temperature rise in the Zn-CIS nuclei should promote fast atomic deposition from the surrounding precursor bath. The exchange of heat and mass between the growing hot nanocrystals and the surrounding cold solvent due to convection should accelerate the atomic deposition of the precursors. One important feature of this synthesis is that the hot nanocrystals are likely to impart energy to the impacting precursor molecules which carry an organic part, where a further thermal dissociation of the organic compartment at the points of deposition or collision should take place upon numerous collisions between the precursor molecules and growing nanocrystals. This results in a chemically-pure deposition, leaving behind the organic counterparts in the solvent medium, as is further evidenced in the HR-TEM photos, (Figure 6.4), where highly orderly-arranged texture of the Zn-CIS lattice for the nanocrystals from smallest to largest dimensions can be resolved at various time periods of synthesis. This result is not possible for solvothermal or similar techniques, except at relatively high temperatures, e.g., $>200^{\circ}$ C, for a long

synthesis duration, e.g., >10 hours, where the resulting ternary nanocrystals showed very poor crystallinity (Figure 6.13) and poor optical behaviors. Incorporation of organic molecules into the developing semiconductor nanocrystals may be one critical factor deteriorating the desired properties.
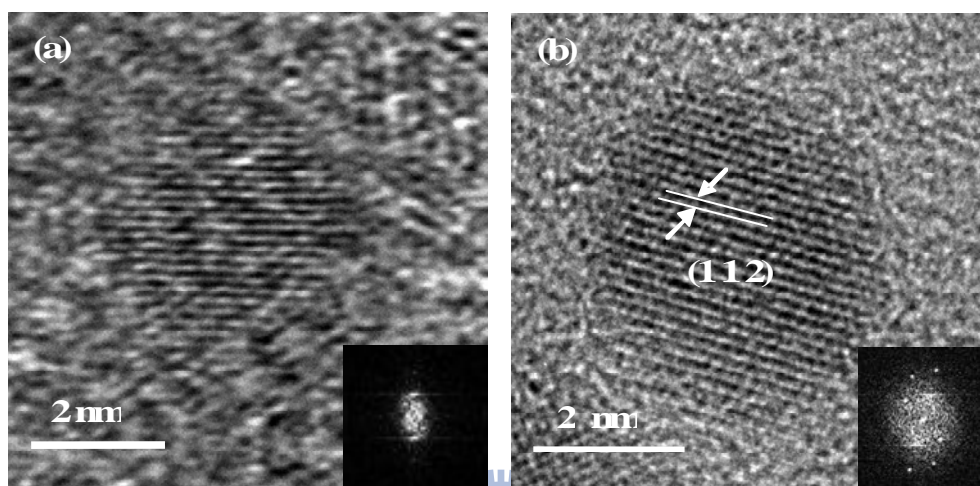
Figure 6.13 HR-TEM images of ZCIS nanocrystals synthesized through high-temperature organic solvent method (a) and HFMF (b). This comparison indicated that crystallinity of ZCIS nanoparticles was enhanced by HFMF.

It is also surprisingly to learn that a highly uniformly compositional development of the nanocrystals of various geometries can be achieved, which suggests that the co-deposition of all those molecular precursors over the time span of the synthesis is kinetically similar. In other words, once the nanocrystals were initially evolved, the potential of those precursors upon impingement to the growing nanocrystals should be energetically similar. Such a collision should be a matter of an interaction between the precursor and nanocrystals, as a result of interparticle attraction. This is further evidenced with a subsequent zeta potential measurement (supporting information Table 6.2) of the nanocrystals. The zeta potential value of Zn-CIS nanocrystals was slightly negatively charged in an average value of -10.8 $\pm$ 3.2 mV for various

geometrical structures. These slightly negatively charged nanocrystals should exert weak attraction to the precursors, following a kinetically similar impingement to form final Zn-CIS crystals. However, the Cu-rich phase evolution of the nanocrystals suggests when incorporated into the lattice, the Cu precursor tends to form a lowest-energy solid solution compared to **t**hose with Zn precursor. Furthermore, the maximum amount of Cu substitution by Zn in the development of the energetically stable Zn-CIS nanocrystals in this finding is approximately 32.43%.

Table 6.2 Zeta potential values of different shape Zn-CIS nanocrystals. Particles are the sample obtained under HFMF duration for 30 and 45 seconds which show emission peaks at 590 and 630 nm.

Shape	Particle (30sec)	Particle (45sec)	Cube/Pyramid	Bar
Zeta potential (mV)	7.25	14.3	9.36	9.74

In order to distinguish the difference between magnetically-induced synthesis and the high-temperature organic solvent method (HTOSM), we compared our nanocrystal with the one reported by Nakamura et al. **[75]** The optical properties, including PL and UV-vis characters, are presented in Figure 6.14. There are two emission peaks located at 420 and 560 nm of the HTOSM sample. The 420 nm peak contributed from the ZnS indicates an insufficient energy transition in HTOSM to permit alloying of the Zn atom into the CIS lattice and form a secondary phase, ZnS. This result confirmed our hypothesis of energy transform through magnetic induction. Moreover, the UV-vis absorption spectra of the Zn-CIS nanocrystals prepared with magnetic induction shows a stronger and sharper peak compared to the Zn-CIS nanocrystals prepared through HTOSM. The relatively sharp exciton peak in the absorbance spectra indicates that the Zn-CIS nanocrystals are relatively size- and
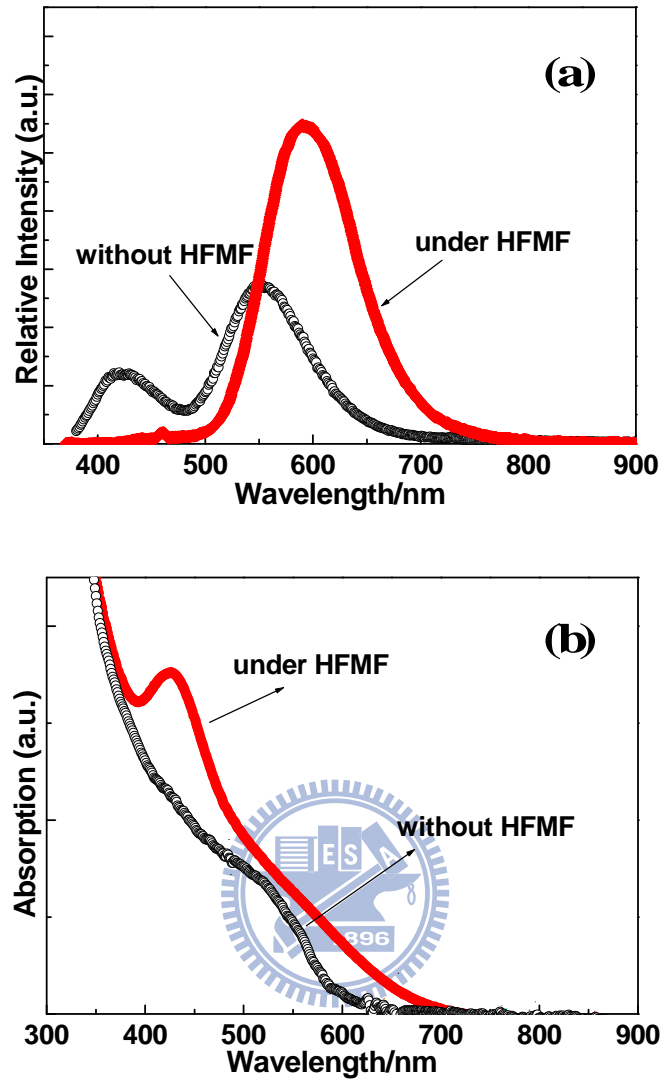
Figure 6.14 Fluorescence (a) and absorption (b) spectra of the Zn-CIS nanocrystals obtained with (red) and without magnetic induction (black). The excitation wavelength for the fluorescence measurements was 366 nm.

shape- monodisperse. Furthermore, the optical properties are much better with band edge PL and narrow peak widths compared with the one prepared from HTOSM. While there are some studies have reported decent results of CIS **[160-164]** and CISe **[164-165]** (CuInSe$_2$) nanocrystals recently, few of them exhibited quantum-confinement behaviors. Nevertheless, all of these reports need rigorous conditions such as high temperature (180~300°C), long crystal-growth duration (1~24 hours), and non-oxygen environment. Compared to those experiment conditions,

magnetically-induced Zn-CIS synthesis is much more easy and fast for such nanocrystals development. This distinct feature further confirms the promising development of magnetically-induced Zn-CIS synthesis over conventional high-temperature pathways.

6.6 Conclusion and implication

A novel method using magnetic doping to form highly-crystalline semiconductor compound in an ambient environment has been explored for the first time. The geometries and lengths of the resulting Zn-doped CIS nanocrystals can be manipulated as a function of the duration in a high-frequency magnetic field. The Zn-CIS nanocrystals exhibited excellent phase pure optical properties and chemically pure crystallinity compared to those prepared via conventional high-temperature methods. The UV-vis absorption spectra of the Zn-CIS colloids has a strong absorption over a relatively wide region from UV to near IR, depending on the dimensional evolution of the Zn-CIS nanocrystals, indicating that the highly-crystalline Zn-CIS colloidal compound prepared in this work can be considered as a potential candidate for solar absorption. Such a magnetically-induced synthesis technology offers great advantages over currently existing methodologies for the growth of these nanocrystals, resulting in better crystalline development and compositional uniformity for such a complex semiconductor compound. Such a novel synthesis method provides a new avenue for the development of ternary chalcopyrite materials via magnetic doping. We also believe that an expansion of such a synthesis technique can be adapted to other important semiconductor compounds, resulting in considerable improvement in purity and optically tunable properties.

Chapter 7

Application of Zn-CuInS2 Nanocrystals Synthesized through Magnetic Field

To employ the Zn doped $CuInS_2$ (Zn-CIS) nanocrystals, as described in chapter 6, for practical application, we prepared a series of Zn-CIS nanocrystal-based solar cell devices using the nanocrystals of various shapes, to measure the solar-cell parameters. The prototype device is schematically represented in Figure 7.1, and Figure 7.2 presents the current-voltage characteristics of the nanocrystal-based devices. The relevant solar-cell parameters for those three samples are given in Table 7.1, which include the current density at short circuit (J_{SC} in mA cm^{-2}), the voltage at open circuit (V_{OC} in V), the fill factor (FF), and the efficiency of power conversion ($\eta = J_{SC} \cdot V_{OC} \cdot FF / P_{in}$ with $P_{in} = 100$ mW cm^{-2}).

Nanocube-based device displayed following characteristics: Jsc = 3.012 mA/cm^2, Voc = 0.61V, FF = 0.38, and an efficiency of 0.70 % in average. The Jsc values increased from 3.012 to 3.317 mA/cm^2 at nanopyramid-based device accompanied with increasing efficiency from 0.7 to 0.80%. The maximum value of Jsc reached 4.21 mA/cm^2 at nanobar-based device with a power conversion efficiency of 1.01% in this study. This result indicated that the ability of light-absorption of Zn-CIS nanocrystal was enhanced once the crystal size was increased. It is obviously suggested that the increasing efficiency of these devices is related to the broadened absorption wavelength of larger Zn-CIS nanocrystals. Referring to previous chapter (see **chapter 6**), the absorption band of Zn-CIS nanocrystals shows a red shift with increasing size, as shown in Figure 7.3. As can be seen in the Table 7.1, compared to other parameters such as Voc and FF, the Jsc is more determinative for this trend, corresponded to the absorbance spectrum.

However, the highest value (4.21 mA/cm^2) of Jsc here is still lower than reported [166] (17 mA cm^{-2}), which might result from thinner absorber layer. Therefore, we deposited the Zn-CIS layers of different thickness for prototype devices, in order to enhance efficiency of the device by increasing Jsc. (The Zn-CIS nanocrystals used here is nanobar-like sample.)
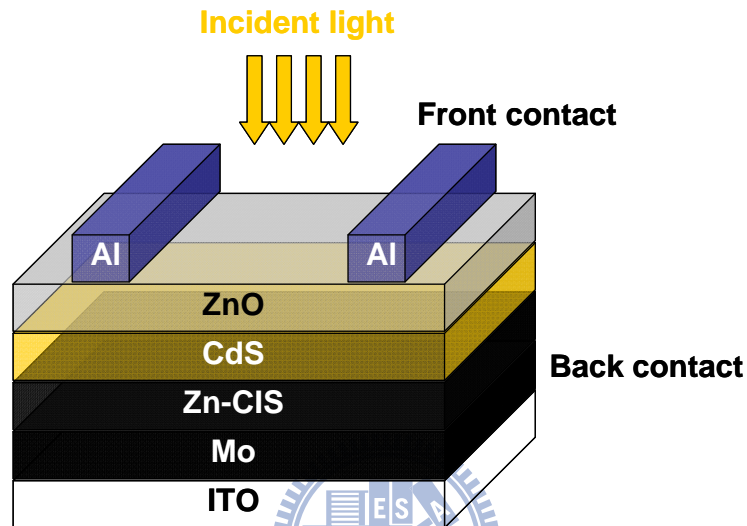
Figure 7.1 Prototype structure of Zn-CIS device.
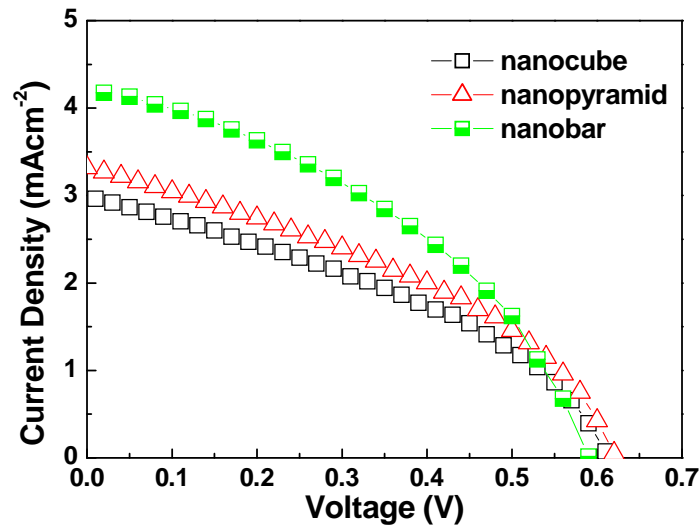
Figure 7.2 Current-voltage characteristics of Zn-CIS devices with different shape nanocrystal under stimulated AM 1.5 solar illumination (100 mW/cm^2) and active area 0.28 cm^2.

The thickness of Zn-CIS layer can be controlled by varying the nanocrystal concentration in the suspensions. Figure 7.4 shows the relationship between absorber layer thickness and the efficiency (the thickness here measured by α-step analysis.). After increasing the thickness of Zn-CIS film, the Voc value shows a slightly increase from 0.59 to 0.62 V which is related to the amount of Zn in the Zn-CIS layer. Based on chapter 6, the incorporation of small amounts of Zn led to an increased Voc [2]. The amount of Zn in the nanobar-like nanocrystal is lightly more than that in other two kinds of nanocrystals, which might provide explanation to the variation of the Voc. The FF value shows a decline from 0.41 to 0.39 at 2.132 μm, indicating the increasing charge recombination with thicker Zn-CIS absorber film. The source of charge recombination might have been a result of film cracking, which became more significant for thicker films than for those two thinner ones. The results display a notably systematic trend for J_{SC}, such that the current density increases significantly from J_{SC} = 4.21 mA/ cm^2 at 1.012 μm to J_{SC} = 5.871 mA/cm^2 at 2.132 μm because thicker absorber offers a promotion of light absorption and photo carrier collection. Because the extent of the increase in J_{SC} was much greater than the extent of the decrease in FF, the overall efficiency of conversion of photons to current exhibits a systematic increase from η = 1.01 % at 1.012 μm to η = 1.44 % at 2.132 μm.

These devices provide a baseline performance and demonstrate as a proof-of-concept that these nanocrystals can be used in PVs. Practical devices, however, require higher efficiencies. There are many ways to try to promote PV efficiency, including using nanocrystals with shorter chain capping ligands, incorporation Ga into the films, and using various chemical or thermal treatment of nanocrystal layers to increase their conductivity. New device architectures that are more favorable to using nanocrystal absorber layers and low-temperature

manufacturing steps may also provide ways to increase device efficiency and eliminate the need for high temperature processing. These are all important topics for further study.

Table 7.1 Photovoltaic performance of the different shape-Zn-CIS nanocrystal-based devices under AM 1.5 solar illumination (100 mW/cm^2) and active area 0.28 cm^2.

	nanocube	nanopyramid	nanobar
J_{sc}/mAcm^{-2}	3.012	3.317	4.21
V_{oc}/V	0.61	0.62	0.59
FF	0.38	0.39	0.41
η (%)	0.7	0.80	1.01
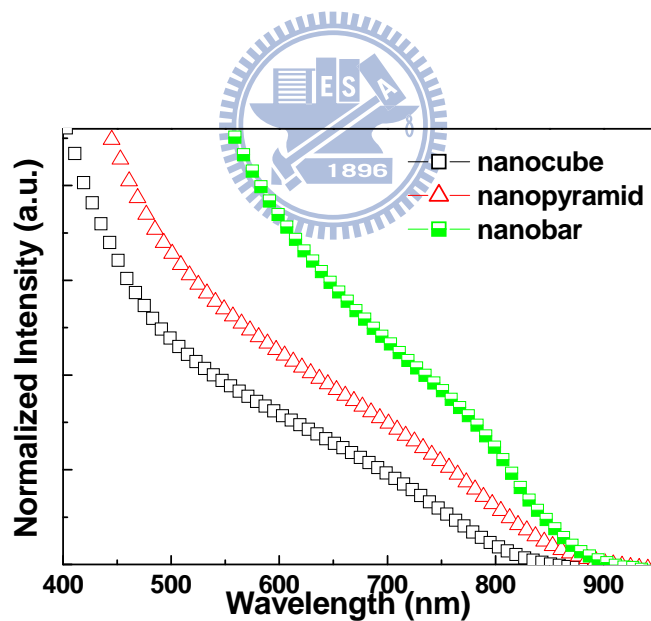
Figure 7.3 UV-vis absorption spectra of different shape Zn-CIS nanocrystals.
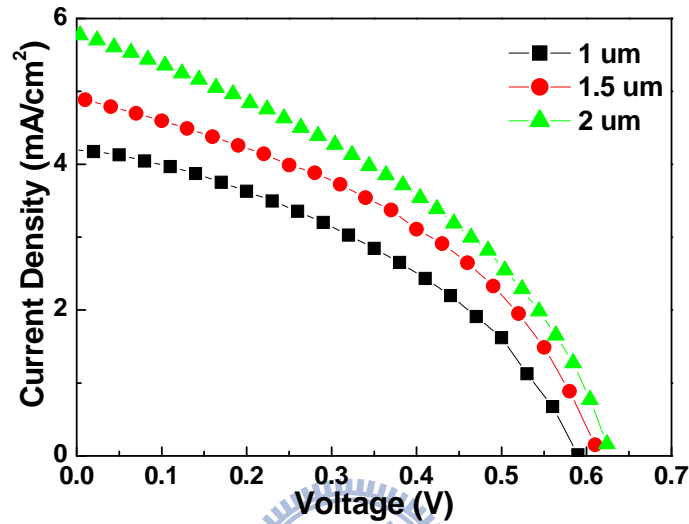
Figure 7.4 Current-voltage characteristics of Zn-CIS devices with different Zn-CIS film thickness under stimulated AM 1.5 solar illumination (100 mW/cm^2) and active area 0.28 cm^2.

Table 7.2 Photovoltaic performance of the different thickness of Zn-CIS nanocrystal film devices under AM 1.5 solar illumination (100 mW/cm^2) and active area 0.28 cm^2.

Thickness (μm)	1.012	1.594	2.132
J_{sc}/mAcm^{-2}	4.21	4.959	5.871
V_{oc}/V	0.59	0.61	0.62
FF	0.41	0.41	0.39
η (%)	1.01	1.25	1.44

Chapter 8

Conclusion

In this thesis, we study the synthesis of nano-scale chalcopyrite $CuInS_2$ (CIS) semiconductors and their application to energy issue. Firstly, we have synthesized CIS nanocrystals smaller than the Wannier-Mott size ($<$ 8.1 nm) through a colloidal solvent process. The nanocrystals produced by this method are 2.4±0.5 nm in size. We have observed the emission peak around 450 nm of these CIS nanoparticles, which is significantly shorter than that of bulk CIS (810 nm) due to quantum confinement effect. After deposition of ZnS layer onto these bare CIS nanocrystals, the photoluminescence intensity was dramatically enhanced by elimination of surface defects. However, new defects were generated with the thickness of ZnS layer over 2 monolayers and resulted in a decreasing PL intensity. (**Chapter 4**)

In order to extend the CIS nanocrystals onto solar energy application, we dope the Zn into CIS nanocrystal to broaden the absorbance spectrum. The average particle sizes of synthesized Zn-CIS nanocrystals with different Cu/Zn ratio (*n*) from 1~3 are 3.5, 4.5, and 4.4 nm respectively. The excitonic transition peaks are shifted to 530, 570, and 660 nm for *n* = 1, 2, and 3, respectively. It is noticeable that the absorption and PL properties of Zn-CIS nanocrystal are dominated by the concentration of Zn doping. The Cu site in the lattice is preferentially substituted by Zn and the substitution is found to be more energetically favorable to prevent anti-site defects, which will affect the absorption spectrum. We have deposited these Zn-CIS nanocrystals onto 5 μm long ZnO nanowires to fabricate the solar device. The best power conversion efficiency of these devices we obtained with different *n* values is 0.28 % at *n* = 2 (*J*sc = 1.71 mA/cm^2, *V*oc = 0.34 V, *FF* = 0.48). The reasons for such low efficiency of this kind of quantum dot-based solar device might

be the QD corrosion from electrolyte and fast recombination. We have demonstrated ZnS deposition as a protecting layer to prevent the corrosion and reduce the recombination by prolonging the exciton lifetime. The efficiency is 0.66 % for the initial ZnS deposition with 0.6 monolayers and promotes to 0.71 % by 1.3 monolayers ZnS deposition due to efficient enhancement of Jsc from 1.71 to 3.21 mA/cm^2. (**Chapter 5**)

Based on Zn-CIS nanocrystals, we continue to investigate the effect of Zn doapant and new synthesis method of this series material. We have synthesized Zn-CIS nanocrystals with different geometries in the presence of high frequency magnetic field (HFMF) at ambient condition. Crystal shape deviates from spherical, cubic, pyramidal, and finally bar with duration time of HFMF. The Zn-CIS nanocrystals obtained within the first 60 seconds exhibited quantum confinement effect, showing emission peaks at 590 (30 sec) ad 630 (45 sec) nm. After longer (120, 300, and 420 seconds, respectively) duration, the UV-vis spectra show the typical absorption curve of a semiconductor material: a band-edge peak was visible at around 710, 780, and 800 nm respectively. All these nanocrystals with variety shapes are monodisperse and highly-crystalline, indicating convenience, rapidity, and novelty of our method. This result demonstrates the fast crystal growth under magnetc-induced heating of such magnetic dopant chalcopyrite semiconductors have potential for optical and energy application. (**Chapter 6**)

For expansion of magnetic-induced synthesized Zn-CIS nanocrystals, we have fabricated a series of solar cell devices using Zn-CIS nanocrystals of various shapes. The best efficiency we obtained is 1.01 % for the nanobar-based device, with Jsc = 4.12 mA/cm^2, Voc = 0.59V, FF = 0.41. The thickness of absorber layer in these devices is around 0.983~1.012 μm. The efficiency of performance is promoted to 1.41 % after deposition of thicker absorber layer (2.132 μm). There are many ways

to try to promote PV efficiency, but our results show the great potential for application in optical and energy device. (**Chapter 7**)
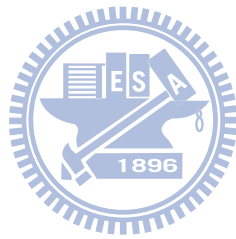
Reference

[1]   M. S. Dresselhaus, I. L. Thomas, Alternative Energy Technologies. *Nature* **2001**, *414*, 332.

[2]   G. W. Crabtree, M. S. Dresselhaus, M. V. Buchanan, The Hydrogen Economy. *Phys. Today* **2004**, *57*, 39.

[3]   K. Jayanthi, S. Chawia, H. Chander, D. Haranath, Structure, Optical and Photoluminescence Properties of ZnS: Cu Nanoparticle Thin Film as a Function of Dopant Concentration and Quantum Confinement Effect. *Cryatal Research and Technology.* **2007**, *42*,976.

[4]   J. Steckel, J. P. Zimmer, S. Coe-Sullivan, N. E. Stott, V. Bulovic, M. G. Bawendi, Color-Saturated Green-Emitting QD-LEDs. *Angew. Chem, Int. Ed.* **2004**, *43*, 2154.

[5]   D. V. Talapin, A. L. Rogach, A. Kornowski, M. Haase, H. Weller, Highly Luminescent Monodisperse CdSe and CdSe/ZnS Nanocrystals Synthesized in a Hexadecylamine−Trioctylphosphine Oxide−Trioctylphospine Mixture. *Nano Lett.* **2001**, *1*, 207.

[6]   A. Eychmu¨ller, Structure and Photophysics of Semiconductor Nanocrystals. *J. Phys. Chem. B* **2000**, *104*, 6514.

[7]   A. Marti, L. Cuadra, A. Luque, Design Constraints of the Quantum-Dot Intermediate Band Solar Cell. *Physica E* **2002**, *14,* 150.

[8]   R. Raffaelle, S. Castro, A. Hepp, S. Bailey, Quantum Dot Solar Cells. *Prog. PhotoVoltaics* **2002**, *10*, 433.

[9]   A. Nozik, Quantum Dot Solar Cells. *Physica E* **2002**, *14*, 115.

[10]   H. Queisser, Photovoltaic Conversion at Reduced Dimensions. *Physica E* **2002**, *14*, 1.

[11]   V. Aroutiounian, S. Petrosyan, A. Khachatryan, Quantum dot solar cells. *J. Appl.*

Phys. **2001**, *89*, 2268.

[12] R. Vogel, P. Hoyer, H. Weller, Quantum-Sized PbS, CdS, Ag$_2$S, Sb$_2$S$_3$, and Bi2S3 Particles as Sensitizers for Various Nanoporous Wide- Bandgap Semiconductors. *J. Phys. Chem.* **1994**, *98*, 3183.

[13] R. Vogel, K. Pohl, H. Weller, Sensitization of Highly Porous, Polycrystalline TiO$_2$ Electrodes by Quantum Sized CdS. *Chem. Phys. Lett.* **1990**, *174*, 241.

[14] D. Liu, P. Kamat, Photoelectrochemical Behavior of Thin CdSe and Coupled TiO2/CdSe Semiconductor Films. *J. Phys. Chem.* **1993**, *97*, 10769.

[15] I. Robel, V. Subramanian, M. Kuno. P. V. Kamat, Quantum Dot Solar Cells. Harvesting Light Energy with CdSe Nanocrystals Molecularly Linked to Mesoscopic TiO2 Films. *J. Am. Chem. Soc.* **2006**, *128*, 2385.

[16] O. Niitsoo, S. K. Sarkar, C. Pejoux, S. Ruhle, D. Cahen, G. Hodes, Chemical Bath Deposited CdS/CdSe-Sensitized Porous TiO2 Solar Cells. *J. Photochem. Photobio. A* **2006**, *181*, 306.

[17] K. S. Leschkies, R. Divakar, J. Basu, E. E. Pommer, J. E. Boercker, C. B. Carter, U. R. Kortshagen, D. J. Norris, E. S. Aydil, Photosensitization of ZnO Nanowires with CdSe Quantum Dots for Photovoltaic Devices. *Nano Lett*. **2007**, *7*, 1793.

[18] J. A. Hollingsworth, K. K. Banger, M. H.-C Jin, J. D. Harris, J. E. Cowen, E. W. Bohannan, J. A. Switzer, W. E. Buhro, and A. F. Hepp, Single Source Precursors for Fabrication of I–III–VI$_2$ Thin-Film Solar Cells via Spray CVD. *Thin Solid Films* **2003**, *431*, 63.

[19] K. K. Banger, J. A. Hollingsworth, J. D. Harris, J. Cowen, W. E. Buhro, and A. F. Hepp, Ternary Single-Source Precursors for Polycrystalline Thin-Film Solar Cells. *Appl. Organomet. Chem*. **2002**, *16*, 617.

[20] K. K. Banger, J. Cowen, A. F. Hepp, Synthesis and Characterization of the First

Liquid Single-Source Precursors for the Deposition of Ternary Chalcopyrite (CuInS$_2$) Thin Film Materials. *Chem. Mater.* **2001**, *13*, 3827.

[21] J. B. Baxter and E. S. Aydil, Structural and Optical Properties of ZnO Nanotower Bundles. *Appl. Phys. Lett.* **2006**, *88*, 123111.

[22] P. Ravirajan, A. M. Peiro, M. K. Nazeeruddin, M. Graetzel, D. D. C. Bradley, J. R. Durrant, J. Nelson, Hybrid Polymer/Zinc Oxide Photovoltaic Devices with Vertically Oriented ZnO Nanorods and an Amphiphilic Molecular Interface Layer. *J. Phys. Chem. B* **2006**, *110*, 7635.

[23] A. N. Shipway, E. Katz, I. Willner, Nanoparticle Arrays on Surfaces for Electronic, Optical, and Sensor Applications. *Chem. Phys. Chem.* **2000**, *1*, 18.

[24] S. Link, M. A. El-Sayed, Optical Properties and Ultrafast Dynamics of Metallic Nanocrystals. *Annu. Rev. Phys. Chem.* **2003**, *54*, 331.

[25] M. Green, Organometallic Based Strategies for Metal Nanocrystal Synthesis. *Chem. Commun.* **2005**, *24*, 3002.

[26] Y. Yin, A. P. Alivisatos, Colloidal Nanocrystal Synthesis and the Organic-Inorganic Interface. *Nature* **2005**, *437*, 664.

[27] L. R. Hirsch, A. M. Gobin, A. R. Lowery, F. Tam, R. A. Drezek, N. J. Halas, J. L. West, Metal Nanoshells. *Ann. Biomed. Eng.* **2006**, *34*, 15.

[28] M.-H. Zhao, Z.-L. Wang, S. X. Mao, Piezoelectric Characterization of Individual Zinc Oxide Nanobelt Probed by Piezoresponse Force Microscope. *Nano Lett.* **2004**, *4*, 587.

[29] R. Narayanan, M. A. El-Sayed, Shape-Dependent Catalytic Activity of Platinum Nanoparticles in Colloidal Solution. *Nano Lett.* **2004**, *4*, 1343.

[30] Thin-film solar cells: an overview, Prince M. 50th Anniversary of Bell Labs solar cell discovery. Proceedings of the 3rd World Conference and Exhibition on Photovoltaic Solar Energy Conversion, **2003**; in press.

[31] D. M. Chapin, C. S. Fuller, G. L. Pearson. A New Silicon *p-n* Junction Photocell for Converting Solar Radiation into Electrical Power. *J. Appl. Phys.* **1954**, *25*, 676.

[32] R. L. Mitchell, C. E. Witt, R. King, D. Ruby, PVMaT Advances in the Photovoltaic Industry and the Focus of Future PV Manufacturing R&D, Proceedings of the 29th IEEE Photovoltaic Specialists Conference, **2002**, 1444.

[33] A. Martin Green, Photovoltaic Principles. *Physica E* **2002**, *14*, 65.

[34] M. A. Contreras, B. Egaas, K. Ramanathan, J. Hiltner, F. Hasoon, R. Noufi, Progress Toward 20% Efficiency in $Cu(In,Ga)$ Se_2 Polycrystalline Thin-Film Solar Cells. *Prog. Photovolt. Res. Appl.* **1999**, *7*, 311.

[35] K. Tennakone, G.R.R. Kumara, I.R.M. Kottegoda, V.S.P. Perera, An Efficient Dye-sensitized Photoelectrochemical Solar Cell Made from Oxide of Tin and Zinc. *Chem. Commun*. **1999**, *1*, 15.

[36] K. Sayama, H. Suguhara, H. Arakawa, Photoelectrochemical Properties of a Porous Nb_2O_5 Electrode Sensitized by a Ruthenium Dye. *Chem. Mater.* **1998**, *10*, 3825.

[37] K. S. Leschkies, R. Divakar, J. Basu, E. Enache-Pommer, J. E. Boercker, C. B. Carter, U. R. Kortshagen, D. J. Norris, E. S. Aydil, Photosensitization of ZnO Nanowires with CdSe Quantum Dots for Photovoltaic Devices. *Nano. Lett.* **2007***, 7,* 1793.

[38] A. Kongkanand, K. Tvrdy, K. Takechi, M. Kuno, P. V. Kamat **,** Quantum Dot Solar Cells. Tuning Photoresponse through Size and Shape Control of $CdSe{-}TiO_2$ Architecture. *J. Am. Chem. Soc.* **2008**, *130*, 4007.

[39] J. L. Shay, J. H. Wernik, Ternary Chalcopyrite Semiconductors: Growth, Electronic Properties and Applications. Oxford: Pergamon Press, **1975**.

[40] Photoluminescence of $CuInS_2$ Nanowires, JCPDS powder diffraction file No.

27-0159.

[41] J. J. M. Binsma, L. J. Giling, J. Bloem, Phase Relations in the System Cu_2S-In_2S_3. *J. Cryst. Growth* **1980**, *50*, 429.

[42] K.-J. Range, G. Engert, A. Weiss, High Pressure Transformations of Ternary Chalcogenides with Chalcopyrite Structure. I. Indium-Containing Compounds. *Solid State Comm.* **1969**, *7*, 1749.

[43] H. W. Spiess, U. Haeberlen, G. Brandt, A. Räuber, J. Scheider, Nuclear Magnetic Resonance in I_B-III-VI_2 Semiconductors. *Phys. Stat. Sol. (b)* **1974**, *62*, 183.

[44] J. E. Jaffe, A. Zunger, Electronic Structure of the Ternary Chalcopyrite Semiconductors $CuAlS_2$, $CuGaS_2$, $CuInS_2$, $CuAlSe_2$, $CuGaSe_2$, and $CuInSe_2$. *Phys. Rev. B* **1983**, *28*, 5822.

[45] S. Kono, M. Okusawa, X-Ray Photoelectron Study of the Valence Bands in I–III–VI_2 Compounds. *J. Phys. Soc. Jpn.* **1974**, *37*, 1301.

[46] W. Braun, A. Goldmann, M. Cardona, Partial Density of Valence States of Amorphous and Crystalline $AgInTe_2$ and $CuInS_2$. *Phys. Rev. B* **1974**, *10*, 5069.

[47] B. Tell, J. L. Shay, H. M. Kasper, Electrical Properties, Optical Properties, and Band Structure of $CuGaS_2$ and $CuInS_2$. *Phys. Rev. B* **1971**, *4*, 2463.

[48] A. N. Tiwari, D. K. Pandya, K. L. Chopra, Electrical and Optical Properties of Single-Phase $CuInS_2$ Films Prepared Using Spray Pyrolysis. *Thin Solid Films* **1985**, *130*, 217.

[49] R. W. Miles, K. T. R. Reddy, I. Forbes, Formation of Polycrystalline Thin Films of $CuInS_2$ by a Two Step Process. *J. Cryst. Growth* **1999**, *198/199*, 316.

[50] Y. Ogawa, S. Uenishi, K. Tohyama, K. Ito, Preparation and Properties of $CuInS_2$ Thin Films, *Solar Energy Mater. Solar Cells* **1994**, *35*, 157.

[51] L. Y. Sun, L. L. Kazmerski, A. H. Clark, P. J. Ireland, D. W. Morton, Absorption

Coefficient Measurements for Vacuum-Deposited Cu-Ternary Thin Films. *J. Vac. Sci.Technol.* **1978**, *15*, 265.

[52] L. L. Kazmerski, C. C. Shieh, Photoconductivity Effects in $CuInS_2$, $CuInSe_2$ and $CuInTe_2$ Thin Tilms. *Thin Solid Films* **1977**, *41*, 35.

[53] D. C. Look, J. C. Manthuruthil, Electron and Hole Conductivity in $CuInS_2$. *J. Phys. Chem. Solids* **1976**, *37*, 173.

[54] B. Tell, J. L. Shay, H. M. Kasper, Room-Temperature Electrical Properties of Ten I-III-VI_2 Semiconductors. *J. Appl. Phys.* **1972**, *43*, 2469.

[55] L. L. Kazmerski, M. S. Ayyagari, G. A. Sanborn, $CuInS_2$ thin films: Preparation and properties. *J. Appl. Phys.* **1975**, *46*, 4865.

[56] S. P. Grindle, C. W. Smith, S. D. Mittleman, Preparation and Properties of $CuInS_2$ Thin Films Produced by Exposing Sputtered Cu-In Films to an H_2S Atmosphere. *Appl. Phys. Lett.* **1979**, *35*, 24.

[57] H. L. Hwang, C. C. Tu, J. S. Maa, C. Y. Sun, On the Preparation of $CuInS_2$ Thin Films by Flash Evaporation. *Solar Energy Mater.* **1980**, *2*, 433.

[58] Y. L. Wu, H. Y. Lin, C. Y. Sun, M. H. Yang, H. L. Hwang, On the Growth of $CuInS_2$ Thin Films by Three-Source Evaporation. *Thin Solid Films* **1989**, *168*, 113.

[59] H. Y. Ueng, H. L. Hwang, The Defect Structure of $CuInS_2$. Part I: Intrinsic Defects. *J. Phys. Chem. Solids* **1989**, *50*, 1297.

[60] A. W. Verheijen, L. J. Giling, J. Bloem, The Region of Existence of $CuInS_2$. *Mater. Res. Bull.* **1979**, *14*, 237

[61] G. Massé, E. Rediai, Radiative Recombination and Shallow Centers in $CuInSe_2$. *J. Appl. Phys.* **1984**, *56*, 1154.

[62] H. Y. Ueng, H. L. Hwang, Defect Identification in Undoped and Phosphorus-Doped $CuInS_2$ Based on Deviations from Ideal Chemical Formula. *J.*

Appl. Phys. **1987**, *62*, 434.

[63] N. Lablou, G. Massé, Donor-Acceptor Pair Transitions in CuInS₂. *J. Appl. Phys.* **1981**, *52*, 978.

[64] F. A. Kroger, *The Chemsitry of Imperfect Crystals, 2nd Ed, Vol. 2*. Amsterdam: North- Holland, **1974**.

[65] H. L. Hwang, L. M. Liu, M. H. Yang, J. S. Chen, J. R. Chen, C. Y. Sun, Composition Determination of CuInS2 by a Chemical Analysis Method. *Solar Energy Mater.* **1982**, *7*, 225.

[66] C. Rincon, S. M. Wasim, In Ternary and Multinary Compounds: Proceedings of the Seventh International Conference, Snowmass, Colorado, September 10-12, 1986, edited by S. K. Deb and A. Zunger (Materials Research Society, Pittsburgh, Pennsylvania, 1987), **1987**, 443.

[67] H. J. Hsu, N. H. Yang, R. S. Tang, T. M. Hsu, H. L. Hwang, A Novel Method to Grow Large CuInS₂ Single Crystals. *J. Cryst. Growth* **1984**, *70*, 427.

[68] Y. Jiang, Y. Wu, X. Mo, W. Yu, Y. Xie, Y. T. Qian, Elemental Solvothermal Reaction to Produce Ternary Semiconductor CuInE (E= S, Se) Nanorods. *Inorg. Chem.* **2000**, *39*, 2964.

[69] J. Xiao, Y. Xie, Y. Xiong, R. Tang, Y. T. Qian, A Mild Solvothermal Route to Chalcopyrite Quaternary Semiconductor CuIn(Se$_x$S$_{1-X}$)₂ Nanocrystallites. *J. Mater. Chem.* **2001**, *11*, 1417.

[70] S. L. Castro, S. G. Bailey, R. P. Raffaelle, K. K. Banger, A. F. Hepp, Nanocrystalline Chalcopyrite Materials (CuInS and CuInSe) via Low-Temperature Pyrolysis of Molecular Single-Source Precursor. *Chem. Mater.* **2003**, *15*, 3142.

[71] A. L. Efros, A. L. Efros, Pioneering Effort I. *Sov. Phys. Semicond*. **1982**, *16*, 772.

[72] J. L. Shay, B. Tell, H. M. Kasper, L. M. Shiavone, *p-d* Hybridization of the

Valence Bands of I-III-VI$_2$ Compounds. *Phys. Rev.* **1972**, *B5*, 5003.

[73] S. L. Castro, S. G. Bailey, R. P. Raffaelle, K. K. Banger, A. F. Hepp, Synthesis and Characterization of Colloidal CuInS Nanoparticles from a Molecular Single-Source Precursor. *J. Phys. Chem. B* **2004**, *108***,** 12429.

[74] J. J. Nairn, P. J. Shapiro, B. Twamley, T. Pounds, R. Wandruszka, T. R. Fletcher, M. Williams, C. Wang, M. G. Norton, Preparation of Ultrafine Chalcopyrite Nanoparticles via the Photochemical Decomposition of Molecular Single-Source Precursors. *Nano. Lett.* **2006**, *6,* 1218.

[75] H. Nakamura, W. Kato, M. Uehara, K. Nose, T. Omata, S. O-Y Matsuo, M. Miyazaki, H. Maeda, Tunable Photoluminescence Wavelenght of Chalcopyrite CuInS-Based Semiconductor Nanocrystals Synthesized in a Colloidal System. *Chem. Mater.* **2006**, *18*, 3330.

[76] T. Yamamoto, I. V. Luck, R. Scheer, H. Katayama-Yoshida, Differences in the Electronic Structure and Compensation Mechanism between N-type Zn- and Cd-Doped CuInS$_2$ Crystals. Physica B **1999**, *273-274*, 927.

[77] D. Pan, L. An, Z. Sun, W. Hou, Y. Yang, Z. Yang, Y. Lu, Synthesis of Cu−In−S Ternary Nanocrystals with Tunable Structure and Composition. *J. Am. Chem. Soc.* **2008**, *130*, 5620.

[78] K. K. Banger, J. A. Hollingsworth, J. D. Harris, J. Cowen, W. E. Buhro, A. F. Hepp,Ternary Single-Source Precursors for Polycrystalline Thin-Film Solar Cells. *Appl. Organomet. Chem.* **2002**, *16*, 617.

[79] K. K. Banger, J. Cowen, and A. F. Hepp, Synthesis and Characterization of the First Liquid Single-Source Precursors for the Deposition of Ternary Chalcopyrite (CuInS$_2$) Thin Film Materials. *Chem. Mater.* **2001**, *13*, 3827.

[80] G. A. Medvedkin, Room Temperature Ferromagnetism in Novel Diluted Magnetic Semiconductor Cd$_{1-x}$Mn$_x$GeP$_2$. *Jpn. J. Appl. Phys.* **2000**, *39*, 949.

[81] Y. J. Zhao, W. T. Geng, A. J. Freeman, T. Oguchi, Electronic and Magnetic

Properties of Ga$_{1-x}$Mn$_x$As: Role of Mn Defect Bands. *Phys. Rev. B* **2001**, *64*, 035207.

[82] Y. J. Zhao, P. Mahadevan, A. Zunger, Comparison of Predicted Ferromagnetic Tendencies of Mn Substituting the Ga Site in III–V's and in I–III–VI$_2$ Chalcopyrite. *Appl. Phys. Lett.* **2004**, *84*, 3753.

[83] C. Erwin, I. Zutic, Tailoring Ferromagnetic Chalcopyrites S. *Nat. Mater.* **2004**, *3*, 410.

[84] C. Czekelius, M. Hilgendorff, L. Spanhel, I. Bedja, M. Lerch, G. Muller, U. Bloeck, D. S. Su, M. Giersig, A Simple Colloidal Route to Nanocrystalline ZnO/CuInS$_2$ Bilayers. *Adv Mater.* **1999**, *11*, 643.

[85] B. O. Dabbousi, J. Rodriguez-Viejo, F. V. Mikulec, J. R. Heine, H. Mattoussi, R. Ober, K. F. Jensen, M. Bawendi, (CdSe)ZnS Core−Shell Quantum Dots: Synthesis and Characterization of a Size Series of Highly Luminescent Nanocrystallites. *J. Phys. Chem. B.* **1997**, *101*, 9463.

[86] M. Kuno, J. K. Lee, B. O. Dabbousi, F. V. Mikulec, M. G. Bawendi, The Band Edge Luminescence of Surface Modified CdSe Nanocrystallites: Probing the Luminescing State. *J. Chem. Phys.* **1997**, *106*, 9869.

[87] X. Peng, M. C. Schlamp, A. Kadavanich, A. P. Alivisatos, Epitaxial Growth of Highly Luminescent CdSe/CdS Core/Shell Nanocrystals with Photostability and Electronic Accessibility. *J. Am. Chem. Soc.* **1997**, *119*, 7019.

[88] M. A. Hines, P. Guyot-Sionnest, Synthesis and Characterization of Strongly Luminescing ZnS-Capped CdSe Nanocrystals. *J. Phys. Chem.* **1996**, *100*, 468.

[89] H. Zajicek, P. Juza, E. Abramof, O. Pankratov, H. Sitter, H. Helm, G. Brunthaler, W. Faschinger, K. Lischka, Photoluminescence from Ultrathin ZnSe/CdSe Quantum Wells. *Appl. Phys. Lett.* **1993**, *62*, 717.

[90] P. Yang, H. Yan, S. Mao, R. Russo, J. Johnson, R. Saykally, N. Morris, J. Pham,

R. He, H.-J. Choi, Controlled Growth of ZnO Nanowires and Their Optical Properties. *Adv. Funct. Mater.* **2002**, *12*, 323.

[91] C. H. Liu, J. A. Zapien, Y. Yao, X. M. Meng, C. S. Lee, S. S. Fan, Y. Lifshitz, S. T. Lee, High-Density, Ordered Ultraviolet Light-Emitting ZnO Nanowire. Arrays *Adv. Mater.* **2003**, *15*, 838.

[92] H. Kind, H. Yan, B. Messer, M. Law, P. Yang, Nanowire Ultraviolet Photodetectors and Optical Switches. *Adv. Mater.* **2002**, *14*, 158

[93] K. Keem, H. Kim, G.-T. Kim, J. S. Lee, B. Min, K. Cho, M.Y. Sung, S. Kim, Photocurrent in ZnO Nanowires Grown from Au Electrodes. *Appl. Phys. Lett.* **2004**, *84*, 4376.

[94] Q. H. Li, T. Gao, Y. G. Wang, T. H. Wang, Adsorption and Desorption of Oxygen Probed from ZnO Nanowire Films by Photocurrent Measurements. *Appl. Phys. Lett.* **2005**, *86*, 123117.

[95] O. Harnack, C. Pacholski, H. Weller, A. Yasuda, J. M. Wessels, Rectifying Behavior of Electrically Aligned ZnO Nanorods. *Nano Lett.* **2003**, *3*, 1097.

[96] P. Ravirajan, A. M. Peiro, M. K. Nazeeruddin, M. Graetzel, D. D. C. Bradley, J. R. Durrant, and J. Nelson, Hybrid Polymer/Zinc Oxide Photovoltaic Devices with Vertically Oriented ZnO Nanorods and an Amphiphilic Molecular Interface Layer. *J. Phys. Chem. B* **2006**, *110*, 7635.

[97] J. B. Baxter and E. S. Aydil, Structural and Optical Properties of ZnO Nanotower Bundles. *Appl. Phys. Lett.* **2006**, *88*, 123111.

[98] M. Law, L. E. Greene, J. C. Johnson, R. Saykally, P. Yang, Nanowire Dye-Sensitized Solar Cells. *Nat. Mater.* 2005, *4*, 455.

[99] J. B. Baxter, E. S. Aydil, Nanowire-Based Dye-Sensitized Solar Cells. *Appl. Phys. Lett.* **2005**, *86*, 053114.

[100] R. D. Schaller, V. I. Klimov, High Efficiency Carrier Multiplication in PbSe

Nanocrystals: Implications for Solar Energy Conversion. *Phys. Rev. Lett.* **2004**, *92*, 186601.

[101] R. J. Ellingson, M. C. Beard, J. C. Johnson, P. R. Yu, O. I. Micic, A. J. Nozik, Shabaev, A. L. Efros, Highly Efficient Multiple Exciton Generation in Colloidal PbSe and PbS Quantum Dots. *Nano Lett.* **2005**, *5*, 865.

[102] R. D. Schaller, M. A. Petruska, V. I. Klimov, Effect of Electronic Structure on Carrier Multiplication Efficiency: Comparative Study of PbSe and CdSe Nanocrystals. *Appl. Phys. Lett.* **2005**, *87*, 253102.

[103] J. E. Murphy, M. C. Beard, A. G. Norman, S. P. Ahrenkiel, J. C. Johnson, P. R. Yu, O. I. Micic, R. J. Ellingson, A. J. Nozik, PbTe Colloidal Nanocrystals: Synthesis, Characterization, and Multiple Exciton Generation. *J. Am. Chem. Soc.* **2006**, *128*, 3241.

[104] R. Vogel, P. Hoyer, H. Weller, Quantum-Sized PbS, CdS, Ag$_2$S, Sb$_2$S$_3$, and Bi$_2$S$_3$ Particles as Sensitizers for Various Nanoporous Wide-Bandgap Semiconductors. *J. Phys. Chem.* **1994**, *98*, 3183.

[105] R. Vogel, K. Pohl, H. Weller, Sensitization of Highly Porous, Polycrystalline TiO$_2$ Electrodes by Quantum Sized CdS. *Chem. Phys. Lett.* **1990**, *174*, 241.

[106] D. Liu, P. Kamat, Photoelectrochemical Behavior of Thin Cadium Selenide and Coupled Titania/Cadium Selenide Semiconductor Films. *J. Phys. Chem.* 1993, *97*, 10769.

[107] I. Robel, V. Subramanian, M. Kuno, P. V. Kamat, Quantum Dot Solar Cells. Harvesting Light Energy with CdSe Nanocrystals Molecularly Linked to Mesoscopic TiO$_2$ Films. *J. Am. Chem. Soc.* **2006**, *128*, 2385.

[108] O. Niitsoo, S. K. Sarkar, C. Pejoux, S. Ruhle, D. Cahen, G. Hodes, Chemical Bath Deposited CdS/CdSe-Sensitized Porous TiO$_2$ Solar Cells. *J. Photochem. Photobiol. A* **2006**, *181*, 306.

[109] K. S. Leschkies, R. Divakar, J. Basu, E. E. Pommer, J. E. Boercker, C. B. Carter, U. R. Kortshagen, D. J. Norris, E. S. Aydil, Photosensitization of ZnO Nanowires with CdSe Quantum Dots for Photovoltaic Devices. *Nano Lett.* **2007**, *7*, 1793.

[110] B. O'Regan, D. T. Schwartz, Large Enhancement in Photocurrent Efficiency Caused by UV Illumination of the Dye-Sensitized Heterojunction TiO_2/RuLL'NCS/CuSCN:　Initiation and Potential Mechanisms. *Chem. Mater*. **1998**, *10*, 1501.

[111] G. R. A. Kumara, S. Keneko, M. Okuya, K. Tennakone, Fabrication of Dye-Sensitized Solar Cells Using Triethylamine Hydrothiocyanate as a CuI Crystal Growth Inhibitor. *Lanrmuir* **2002**, *18*, 10493.

[112] F. Cao, G. Oskam, P. C. Searson, A Solid-State Dye-Sensitized Photoelectrochemical Cell. *J. Phys. Chem*. **1995**, *99*, 17071.

[113] K. Tennakone, G. K. R. Senadeera, V. P. S. Perera, I. R. M. Kottegoda, L. A. A De Silva, Dye-Sensitized Photoelectrochemical Cells Based on Porous SnO_2/ZnO Composite and TiO_2 Films with a Polymer Electrolyte. *Chem. Mater*. **1999**, *11*, 2474.

[114] E. Stathatos, P. Lianos, C. Krontiras, Dye-Sensitized Photoelectrochemical Cell Using a Nanocomposite SiO_2/Poly(Ethylene Glycol) Thin Film as Electrolyte Support. Characterization by Time-Resolved Luminescence and Conductivity Measurements. *J. Phys. Chem. B* **2001**, *105*, 3486.

[115] T. Stergiopoulos, I. M. Arabatzis, G. Katsaros, P. Falaras, Binary Polyethylene Oxide/Titania Solid-State Redox Electrolyte for Highly Efficient Nanocrystalline TiO_2 Photoelectrochemical Cells. *Nano Lett.* **2002**, *2*, 1259.

[116] A. F. Nogueira, J. R. Durrant, M. –A. De Paoli, Dye-Sensitized Nanocrystalline Solar Cells Employing a Polymer Electrolyte. *Adv. Mater*.

2001, *13*, 826.

[117] E. Stathatos, P. Lianos, U. Lavrencic-Stangar, B. Orel, A High-Performance Solid-State Dye-Sensitized Photoelectrochemical Cell Employing a Nanocomposite Gel Electrolyte Made by the Sol-Gel Route. *Adv. Mater*. **2002**, *14*,354.

[118] B. Asenjoa, A. M. Chaparroa, M. T. Gutie'rreza, J. Herreroa, J. Klaer, Study of CuInS2/ZnS/ZnO solar cells, with Chemically Deposited ZS Buffer Layers from Acidic Solutions. *Sol. Energ. Mat. Sol. C.* **2008**, *92*, 302.

[119] S. F. Wuister, I. Swart, F. Driel, S. G. Hickey, C. M. Donega, Highly Luminescent Water-Soluble CdTe Quantum Dots. *Nano Lett*. **2003**, *3*, 503.

[120] D. Braunger, Th. Dürr, D. Hariskos, Ch. Köble, Th. Walter, N. Wieser, and H. W. Schock, in: Proceedings of the 24th IEEE Photovoltaic Specialists Conference, New York, **1998**.

[121] K. S. Kim, Y.S. Kang, J. H. Lee, Y. J. Shin, N. G. Park, K. S. Ryu, S. H. Chang, Photovoltaic Properties of Nano-particulate and Nanorod Array ZnO Electrodes for Dye-Sensitized Solar Cell. *Bull. Korean Chem. Soc.* **2006**, *27*, 295.

[122] N. M. Dimitrijevic, Electron-Transfer Reactions on CdSe Colloids as Studied by Pulse Radiolysis. *J. Chem. Soc., Faraday Trans. 1* **1987**, *83*, 1193.

[123] N. M. Dimitrijevic, P. V. Kamat, Transient Photobleaching of Small Cadmium Selenide Colloids in Acetonitrile Anodic Decomposition. *J. Phys. Chem.* **1987**, *91*, 2096.

[124] Y. Matsumoto, R. Kanemoto,T. Itoh, S. Nakanishi, M. Ishikawa, V. Biju, Photoluminescence Quenching and Intensity Fluctuations of CdSe-ZnS Quantum Dots on an Ag Nanoparticle Film. *J. Phys. Chem. C* **2008,** *112,* 1345.

[125] S. M. Yang, C. H. Huang, J. Zhai, Z. S. Wang, L. Jiang, High Photostability and Quantum Yield of Nanoporous TiO2 Thin Film Electrodes Co-Sensitized with Capped Sulfides. *J. Mater. Chem.* **2002**, *12*, 1459.

[126] C. C. Lin, C. S. Hsiao, S. Y. Chen, S. Y. Cheng, Ultraviolet Emission in ZnO Films Controlled by Point Defects. *J. Electrochem. Soc.* **2002**, 151, G285-G288.

[127] S. Sun, C.B. Murray, D. Weller, L. Folks, A. Moser, Monodisperse FePt Nanoparticles and Ferromagnetic FePt Nanocrystal Superlattices. *Science* **2000**, *287*, 1989.

[128] S. Chen, Z. L. Wang, J. Ballato, S. H. Foulger, D. L. Carroll. Monopod, Bipod, Tripod, and Tetrapod Gold Nanocrystals. *J. Am. Chem. Soc*. **2003**, *125*, 16186.

[129] X. Peng, U. Manna, W. Yang, J. Wickham, E. Scher, A. Kadavanich, A. P. Allvisatos, Shape Control of CdSe Nanocrystals. *Nature* **2000**, *404*, 59.

[130] V. F. Puntes, D. Zanchet, C. K. Erdonmez, A. P. Alivisatos, . Synthesis of Hcp-Co Nanodisks. *J. Am. Chem. Soc*. **2002**, *124*, 12874

[131] N. Cordente, C. Amiens, B. Chaudret, M. Respaud, F. Senocq, M. J. Casanove, Chemisorption on Nickel Nanoparticles of Various Shapes: Influence on Magnetism. *J. Appl. Phys.* **2003**, *94*, 6358.

[132] C. Qian, F. Kim, L. Ma, F. Tsui, P. Yang, J. Liu, Solution-Phase Synthesis of Single-Crystalline Iron Phosphide Nanorods/Nanowires. *J. Am. Chem. Soc.* **2004**, *126*, 1195.

[133] D. V. Talapin, R. Koeppe, S. Goetzinger, A. Kornowski, J. M. Lupton, A. L. Rogach, O. Benson, J. Feldmann, H. Weller, Highly Emissive Colloidal CdSe/CdS Heterostructures of Mixed Dimensionality. *Nano Lett.* **2003**, *3*, 1677.

[134] M. Yin, Y. Gu, I. L. Kuskovsky, T. Andelman, Y. Zhu, G. F. Neumark, S.

O'Brien, Zinc Oxide Quantum Rods. *J. Am. Chem. Soc.* **2004**, *126*, 6206.

[135]   D. J. Milliron, S. M. Hughes, Y. Cui, L. Manna, J. Li, L. −W. Wang, A. P. Alivisatos, Colloidal Nanocrystal Heterostructures with Linear and Branched Topology. *Nature* **2004**, *430*, 190.

[136]   B. Li, Y. Xie, J. Huang, Y. T. Qian, Synthesis by a Solvothermal Route and Characterization of CuInSe$_2$ Nanowhiskers and Nanoparticles. *Adv. Mater.* **1999**, *11*, 1456.

[137]   M. A. Malik, P. O'Brien, N. Revaprasadu, A Novel Route for the Preparation of CuSe and CuInSe$_2$ Nanoparticles. *Adv. Mater.* **1999**, *11*, 1441.

[138]   H. Z Zhong, Y. C. Li, M. F. Ye, Z. Z. Zhu, Y. Zhou, C. H. Yang, Y. F. Li, A Facile Route to Synthesize Chalcopyrite CuInSe$_2$ Nanocrystals in Non-Coordinating Solvent. *Nanotechnology* **2007**, *18*, 025602.

[139]   L. Tian, H. I. Elim, W. Ji, J. J. Vittal, One-Pot Synthesis and Third-Order Nonlinear Optical Properties of AgInS$_2$ Nanocrystals. *Chem. Commun.* **2006**, *41*, 4276

[140]   K. K. Banger, M. H. C. Jin, J. D. Harris, P. E. Fanwick, A. F. Hepp, A New Facile Route for the Preparation of Single-Source Precursors for Bulk, Thin-Film, and Nanocrystallite I-III-VI Semiconductors. *Inorg Chem.* **2003**, *42*, 7713.

[141]   T. Kamatani, H. Akai, The Magnetic Properties in Transition Metal-Doped Chalcopyrite Semiconductors. *Mat. Sci. Semicon. Proc.* **2003,** *6,* 389.

[142]   L.-H. Ye, A. J. Freeman, B. Delley, Half-Metallic Ferromagnetism in Cu-Doped ZnO: Density Functional Calculations. *Phys. Rev. B* **2006**, *73*, 033203.

[143]   K. R. Kittilstved, D. R. Gamelin, Activation of High-T_c Ferromagnetism in Mn^{2+}-Doped ZnO using Amines. *J. Am. Chem. Soc.* **2005**, *127*, 5292.

[144] G. Z. Xing, J. B. Yi, J. G. Tao, T. Liu, L. M. Wong, Z. Zhang, G. P. Li, S. J. Wang, J. Ding, T. C. Sum, C. H. A. Huan, T. Wu, Comparative Study of Room-Temperature Ferromagnetism in Cu-Doped ZnO Nanowires Enhanced by Structural Inhomogeneity. *Adv. Mater.* **2008**, *9999*, 1.

[145] T. Shinohara, T. Sato, T. Taniyama, Surface Ferromagnetism of Pd Fine Particles. *Phys. Rev. Lett.* **2003**, *91*, 197201.

[146] B. Sampedro, P. Crespo, A. Hernando, R. Litran, J. C. Sanchez Lopez, C. Lopez Cartes, A. Fernandez, J. Ramirez, J. Gonzalez Calbet, M. Vallet, Ferromagnetism in fcc Twinned 2.4 nm Size Pd Nanoparticles. *Phys. Rev. Lett.* **2003**, *91*, 237203.

[147] P. Crespo, R. Litran, T. C. Rojas, M. Multigner, J. M. de la Fuente, J. C. Sanchez Lopez, M. A. Garcia, A. Hernando, S. Penades, A. Fernandez, A. Permanent Magnetism, Magnetic Anisotropy, and Hysteresis of Thiol-Capped Gold Nanoparticles. *Phys. Rev. Lett.* **2004**, *93*, 087204.

[148] Y. Yamamoto, T. Miura, M. Suzuki, N. Kawamura, H. Miyagawa, T. Nakamura, K. Kobayashi, T. Teranishi, H. Hori, Direct Observation of Ferromagnetic Spin Polarization in Gold Nanoparticles. *Phys. Rev. Lett.* **2004**, *93*, 116801.

[149] T. L. Makarova, B. Sundqvist, R. Hohne, P. Esquinazi, Y. Kopelevich, P. Scharff, V. A. Davydov, L. S. Kashevarova, A. V. Rakhmanina, Magnetic Carbon. *Nature* **2001**, *413*, 716.

[150] N. Tsujii, H. Kitazawa, G. Kido, Electric and Magnetic Properties of Mn- and Fe-Doped $CuInS_2$ Compounds. *Phys. Stat. sol. (a)* **2002**, *189*, 951.

[151] A. Pietnoczka, R. Bacewicz, S. Schorr, Local Structure in $(MnS)_{2x}(CuInS_2)_{1-x}$ Alloys. *Phys. Stat. sol. (a)* **2006**, *203*, 2746.

[152] B. Koo, R. N. Patel, B. A. Korgel, Synthesis of CuInSe Nanocrystals with

Trigonal Pyramidal Shape. *J. Am. Chem. Soc.* **2009**, **DOI:** 10.1021/ja8080605.

[153] N. Pinna, K. Weiss, J. Urban, M. P. Pileni, Triangular CdS Nanocrystals: Structural and Optical Studies. *Adv. Mater.* **2001**, *13*, 261.

[154] Y. Cui, J. Ren, G. Chen, Y. Qian, Y. Xie, A Simple Route to Synthesize MInS$_2$ (M=Cu, Ag) Nanorods from Single-molecular Precursors. *Chem. Lett.* **2001**, *30,* 236.

[155] W. Han, L. Yi, N. Zhao, A. Tang, M. Gao, Z. Tang, Synthesis and Shape-Tailoring of Copper Sulfide/Indium Sulfide-Based Nanocrystals. *J. Am. Chem. Soc.* **2008,** *130***,** 13152.

[156] S. -H. Choi, E. -G. Kim, T. Hyeon, One-Pot Synthesis of Copper-Indium Sulfide Nanocrystal Herterostructures with Acorn, Bottle, and Larva Shapes. *J. Am. Chem. Soc.* **2006**, *128,* 2520.

[157] S. M. Lee, S. N. Cho, J. W. Cheon, Anisotropic Shape Control of Colloidal Inorganic Nanocrystals. *Adv. Mater.* **2003**, *15,* 441.

[158] R. E. Rosensweig, Heating Magnetic Fluid with Alternating Magnetic Field. *J. Magn. Magn. Mater.* **2002,** *252*, 370.

[159] C. Corrado, Y. Jiang, F. Oba, M. Kozina, F. Bridges, J. Z. Zhang, Sythesis, Structural, and Optical Properties of Stable ZnS:Cu,Cl Nanocrystals. *J. Phys. Chem. C* **2009**, *113*, 3830.

[160] S. T. Connor, C. –M. Hsu, B. D. Weil, S. Aloni, Y. Cui, Phase Transformation of Biphasic Cu$_2$S-CuInS$_2$ to Monophasic CuInS$_2$ Nanorods. *J. Am. Chem. Soc.* **2009**, *131*, 4962.

[161] R. Xie, M. Rutherford, X. Peng, Formation of High-Quality I-III-VI Semiconductor Nanocrystals by Tuning Relative Reactivity of Cationic Precursors. *J. Am. Chem. Soc.* **2009**, *131*, 5691.

[162] Y. Qi, Q. Liu, K. Tang, Z. Liang, Z. Ren, X. Liu, Synthesis and

Characterization of Nanostructured Wurtzite $CuInS_2$: A New Cation Disordered Polymorph of CuInS2. *J. Phys. Chem. C* **2009**, *113*, 3939.

[163] H. Zhong, Y. Zhou, M. Ye, Y. He, J. Ye, C. He, C. Yang, Y. Li, Controlled Synthesis and Optical Properties of Colloidal Ternary Chalcogenide $CuInS_2$ Nanocrystals. *Chem. Mater.* **2008**, *20*, 6434.

[164] M. G. Panthani, V. Akhavan, B. Goodfellow, J. P. Schmidtke, L. Dunn, A. Dodabalapur, P. F. Barbara, B. A. Korgel, Synthesis of $CuInS_2$, $Cu(In_xGa_{1-x})Se_2$ (CIGS) nanocrystal "Inks" for Printable Photovoltaic. *J. Am. Chem. Soc.* **2008**, *130*, 16770.

[165] P. M. Allen, M. G. Bawendi, Ternary I-III-VI Quantum Dots Luminescent in Red to Near-Infrared. *J. Am. Chem. Soc.* **2008**, *130*, 9240.

[166] M. Nanu, J. Schoonman, A. Goossens, Nanocomposite Three-Dimensional Solar Cells Obtained by Chemical Spray Deposition. *Nano Lett*. **2005**, 5, 1716.

Curriculum Vitae

Name: Kuan-Ting Kuo

14.08.1979   Born in Kaohsiung (Taiwan)

1997-2001   Undergraduate study in the department of chemistry at Tung Hai
   Universirty

2001-2003   Graduate study in the institute of chemistry at National Kaohsiung
                Normal University

                Master Thesis: Synthesis of 2-(S)-benzyloxylpropanol and liquid
                crystals content it

2003-2004   Intern teacher of chemistry at National Feng Shan Senior High
                School (Kaohsiung, Taiwan)

2004-2009   PhD study in the department of materials science and engineering at
                Chiao Tung University (Taiwan)

                PhD Thesis: Study on synthesis and optical characterics of
                chalcopyrite nanocrystals
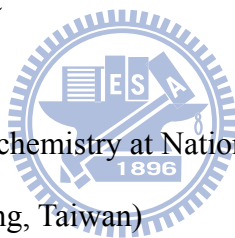
Publication list

Journal

[1] **K. T. Kuo**, S. P. Lee, S. Y. Chen, B. M. Cheng, H. C. Lu, and C. C. Ting, "Effect of microwave irradiation on surface characteristics and luminescent properties of $BaMgAl_{10}O_{17}$:Eu blue phosphor", *J. Phys. Chem. Solids* **2008**, 69, 362-365. (*Impact Factor*: 1.103)

[2] **K. T. Kuo,** S. P. Lee, S. Y. Chen, B. M. Cheng, H. C. Lu, D. M. Liu, and C. C. Ting, "$BaMgAl_{10}O_{17}$:Eu blue phosphor with MgO coating and microwave irradiation", *J. Phys. Chem. Solids* **2008**, 69, 446-450. (*Impact Factor*: 1.103)

[3] **K. T. Kuo,** S. Y. Chen, B. M. Cheng and C. C. Lin, "Synthesis and characterization of highly luminescent $CuInS_2$ and $CuInS_2$/ZnS (core/shell) nanocrystals", *Thin Solid Film,* **2008***,* 517, 1257-1261. (*Impact Factor*: 1.884)

[4] **K. T. Kuo,** D. M. Liu, S. Y. Chen, and C. C. Lin, "Core-shell CuInS2/ZnS quantum dots assembled on short ZnO nanowires with enhanced photo-conversion efficiency", *J. Mater. Chem.* **2009**, DOI: 10.1039/b907765k. (*Impact Factor*: 4.646)

[5] S. H. Hu**, K. T. Kuo**, W. L. Tung, D. M. Liu, and S. Y. Chen, "A multifunctional nanodevice capable of imaging, magnetically controlling, and in-situ monitoring drug release", *Adv. Func. Mater.* **2009**, DOI: 10.1002/adfm.200900465. (*Impact Factor*: 6.808)

[6] **K. T. Kuo,** S. H. Hu, D. M. Liu, and S. Y. Chen, "Magnetically-induced synthesis of highly-crystalline ternary semiconductor chalcopyrite nanocrystals at ambient conditions", *J. Mater. Chem*. **2009,** submitted.

Conference Papers

[1] C. C. Lin, S. P. Lee, **K. T. Kuo**, and S. Y. Chen, "Engineered Surface with Improved Luminous Efficiency of Phosphor Powder for Plasma Planar Back Light", Society for Information Display 2005 (SID 2005), Hynes Convention Center, Boston, Massachusetts, U.S.A, May 22nd - 27th, 2005.

[2] C. C. Lin, S. P. Lee, **K. T. Kuo**, and S. Y. Chen, "Improved luminescent efficiency of PDP blue phosphor by microwave irradiation", 2005, MRS Spring Meeting, San Francisco, California, U.S.A, March 28th - April 1st, 2005.

[3] C. C. Lin, S. P. Lee, **K. T. Kuo**, and S. Y. Chen, "Study on luminous phosphor with improved efficiency for plasma planar back light", International Display Manufacturing Conference (IDMC) 2005, Taipei, Taiwan, Feb. 21st – 24th, 2005.

[4] **K. T. Kuo**, S. P. Lee, S. Y. Chena, B. M. Cheng, H. C. Lu and C. C. Ting, "Effect of microwave irradiation on surface characteristics and luminescent properties of $BaMgAl_{10}O_{17}$:Eu blue phosphor", Proceedings of the 2nd International Symposium on Point Defect and Non-Stoichiometry (ISPN-2), Kaohsiung, Taiwan, Oct 4th – 6th, 2005.

[5] **K. T. Kuo**, S. P. Lee, S. Y. Chena, B. M. Cheng, H. C. Lu, and D. M. Liu, "$BaMgAl_{10}O_{17}$:Eu Blue Phosphors with MgO Coating and Microwave Irradiation", Proceedings of the 2nd International Symposium on Point Defect and Non-Stoichiometry (ISPN-2), Kaohsiung, Taiwan, Oct 4th - 6th, 2005.

[6] **K. T. Kuo**, S. P. Lee, S. Y. Chena, B. M. Cheng, H. C. Lu, and D. M. Liu, "Improvement of luminance and deterioration resistance of BAM

phosphor in PDP application", the 5th International Conference on Synchrotron Radiation in Materials Science (SRMS-5), Chicago, Illinois, U.S.A., Jul. 30th - Aug. 2nd, 2006.

[7] **K. T. Kuo**, S. Y. Chena, B. M. Cheng, and C. C. Lin, "Synthesis and characterization of highly luminescent $CuInS_2$ and $CuInS_2/ZnS$ (core/shell) nanocrystals", 35th International Conference on Metallurgical Coatings and Thin Films (ICMCTF) 2008, San Diego, California, U.S.A., April 28th – May 2nd, 2008.

Domestic Journal

陳三元，郭冠廷，『螢光粉在液晶顯示器背光模組之電漿式平面光源的應用及探討』，電子月刊，**2007**，141(4)，114-124

Award

胡尚秀，董維琳，郭冠廷，『設計與製備具顯影、標靶與即時監測藥物釋放之多功能型奈米藥物輸送載體元件』，2008 第六屆國家新創獎學生組第二名